Microscopic flows of aqueous polyacrylamide solutions: a quantitative study

A thesis
submitted to The University of Manchester
for the degree of doctor of philosophy (PhD)
in the faculty of Engineering and Physical Sciences

Alfredo Lanzaro

School of Chemical Engineering and Analytical Science
2011

Contents

Final word count: 18109

List of Figures

List of Tables

Abstract

Microfluidic technology makes it possible to study highly nonlinear polymer dynamics in large Weissenberg number, moderate Reynolds number flow regimes, even for dilute polymer solutions having low viscosities and very short relaxation times. The strongly non-linear effects observable in microfluidic flow are of crucial importance for optimizing the design of inkjet printers, enhanced oil recovery, "lab-on-a-chip" essays and "micro-rheometers" operating at high deformation rates with minimal inertial effects.

This thesis presents quantitative results on the nonlinear flows of molecularly and rheometrically well-characterized aqueous solutions of a large molecular weight, highly polydisperse polyacrylamide (PAAm) sample through several benchmark flow geometries. A complete set of molecular and rheometric data for PAAm solutions has been obtained, including: gel-permeation chromatography (GPC) molecular characterisation; the steady shear viscosities, as measured by means of a commercial ARES device and of a novel microfluidic rheometer, over a large range of shear rates ($0.1 \leq \dot{\gamma} \leq 4 * 10^4\,\mathrm{s}^{-1}$); linear viscoelasticity data obtained by means of both a Vilastic-3 Analyzer and of a piezolelastic axial vibrator (PAV), over a broad range of frequencies ($10^{-2} \leq \omega \leq 10^4\,\mathrm{Hz}$); the data from capillary-driven elongational flow measurements using a CaBER rheometer.

Using three flow geometries, nonlinear flows of PAAm solutions in different concentrations over a wide range of Elasticity number ($13.3 \leq El \leq 476.8$) and Weissenberg number ($1.4 \leq Wi \leq 131.7$) flow regimes are studied by means of micro-particle image velocimetry ($\mu - PIV$) and pressure drop measurements. Some intriguing viscoelastic flow phenomena were observed for the first time, to our best knowledge. It was established that changing the contraction ratio leads to significant changes in the observed flow patterns even for close values of the Elasticity number. Moreover, tuning El under a given flow geometry can either increase or decrease the stability of the nonlinear flow structures. It was also found that, in addition to Wi and El, the viscoelastic flow phenomena are very sensitive to the molecular properties of polymer. The excess pressure drops across the contraction-expansion geometry were correlated closely with the vortex growth mechanism.

A numerical algorithm has been developed to compute local extensional rates along the streamlines. It can map out the spatial distribution of the local stretch experienced by polymer chains across complex flow domain at any instant. The method led to a definition of "local Deborah number" field, which describes viscoelastic flows in complex geometries in a more accurate way than the nominal, arbitrarily defined Weissenberg number. Hence, the spatial distribution of polymer conformation being stretched from the equilibrium under flow condition can be visualized across flow domain through an image of the local De field. The time evolution of these images will provide physical insight to nonlinear polymer dynamics in complex flow as well as to develop a better constitutive model for semi-dilute polymer solutions.

Declaration

I declare that no portion of this work referred to in this thesis has been submitted in support of an application for another degree or qualification of this or any other university or other institute of learning.

Signed: Date: August 29, 2011

Copyright

I. The author of this thesis (including any appendices and/or schedules to this thesis) owns any copyright in it (the "Copyright") and he has given The University of Manchester the right to use such Copyright for any administrative, promotional, educational and/or teaching purposes.

II. Copies of this thesis, either in full or in extracts and whether in hard or electronic copy, may be made **only** in accordance with the Copyright, Designs and Patents Act 1988 (as amended) and regulations issued under it or, where appropriate, in accordance with licensing agreements which the University has from time to time. This page must form part of any such copies made.

III. The ownership of certain Copyright, patents, designs, trade marks and other intellectual property (the Intellectual Property) and any reproductions of copyright works in the thesis, for example graphs and tables (Reproductions), which may be described in this thesis, may not be owned by the author and may be owned by third parties. Such Intellectual Property and Reproductions cannot and must not be made available for use without the prior written permission of the owner(s) of the relevant Intellectual Property and/or Reproductions.

IV. Further information on the conditions under which disclosure, publication and commercialisation of this thesis, the Copyright and any Intellectual Property and/or Reproductions described in it may take place is available in the University IP Policy (see `http://documents.manchester.ac.uk/DocuInfo.aspx?DocID=487`), in any relevant Thesis restriction declarations deposited in the University Library, The University Library's regulations (see `http://www.manchester.ac.uk/library/aboutus/regulations`) and in The University's policy on Presentation of Theses.

Acknowledgements

There is a number of people that I would like to thank for helping me during this research. They are, in a rigorously *non* alphabetical order:

- My supervisor, Dr. Xue-Feng Yuan, for giving me the opportunity of studying for my PhD in the School where the Chemical Engineering was invented nearly 150 years ago (which is matter of great pride for a chemical engineer like me), and for his energetic and tireless support throughout all my studies. I don't think that this work would have been possible without his help.

- I also would like to acknowledge Keith Nixon and Colin Booth from the School of Chemistry, University of Manchester, and Damien Vadillo and Malcolm Mackley from the University of Cambridge, UK, for their help on GPC and PAV measurements respectively.

- All the people I have been working with during my research period (Joseph Dawes, Dr. Sunday Omowunmi, Dr. Zhuo Li, Dr. Gabriel Aloku, Dr. Simon Haward, Dr. Jeff Odell and many others), for many interesting discussions and for creating a truly enjoyable work environment

- All the members of my family, for their invaluable support (either here or from Italy)

- My girlfriend, for an approximately infinite patience

Chapter 1

Introduction

Microfluidics is commonly known as a technology capable of controlling and transferring fluids in volumes on the order of nanolitres (Whitesides, 2006). Early attempts to build macroscopic fluidic devices possessing features similar to those of electronic circuits date back to 1960s (Foster and Parker, 1969). Thanks to rapid advancement of micro-fabrication techniques like soft lithography, the development of microfluidic technologies has been expanded enormously during last decade, most notably in fields like biotechnology, life sciences and pharmaceutical industry.

Downsizing the characteristic length scale of a process operation to an order of a few microns is attractive in many ways. A microfluidic device only requires a very small amount of operating fluid, which is ideal for biological and biomedical applications, often using fluids like blood, synovial liquid or saliva in very small quantities. Moreover, due to their high surface-to-volume ratio, micro-fabricated devices allow high heat transfer rates, so that exothermic reactions could be performed with an high efficiency and at a nearly constant temperature (Demello, 2006). Also, in a device with characteristic dimensions of only a few micrometers, several single operations can be integrated in a very tiny space, so that processes like the analysis, synthesis, separation and purification of samples could be unified within a single hand-sized apparatus. This means that microfluidic devices can potentially be thought of as self-consistent, automated and downsized "lab-on-a-chip" systems, capable of executing all possible laboratory tasks (Ouellette, 2003).

In order to allow for microfluidic technologies to become important for biology

and industry, it is necessary to have a better understanding of how complex fluids behave in microscopic flows. Many microfluidic operations, e.g. DNA sequencing or drop-on-demand inkjet printing, involve the use of fluids with a complex microstructure, and their non-Newtonian rheological response at fast flow conditions becomes evident. The zero-shear viscosity and relaxation time of dilute and semi-dilute polymer solutions are usually small, of a few mPa $\cdot$ s, and milliseconds respectively. When the characteristic size of the flow geometry, l, is of the order of a few micrometers, the characteristic time of viscous forces, $t_v = \frac{\rho l^2}{\eta_0}$, with ρ and η_0 being the fluid density and zero-shear viscosity respectively, can become comparable with an intrinsic relaxation time of the material, λ. t_v represents the timescale of the development of a steady velocity profile in a start-up Newtonian flow, see Bird et al. (2007). In this flow regime non-Newtonian flow effects can occur, as shown in the analysis of Denn and Porteous (1971) for the Maxwell fluid in a suddenly accelerated flow. The ratio λ/t_v is defined as the Elasticity number, *El*. The Elasticity number can also be expressed as $El = Wi/Re$, where $Wi = \lambda\dot{\gamma}$ is the Weissenberg number, and $Re = \frac{\rho\dot{\gamma}l^2}{\eta_0}$ is the Reynolds number, with $\dot{\gamma}$ being a nominal shear rate. It should be noticed that, as complex fluids can exhibit a broad relaxation spectrum, the value of Wi for a fixed deformation rate can greatly change, based on which relaxation time is chosen. For example, the $16.6c^*$ PAAm solution presented in this thesis has a spectrum of relaxation times, as measured by small amplitude oscillatory shear, comprised between 0.0027 ms and 83.93 ms. Thus, the value of the Weissenberg number for a fixed shear rate can spread across four orders of magnitude, leading to significant discrepancies in the interpretation of the experimental results. The longest fluid relaxation time is commonly used in the literature for defining the Weissenberg number in complex viscoelastic flows of polymer solutions. It can either be estimated using molecular theories, like the theory for dilute polymer solutions due to Zimm (1956) (see for example Rodd et al. (2007)), or measured experimentally, typically by capillary-force-driven extensional rheometry (CaBER, see Rodd et al. (2005b)). As observed by Clasen et al. (2006) and by Rodd et al. (2005a), the CaBER-measured longest relaxation time of polymer solutions in the

semi-dilute regime is approximately one order of magnitude higher than the one estimated by means of Zimm's theory. Such discrepancy must be taken into account as far as a comparison between the results presented in this thesis and previous publications is concerned. In the present work, the longest relaxation time measured by CaBER extensional rheometer, λ_{CaBER}, will be systematically used for defining Wi. This choice is motivated by the fact that the complex viscoelastic flows through three-dimensional contraction geometries presented in this thesis possess a strongly elongational character, which is proper also of CaBER experiments. λ_{CaBER} has been used for defining Wi in several previous studies of flows of polymer solutions through micro-fabricated contraction geometries (Rodd et al. (2005a), Miller and Cooper-White (2009), Haward et al. (2010a), Li et al. (2011)).

When flowing through micro-fabricated devices, even fluids which would behave in a Newtonian manner in macroscopic flow geometries can reach high Wi and low or moderate Re flow regimes. Under such conditions elastic forces are dominant, and therefore strongly non-linear, "turbulence-like" effects could be observed. These phenomena have been witnessed for the first time by Groisman et al. (2003), who developed two elementary microfluidic circuits based on the non-linear effects observable in the flow of an aqueous polymer solution through a microscopic rectifier. More recently, Rodd et al. (2005a), (2007) (2010) have investigated the flow of several polyethylene oxide (PEO) aqueous solutions through microchannels with an abrupt contraction, to reveal the onset of highly non-linear flow regimes upstream the contraction. The flow structure and stability greatly depends on both Wi and Re.

Studying such strongly non linear flow effects observable in microfluidics is important for several applications. For example inkjet printing, a very promising technology which allows for a precise deposition of polymeric materials on surfaces, involves the ejection of low viscosity fluids from nozzles with a diameter of $100\,\mu m$ or smaller, at shear rates of $10^5\,s^{-1}$ or higher (de Gans et al., 2004). The dynamics of the ejected ink drops depend on various parameters, like the size of the nozzle or the molecular weight of the polymer, and are still poorly understood at present.

Better understanding of the flow behaviour of polymer solutions in microscopic flows would permit to precisely establish the design principles of inkjet printheads.

On the other hand, microfluidic technology could also be used to create "micro-rheometers" capable of measuring the flow properties of even tiny amounts of low-viscosity fluids under large deformation rates, and with little inertial effects. These devices one day might replace traditional rheometric techniques in the characterization of materials typically undergoing high speed process operations, like inks, sprays and liquid crystals, or in the study of rare biomaterials like DNA solutions or biofluids (Pipe and McKinley, 2009).

Very few authors have studied the non-Newtonian flows in microscopic geometries by means of quantitative approach. Also, the most commercial rheometers cannot characterise weakly viscous fluids at high deformation rates relevant to industrial applications. In order to reach a deep understanding of the high Wi, moderate Re flow regime, it is necessary to link the nonlinear dynamics observed at a micrometers scale with the evolution of the fluid microstructure under flow. Therefore, this thesis will provide a quantitative investigation, from molecular characteristics of model fluids, materials functions measured under rheometric flows to flow characterisation including accurate velocity and pressure measurements in well-defined microscopic flow geometries. The full set of benchmark quantitative data produced by such a systematic approach will be useful for testing the validity of the predictions arising from molecular constitutive models, and for optimizing the design of devices like lab-on-a-chip essays, inkjet printers or micro-rheometers.

Chapter 2

Literature survey

2.1 Introduction

After the work of Groisman et al. (2003), several authors have investigated the high Weissenberg, moderate Reynolds numbers flow regime achievable in microfluidics throughout last decade, using various flow geometries, model fluids and characterisation techniques. The nonlinear response of polymer solutions in microscopic flow depends on a number of factors, e.g. the fluid microstructure, the details of the flow geometry and the imposed flow conditions. This Chapter briefly reviews the most significant published works on non-linear flow of complex fluids through microfluidic geometries.

Section 2.2 focuses on the rheology of polymer solutions. The criterion of dilute polymer solution arising from de Gennes theory, and a discussion on the rheological behaviour of polymer solutions under elongational and shear flows are given. In Section 2.3, the principles and the advantages of microfluidic shear rheometry are introduced. The literatures on the complex flow of polymer solutions through microfabricated sudden contractions are reviewed in Section 2.4. The key findings of the previous investigations on microfluidic flows of complex fluids are summarized in Section 2.5. The aim and the objectives, and the motivations of this thesis are listed in Section 2.6. The organization of this thesis is presented in Section 2.7.

2.2 Rheology of flexible polymer solutions

Simple fluids, like water, are formed by molecules with a size of just a few angstroms, and relax from a deformed state in extremely short times on the order of 10^{-12} s. Addition of an even small quantity of a hydrophilic polymer in water gives rise to a complex fluid, which possesses a mesoscopic length scale spanning from the dimensions of the monomers to the hydrodynamic radius. By example, when a flexible polyacrylamide chain with a molecular weight of $M_w = 5000000$ g/mol is dissolved in water, its size can be changed from $1.6{\cdot}10^{-7}$ m (at equilibrium) to $2{\cdot}10^{-4}$ m (fully extended) [1]. It is much bigger than the dimensions of the monomers or of the molecules of solvent. Therefore its relaxation from a deformed state requires a much longer time. As a consequence, the response of the polymer solution exhibits viscoelastic characteristics.

2.2.1 Concentration regimes

Apart from the elasticity of a single chain, the rheological behaviour of a polymer solution also depends on polymer-polymer and polymer-solvent interactions. de Gennes (1979) argued that the polymer chains in solution overlap at a concentration c^*, which can be estimated as:

$$c^* \cong \frac{M_w}{N_A R_g^3} \tag{2.1}$$

where M_w is the weight average molecular weight of polymer, N_A is Avogadro's constant and R_g is the radius of gyration. The latter is defined as the radius of a spherical surface with the same mass and moment of inertia of the polymer, and can be directly measured via light scattering (de Gennes, 1979; François et al., 1980).

It must be noticed that the transition between dilute and semi-dilute regime is not sharp and is often difficult to observe (Doi and Edwards, 1988). Moreover, the

[1] The equilibrium, mean square end-to-end distance for a polymer chain immersed in a solvent is estimated as $L_{eq} = \sqrt{\langle R_0^2 \rangle} = \sqrt{C_\infty n l^2}$, where n is the number of main bonds per unit of monomer, $l = 1.54\,\mathring{A}$ is the sp^3 bond length (Larson, 2005), and C_∞ is the "characteristic ratio". For PAAm molecules in water $C_\infty \cong 8.5$ (Bohdaneckỳ et al., 1983). The size of a fully extended PAAm chain is estimated as $L_{fe} \cong C_\infty n l$.

definition of c^* in Eq. 2.1 does not take in account of the polydispersity of the polymer sample.

In the *dilute* regime ($c/c^* << 1$) the polymer chains essentially act like self-avoiding walks, so that their dynamics are well described by the coarse-grained model due to Zimm (1956), which predicts that the longest relaxation time of the polymer solution is proportional to $M_w^{3\nu}$, where ν is the excluded volume exponent (Doi and Edwards, 1988). Zimm's predictions have been experimentally confirmed for several polymer-solvent systems under different flow conditions (see by example Keller and Odell (1985) and Perkins et al. (1994)). In the *semi-dilute* regime ($c \cong c^*$) the polymer molecules are also subjected to hydrodynamic interactions with the surrounding chains, so that the rheometric properties of the solution become concentration-dependent (de Gennes, 1979). By applying de Gennes' idea of "blob", it can be shown that, for a solution of monodisperse polymer in the semi-dilute regime, the ratio between the chain longest relaxation time λ and the Zimm relaxation time λ_{Zimm} scales with c/c^* as (Liu et al., 2009):

$$\frac{\lambda}{\lambda_{Zimm}} \propto (c/c^*)^{\frac{2-3\nu}{3\nu-1}}. \tag{2.2}$$

It must be noticed that the criterion for dilute polymer solution arising from the concept of overlap concentration only applies near equilibrium conditions which do not perturb very much the fluid microstructure. At sufficiently high deformation rates, the polymers unravel and the characteristic length of polymer chain becomes bigger than the one at near-equilibrium conditions. Thus, polymer-polymer interactions might occur even in a dilute polymer solution under flow conditions, as shown by the measurements in capillary-force-driven elongational flow of Clasen et al. (2006).

2.2.2 Elongational flows

Elongational flows of polymer solutions can be encountered in a large number of applications, including inkjet printing, fibre spinning, extrusion and enhanced oil recovery.

In a uniaxial elongational flow the velocity field $\underline{v} = (v_x, v_y, v_z)$ is given by:

$$v_x = \dot{\varepsilon} x \tag{2.3}$$

$$v_y = v_z = -\frac{\dot{\varepsilon}}{2} \tag{2.4}$$

where x is the flow direction and $\dot{\varepsilon}$ is the elongational rate (Larson, 2005). The most distinctive property of polymer solutions undergoing a pure elongational flow is a much stronger resistance than under shear flow. It can be quantified by means of the Trouton ratio $Tr = \frac{\eta_{el}}{\eta_0}$, with η_{el} being the elongational viscosity defined as $\eta_{el} = \frac{\sigma_{xx} - \sigma_{yy}}{\dot{\varepsilon}}$, where σ_{xx} and σ_{yy} are the stresses along the x and y directions respectively. Even aqueous polyethylene oxide (PEO) solutions with zero-shear viscosities $\eta_0 \cong 5 - 6\,\mathrm{mPa \cdot s}$ exhibit Trouton ratios $Tr = \frac{\eta_{el}}{\eta_0}$ much larger than unity at $\dot{\varepsilon} \cong 10^3\, s^{-1}$ (Cooper-White et al., 2002) .

The large stresses arising under elongational flow are a consequence of the polymer chains being aligned along the flow and stretched far away from their equilibrium configuration. Early theoretical investigations on the deformation of macromolecules in extensional flow were carried out by Ziabicki and Kedzierska (1959). Peterlin (1966) also showed that, at sufficiently large elongational rates, the characteristic size of a polymer chain in a dilute solution increases, so that very large Trouton ratios could be attained. The subsequent works of de Gennes (1974) and Larson and Magda (1989) predicted that a single, non-free-draining polymer chain in solution abruptly passes from a coiled state to a stretched state at a critical Weissenberg number $Wi = \lambda\dot{\varepsilon} = 0.5$. This suggests that, in order to observe large extensional stresses, it is necessary to impose elongational rates comparable with the inverse of the fluid relaxation time, and for a sufficient time to accumulate enough strain on the polymer chains. Designing rheometers capable of attaining such dual condition presents considerable difficulties, especially for weakly viscous, strain-hardening fluids.

For example, in case of the filament stretching rheometer (Sridhar et al., 1991), a fluid filament is elongated by means of two parallel plates moving apart to a maximum travel distance which sets a limit to the imposed strain. Moreover, for fluids

with shear viscosity close to that of water, inertial and gravitational effects can lead to a sagging of sample fluid which can be of great disturbance to the measurements (Anna et al., 2001). An alternate method to characterise the elongational flow of low viscosity polymer solutions is given by capillary-force-driven rheometry (Anna and McKinley, 2001; Rodd et al., 2005b), in which the thinning of a pre-strained fluid filament under the action of surface tension is monitored. The analysis of Entov and Hinch (1997), corroborated by the experimental results of Anna and McKinley (2001) for monodisperse polymer solutions, indicate that the capillary-force-driven thinning of an elastic fluid occurs at an elongational rate $\dot{\varepsilon} = \frac{2}{3\lambda_1}$, where λ_1 is the longest fluid relaxation time, thus at a Weissenberg number $Wi = \frac{2}{3}$ just above the critical value corresponding to the coil-stretch transition.

More promising solutions for characterising the elongational behaviour of low-viscosity complex fluids at sufficiently large values of Wi and of the strain arise from bulk rheometry, such as the flows through cross-slot devices. The presence of a stagnation point in a cross-slot flow geometry typically allows for reaching nominal strains on the order of 10^2 or above, and large elongational rates on the order of $10^3\, s^{-1}$, as demonstrated by (Haward et al., 2010b). Another relevant example is given by the complex flows through microscopic contraction geometries, in which the nominal Hencky strain can be adjusted by tuning the geometric details of the flowcell, while the nominal strain rate can be as high as $10^5\, s^{-1}$ or above (Rodd et al., 2005a; Oliveira et al., 2007). Such typology of flow presents several peculiarities, and will be discussed in detail in Section 2.4.

2.2.3 Shear flows

Shear flows are ubiquitous in practical applications, as they are found in all the processes in which materials slide past a surface.

In shear flows the velocity field $\underline{v} = (v_x, v_y, v_z)$ is defined by:

$$v_x = \dot{\gamma} y \tag{2.5}$$

$$v_y = v_z = 0 \tag{2.6}$$

where x, y and z are the flow direction, the velocity gradient direction and the vorticity direction respectively, and $\dot{\gamma}$ is the shear rate (Larson, 2005). A shear flow can be considered as a combination between a purely elongational and a purely rotational flow. Under such flow conditions, de Gennes (1974) predicted that a single polymer chains cannot reach a stable stretched state. This has also been experimentally observed for diluted solutions of DNA chains Smith et al. (1999). This suggests that the polymer chains under shear flow are less stretched than under an elongational flow with a same rate of deformation.

Using the so-called "Boger fluids" (i.e., dilute solutions of high molecular weight polymers in high viscosity solvents), it is possible to reach flow regimes with an high Weissenberg number $Wi = \lambda\dot{\gamma}$ and a low Reynolds number in conventional rheometers, so that purely elastic flow instabilities can be harnessed (Magda and Larson, 1988; Sousa et al., 2009). However, it is almost impossible to attain the same flow conditions with low viscosity aqueous polymer solutions in macroscopic devices. As those fluids have relaxation times on the order of 10^{-3} s and shear viscosities on the order of a few mPa $\cdot$ s, to achieve high Wi flow regimes it is necessary to impose shear rates of $10^4\, s^{-1}$. As the characteristic length of flow l is on the order of millimetres in macro-fabricated devices, at such high values of $\dot{\gamma}$ the Reynolds number $Re = \frac{\dot{\gamma} l^2}{\nu}$ is much bigger than the unity, leading to large inertial forces which are of great disturbance for the measurements of the fluid properties. Typical examples of inertial effects in macroscopic rheometers are the Taylor-Couette instability in Couette flows (Taylor, 1923; Rodd et al., 2005a), or the radial migration effect in plate-plate and cone-plate geometries (Connelly and Greener, 1985; Pipe et al., 2008).

2.3 Rheometric flows in microfluidics

Many industrial applications, like inkjet printing, coating or spraying, require rheometric data at high values of $\dot{\gamma}$. For example inks, typically shear-thinning fluids with zero-shear viscosities on the order of just a few mPa $\cdot$ s, can experience shear rates $\dot{\gamma} = 10^5\, s^{-1}$ or above while flowing through nozzles of printers (de Gans et al.,

2004). Although some authors suggest to reach such an high range of shear rates by means of conventional plate-plate rheometers with small gaps on the order of microns (Pipe et al., 2008; Rodd et al., 2010), a very promising alternative solution for characterizing the flow of low-viscosity fluids at large deformation rates is through microfluidic technologies.

The principle of operability of a microfluidic shear rheometer is essentially the same as for capillary rheometers: operating fluid flows through a pipe with a rectangular cross section with a depth h, a width w_c and a length L. The steady state pressure drop ΔP across the channel, measurable by means of pressure sensors, is correlated to the shear stress on the walls by a simple force balance:

$$\Delta P = \frac{2L(h + w_c)}{hw_c}\overline{\tau} \tag{2.7}$$

where $\overline{\tau}$ is the average wall shear stress. If h and w_c are on the order of μm, the ratio $\frac{2L(h+w_c)}{hw_c}$ is much bigger than unity, even if L is just on the order of mm. On the other hand, the nominal shear rate, defined as $\dot{\gamma} = \frac{2Q}{hw_c^2}$ can easily approach values $\dot{\gamma} \cong 10^4\, s^{-1}$ for flow rates on the order of ml/hr, while the Reynolds number $Re = \frac{\dot{\gamma} d_h^2}{\nu}$ remains low or moderate. Under such conditions, pumping low viscosity aqueous polymer solutions (for which $\eta_0 \cong 1\,\mathrm{mPa \cdot s}$ and $\lambda \cong 1 - 10$ ms) requires a typical pressure drop on the order of bars, allowing for precise measurements of shear stress in relatively modest flow rates. Thus, these devices can characterize low viscosity polymer solutions at very large deformation rates and with minimum inertial effects. Moreover, the channel volume $V = Lhw_c$ is less than a few μl, so that very little amounts of sample are required in principle. This feature makes micro-fabricated rheometers ideal for characterizing materials like biofluids (blood, DNA and others). Also, due to the very small characteristic size, viscous heating effects are negligible even in very high shear rates.

Very few researchers have characterized complex fluids under microfluidic shear flows. A typical approach consists in applying a known flow rate and then measuring the pressure drop. Kang et al. (2005) investigated the flow of polyethylene oxide (PEO) and cellulose solutions through a rectangular microchannel. By imposing

the flow rate with a syringe pump, it was possible to achieve shear rates as high as $10^7\,s^{-1}$, so that polymer degradation was observed in case of the PEO solution. Note that pressure drops across the flow geometry were measured here via an indirect method. By using *in situ* pressure sensors, Pipe et al. (2008) performed precise measurements of the shear viscosities of several complex fluids (a micellar and a Xantham Gum solution) through a microscopic straight channel geometry up to shear rates on the order of $10^4\,s^{-1}$. Conversely, it is possible to impose a known pressure and to measure the flow field through the flowcell. This approach was adopted by Masselon et al. (2008), who characterized the flow of a shear banding fluid through a microchannel with a large depth-to-width aspect ratio by means of particle-image velocimetry.

2.4 Complex flows in microfluidics

The flow of aqueous polymer solutions through micro-fabricated planar devices with a sudden contraction is of particular interest for many reasons. Firstly, these flows have an industrial and technological relevance, as they have several features in common with the jet of inks through printheads, or with the flows through porous media experienced by the solutions commonly used for enhanced oil recovery (Meinhart and Zhang, 2002; Jones and Walters, 1989). Secondly, the extensional rates experienced by the test fluid when passing through the contraction plane suggest that these geometries could be suitable for designing elongational micro-rheometers, as suggested by Oliveira et al. (2007). Thirdly, this geometry represents a useful benchmark flow problem for testing the validity of predictions arising from constitutive models of non-Newtonian fluids under very stringent flow conditions.

A schematic diagram of a typical contraction flow is given in Fig. 2.1. In the three-dimensional geometry, the fluid elements are strongly elongated near the contraction plane and predominantly sheared elsewhere. If the characteristic length of the flow geometry is on the order of microns, it could also be comparable to the size of a fully extended polymer chain. This unique feature makes microfludic contraction devices ideal for studying nonlinear viscoelastic fluid flows that could not be

harnessed in macroscopic flow geometries. One of the most interesting nonlinear viscoelastic flow phenomena is represented by the dynamics of the large recirculation regions in the upstream region, which appear in the corner of contraction ("corner vortices") and/or in the vicinity of the re-entrant lips ("lip vortices"), and are accompanied by a significant increase of the excess pressure drop across the entire geometry. On the other hand, in case of Newtonian flows large vortex structures can be observed only in the downstream region, as it has been documented in both experiments (Rodd et al., 2005a) and simulations Oliveira et al. (2008), whereas in the upstream contraction region, only very small vortices, so-called "Moffatt vortices", are present.

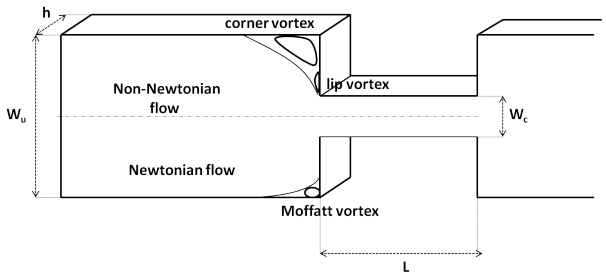

Figure 2.1: Schematic diagram of a typical flow through a sudden contraction.

2.4.1 Characteristic parameters

With reference to Fig. 2.1, it is clear that the flow behaviour of aqueous polymer solutions through a sudden planar contraction is related to several independent parameters, such as upstream and downstream widths w_u and w_c, the depth of channels h, the imposed flow rate Q and the rheometric properties of fluid, which can be tuned, for example, by changing the polymer concentration[2]. In order to define a viscoelastic flow, these five "degrees of freedom" need to be specified, e.g., a choice can be to assign the depth h, the upstream aspect ratio $\alpha = \frac{h}{w_u}$, the contraction ratio $\beta = \frac{w_u}{w_c}$ and the nominal Weissenberg and Elasticity numbers, Wi

[2]For simplicity's sake, this analysis does not take in account the length of downstream channel L_c. Such parameter has been recently proven to have an effect on the flow patterns observed upstream the contraction, see Rodd et al. (2010)

and *El*. The majority of previous studies defines *Wi* and *El* as:

$$Wi = \lambda \dot{\gamma}_c \tag{2.8}$$

$$El = \frac{Wi}{Re} = \frac{\lambda \eta_0}{\rho D_h h} \tag{2.9}$$

where $\dot{\gamma}_c = \frac{2Q}{hw_c^2}$ and $D_h = \frac{2hw_c}{h+w_c}$ are the nominal shear rate and hydraulic diameter of the downstream channel, and $Re = \frac{\rho Q D_h}{\eta_0 h w_c}$ is a characteristic Reynolds number. However, it should be remarked that this way of defining the Weissenberg and Elasticity numbers is quite arbitrary, and is motivated by the fact that the nominal shear rates in either downstream or upstream channels are in facts the only deformation rates that one can evaluate *a priori*. The major drawback of the definitions of *Wi* and *El* in Eq. 2.8 is that both the extensional rate and the fluid elongational viscosity, which are of primary importance in contraction flows, are not taken into account. The local extensional rate experienced by the fluid elements strongly depends on the nonlinear dynamics upstream the contraction, and therefore it cannot be estimated *a priori*. This suggests that a much more adequate definition of *Wi* could be obtained from quantitative measurements of the velocity field. From this viewpoint, quantitative time-resolved velocity field measurement techniques, e.g. micro-particle image velocimetry, could play an important role for better understanding of polymer dynamics in strong flow regime.

2.4.2 Role of fluid elasticity

Rodd et al. (2005a) have studied the effect of tuning the Elasticity number in a fixed micro-contraction flow geometry, using a 16 : 1 : 16 planar contraction-expansion microflow channel, several polyethylene oxide (PEO) aqueous solutions and streak videography. By changing both the polymer concentration (effectively changing the Elasticity number over a range $3.8 < El < 89$) and the flow rate, it was possible to identify several non-linear flow regimes (Newtonian-like flow, "inertio-elastic" instabilities, lip vortices, symmetric and/or asymmetric corner vortex growth) over a range of Weissenberg numbers up to $Wi = 548$. The results were summarized in a

Wi-Re diagram. It was observed that increasing *El* (thus decreasing flow inertia) at a fixed *Wi* made the elastic vortex structures more stable. The steady-state, mean extra pressure drops measured across the contraction channel were found to be very sensitive to the above mentioned flow regimes. In a subsequent work, same authors Rodd et al. (2007) explored another region of the *Wi-Re* space ($43 \leq El \leq 610$, $20 \geq Wi \geq 300$)[3] in an almost identical geometry than the previous one, simply by tuning the solvent viscosity of a PEO solution with fixed polymer concentration. Flow behaviours were characterized here using both streak photography and micro-particle image velocimetry (PIV), and essentially similar results as in the previous work were found. The observation that changing *El* affects the stability of elastic flow structures is in agreement with more recent studies through $8:1$ planar micro-contractions carried out by Haward et al. (2010a), for aPS-DOP solutions, and by Li et al. (2011) (see Table 2.2), for PEO solutions through a much more shallow geometry. Also, Miller and Cooper-White (2009) have shown that the presence of a surfactant in PEO solutions leads to elastic flow transitions to occur, in the same geometry, at *lower* values of *Wi* than what observed by Rodd et al. (2007), even for solutions in much lower *El* flow.

2.4.3 Effects of flow geometry on vortex growth mechanisms

The Hencky strain ϵ experienced by fluid elements through a contraction flow geometry is a function of the contraction ratio β ($\varepsilon = \ln \beta$ in case of planar contraction flows). This suggests that varying β might result in dramatic changes in the flow behaviour of viscoelastic fluids. Several studies in macro-fabricated contraction geometries have shown that the contraction ratio plays an important role in non-Newtonian flows. The experimental evidences from Evans and Walters (1986, 1989), using planar and square-square geometries over a range of contraction ratios ($4 \leq \beta \leq 80$), have shown that, while Boger fluids do not show any observable vortex growth mechanisms, shear-thinning PAAm solutions can produce corner vor-

[3]In order to compare the results of 2005 and 2007 papers of Rodd *et al*, the dimensionless flow parameters in the latter have been recalculated by using capillary rheometry, instead of the originally used Zimm relaxation time

tices that can also become asymmetric at high enough *Wi*. Lip vortices, if present, were found at relatively low flow rates before being enveloped in much larger corner recirculations, with their sizes strongly increasing with *Wi*. Such a lip-to-corner vortex transition was also found in the 2D creeping flow simulations based on the Phan-Thien Tanner (PTT) model by Alves et al. (2004) for shear-thinning liquids through planar contractions with $10 \leq \beta \leq 100$. The authors mapped their results in a $\beta - Wi$ diagram to show that, for $\beta < 10$, just corner vortices are present, and, for $\beta \geq 10$, lip and corner vortices coexist in a window of *Wi*. This is consistent with the work of Gulati et al. (2008), who observed very symmetric and stable corner vortices in the flow of a DNA solution through a $2:1$ planar contraction flow, over a range of $0.8 \leq Wi \leq 700$. On the other hand, the PTT model-based 3D flow simulations of Omowunmi and Yuan (2010) for a shear-thinning solution through a $8:1$ contraction have demonstrated that tuning the aspect ratio has an effect on the vortex growth phenomena: lip vortices only occurs in shallow flow geometries with low aspect ratio $\alpha \leq 1/4$, and are absent in high aspect ratio flow geometries ($\alpha \geq 1/2$).

It is interesting to notice that, in all the above mentioned previous works, changing a geometric parameter (either α or β) also resulted in a change of *El*, which in turns has an effect on stability of elastic flow structures, as discussed in Section 2.4.2. Thus, future studies on the effect of the aspect ratio (or of the contraction ratio) on dynamics of complex fluids in contraction flows with a uniform depth and in a given range of *Wi* should be carried out at fixed β (or α) and *El*.

2.5 Summary of the previous related works

Some of the most significant works published during last decade concerning the high *Wi*, moderate *Re* flow regime achievable in microfluidics are summarized in Table 2.1 and in Table 2.2. The tables list, for each published work, the characteristics of employed flowcell(s) (either straight microchannel, contraction-expansion or cross-slit), the model fluids, the range of *Wi* and *El*, the results of molecular and rheometric characterisation (if reported), the techniques used to study the microscopic flows

and the key results.

The model fluids are mainly solutions of flexible polymers such as polyethylene oxide (PEO), polyacrylamide (PAAm) or DNA, and micellar solutions (see for example Masselon et al. (2008) and Pipe et al. (2008)). The availability of molecular and rheometric data is very limited, with the notable exception of the recent work of Li et al. (2011). Moreover, the rheometric properties were characterized in most of cases over a range of shear rates ($\dot{\gamma} \leq 10^3\, s^{-1}$) that is of little relevance to microfluidic applications. Measurements at higher shear rates have been achieved in very few cases using the ARES-G2 rheometer (see (Miller and Cooper-White, 2009; Rodd et al., 2010)), or microfluidic Poiseuille flows (Pipe et al., 2008). Also, the full relaxation spectrum of the model fluids over a sufficiently large range of frequencies has been reported only by Gulati et al. (2008).

The flow field in microfluidics has been studied either qualitatively, by means of streak imaging (Rodd et al., 2005a; Miller and Cooper-White, 2009), or quantitatively, by means of micro-particle image velocimetry ($\mu - PIV$) (Arratia et al., 2006; Masselon et al., 2008; Li et al., 2011). A combination of $\mu - PIV$ and of birefringence measurements has also been reported by Haward et al. (2010a).

It should also be noticed that very little effort has been made to analyze the quantitative data with respect to the nonlinear dynamics observable in microscopic flows. This is particularly evident in the study of contraction flows, where only a simplified analysis, like studying the effect of the vortex flow structures on the velocity profiles measured along the flow axis, has been carried out (see by example Rodd et al. (2007) and Li et al. (2011)). More insightful and systematic methods for quantitative analysis have not been proposed.

Author(s) and year	**Flow geometry**	***El* range and *Wi* range**	**Materials**	**Molecular characterisation**	**Rheometric characterisation**	**Flow characterisation and key findings**
Kang et al. (2005)	Rectangular duct with an hydraulic diameter $D_h = 188\,\mu m$	Not reported	2 wt.% PEO, 1 wt% cellulose aqueous solutions	Not reported	Shear viscosities up to $\dot{\gamma} = 10^7\,s^{-1}$	No velocity measurements or flow imaging. The studied geometry was used to measure the shear viscosities up to very high shear rates
Rodd et al. (2005a)	16 : 1 : 16 planar contraction (upstream channel aspect ratio $\alpha = 1/8$, upstream channel width $w_u = 400\,\mu m$, downstream channel length $L_c = 100\,\mu m$)	$3.8 \leq El \leq 89$, $1 \leq Wi \leq 548$	PEO ($M_w = 2M$), $0.58 \leq c/c^* \leq 3.5$	Not reported	Shear viscosities up to $\dot{\gamma} \cong 10^3\,s^{-1}$, relaxation times measured via capillary break-up extensional rheometer (CaBER)	Used streak imaging and pressure drop measurements to characterize a variety of elastic flow regimes upstream the contraction. The size, shape and stability of the vortices depend on both *Wi* and *El*. The pressure drops across the contraction were found to be very sensitive to the flow regimes
Arratia et al. (2006)	Cross slot. Each channel has a width $w = 650\,\mu m$ and a depth $h = 500\,\mu m$.	*El* not reported $1.2 \leq Wi \leq 26.4$, as deducted from measured velocity field	0.2 wt.% PAAm ($M_w = 18M$) in a water-glycerol solvent	Not reported	Zero-shear viscosity and first normal stress difference at low shear rates	Used particle tracking and micro-particle image velocimetry ($\mu - PIV$) to observe two novel elastic flow instabilities
Rodd et al. (2007)	Approximately the same as Rodd et al. (2005a)	$3 \leq El \leq 68$, $0.4 \leq Wi \leq 42$	PEO ($M_w = 2M$) in several water-glycerol solutions	Reported the polydispersity index of the polymer as indicated by the supplier	Zero-shear viscosities and CaBER relaxation times. Used the Zimm relaxation times to define *Wi* and *El*	Used both streak imaging and micro-particle image velocimetry. Reported the effect of the elastic flow regimes on the centreline velocity profiles for various *Wi* and two different El numbers
Masselon et al. (2008)	Straight microchannel featuring a very large aspect ratio (width = $200\,\mu m$, depth = 1 mm)	Not reported	Two micellar solutions	Not reported	Shear stress measurements up to $\dot{\gamma} \cong 50\,s^{-1}$	Velocity measurements in microchannel flow. The local velocity gradients are used to show that the shear stress does not monotonically depend on shear rate
Pipe et al. (2008)	Two straight microchannels with a width of a few mm and depths of 246 and 507 μm respectively.	Not reported	0.1 wt.% PEO ($M_w = 2M$) in water-glycerol solvent, Xantan gum and a CpyCl/NaCal wormlike micellar solution	Not reported	Shear viscosities measured up to $\dot{\gamma} \cong 10^4\,s^{-1}$	No flow visualization data. A combination of commercial rheometers and microchannels is used for measuring the shear viscosity up to very high deformation rates

Table 2.1: A brief review of previous works which have experimentally investigated the non-linear flow regime achievable in microfluidics.

Author(s) and year	**Flow geometry**	***El* range and *Wi* range**	**Materials**	**Molecular characterisation**	**Rheometric characterisation**	**Flow characterisation and key findings**
Gulati et al. (2008)	2 : 1 planar contraction (Upstream aspect ratio is $\alpha = 0.9$, upstream channel width $w_u = 200\,\mu m$, downstream channel length $L_c = 0.75$ cm)	$10^3 \leq El \leq 10^6$, $1 \leq Wi \leq 630$	a DNA aqueous solution ($c/c^* = 4$)	Not reported	Shear viscosities, viscous and elastic modulus over a range of shear rates $10^{-2} \leq \dot{\gamma} \leq 2 * 10^2\, s^{-1}$	Used both streak imaging and digital particle image velocimetry (DPIV). Visualized very symmetric and stable corner vortices upstream the contraction for $42 \leq Wi \leq 629$. The centreline velocity profiles are sensitive to Wi
Miller and Cooper-White (2009)	Same as Rodd et al. (2005a)	$6.2 \leq El \leq 612$, $4 \leq Wi \leq 300$	Several PEO-surfactant aqueous solutions.	Not reported	Steady state shear viscosities and viscous and elastic moduli, as measured with an ARES-G2 rheometer, over a range $40 \leq \dot{\gamma} \leq 10^4 s^{-1}$. CaBER relaxation times	Studied the flow via streak imaging. In contrast with previous works that used PEO-water solutions, polymer-surfactant systems show much more stable vortex regions, which start to appear at lower Wi
Haward et al. (2010a)	8 : 1 planar contraction (upstream aspect ratio $w_u/h = 0.5$, upstream width $w_u = 1.6$ mm, downstream channel length $L_c = 2$ mm	$31 \leq El \leq 295$, $8.7 \leq Wi \leq 1562$	Several dilute and semi-dilute atactyc polystyrene (aPS, $M_w = 6.9$ millions) solutions in dioctyl phthalate (DOP)	Reported the the polydispersity index ($M_w/M_n = 1.15$) of the aPS as suggested by the supplier	Shear viscosities over a range $1 \leq \dot{\gamma} \leq 10^3\, s^{-1}$, CaBER relaxation times	Used $\mu - PIV$, birefringence measurements and pressure drops across the channel to study the flow field. Increasing the Elasticity number at an approximate equality of Wi leads to more stable PIV-generated streamlines. Pressure drops and local birefringence are sensitive to the flow regime
Li et al. (2011)	8 : 1 planar sudden contraction (upstream aspect ratio $\alpha = 9/160$, upstream channel width $w_u = 800\,\mu m$, downstream channel length $L_c = 40$ mm)	$20 \leq El \leq 120$, $7 \leq Wi \leq 121$	Four PEO aqueous solutions ($M_w = 4.82M$, $15 \leq c/c^* \leq 22.5$)	Reported the molecular characteristics as measured by means of gel-permeation chromatography (GPC). In particular, the polydispersity index is $M_w/M_n = 7.50$.	A comprehensive set of data, including: the viscous and the elastic modulus measured over a range of frequencies $10^{-1} \leq \omega \leq 10^5$ Hz with both an ARES and a piezoelastic axial vibrator (PAV); shear viscosities measured over a range of shear rates $1 \leq \dot{\gamma} \leq 10^3\, s^{-1}$; CaBER relaxation times; elongational viscosity of one solution measured in a cross-slot device	Used $\mu - PIV$ and pressure drop measurements to quantitatively characterize the flow field upstream the contraction. Several flow regimes have been classified. The effect of increasing Wi on the centreline velocity profiles has been analyzed for two values of El. The extra pressure drops across the contraction are sensitive to the nominal Wi

Table 2.2: A brief review of previous works which have experimentally investigated the non-linear flow regime achievable in microfluidics (*Continued*).

2.6 Aims, objectives and motivation of the present work

The aim of present work is to quantitatively investigate the nonlinear dynamics of semi-dilute polymer solutions in microfluidics in the high Weissenberg, moderate Reynolds number flow regime using molecularly and rheometrically well-characterized, highly polydisperse polyacrylamide aqueous solutions. To achieve this, the following

objectives have been addressed:

1. The molecular properties of model polymer and the rheometric properties of polymer solutions under a variety of standard flows have been fully characterized.

2. A platform capable of simultaneously performing precise measurements of pressure drops and velocity fields in microscopic flows has been developed.

3. Nonlinear flows of the model fluids through several microscopic geometries have been quantitatively investigated over a wide range of Weissenberg numbers ($Wi \leq 120$) and Elasticity numbers ($13.3 \leq El \leq 476.8$).

4. A novel method for analyzing velocity measurements in microfluidics has been proposed and validated. It can produce a snapshot image to reveal a stretch intensity map of polymer chains across flow domain from velocity field data at any given instant. Such technique has thus been used to extract useful quantitative information from the available $\mu - PIV$ data.

The motivation of this study lies in the fact that, in order to reach an insightful understanding of the highly nonlinear dynamics in microfluidics, it is necessary to bridge the considerable knowledge gap between the molecular dynamics and the flow behaviour of complex fluids in micro-fabricated devices. A full quantitative study of model polymer solutions, ranging from molecular to rheometric and flow characterisations through benchmark flow geometries, is a first step towards such an important aim. The outcomes of this work will thus facilitate rationalizing the design principles of microfluidic technologies (e.g. microrheometers, inkjet printers, lab-on-a-chip essays and so on), and will be useful to validate constitutive models for semi-dilute polymer solutions under well-defined flow conditions.

2.7 Organization of this thesis

This thesis is organized as follows.

Chapter 3 describes the experimental techniques for quantitative investigation adopted in this thesis. These include: a Gel-Permeation Chromatography (GPC) molecular analysis system; several commercial rheometers, including ARES, Vilastic-3, Piezoelastix Axial Vibrator (PAV) and Capillary Break-Up Extensional Rheometer (CaBER); a variety of microfluidic flow geometries; sensors for *in situ* pressure measurements in microscopic flow; a micro-particle image velocimetry ($\mu - PIV$) system for velocity measurements.

Chapter 4 presents the results of the molecular analysis and of the rheometric characterisation of the model PAAm aqueous solutions. GPC revealed the high molecular weight and high polydispersity of model polymer. The rheometric properties of the PAAm solutions under steady shear, SAOS and capillary-force-driven elongational flow are presented. The linear mechanical spectroscopy of a PAAm solution over a broad range of frequencies ($0.1 \leq \omega \leq 6650$ Hz) are obtained from Vilastic-3 and PAV measurements. ARES rheometer and a novel microfluidic device produced the shear viscosity data of the model fluids over a large range of shear rates ($0.1 \leq \dot{\gamma} \leq 4 \times 10^4 s^{-1}$).

Chapter 5 contains the results of quantitative characterisation of the flow of three PAAm aqueous solutions through several benchmark flow geometries. The flows through a straight microchannel and three micro-fabricated 4:1:4, 8:1:8 and 16:1:16 contraction-expansion flowcells have been studied over a wide range of Elasticity numbers ($13.3 \leq El \leq 476.8$) and Weissenberg numbers ($1.4 \leq Wi \leq 131.7$). The effects of Elasticity number on the observed elastic vortex structures have been investigated for various flow geometries. Also, the details of the velocity fields and the excess pressure drops across the contraction-expansion geometries in various flow regimes have been studied. Part of the contents of Chapter 4 and of Chapter 5 constitute the main body of a paper recently submitted to the Journal of Non-Newtonian Fluid Mechanics.

Chapter 6 introduces a general method for analyzing velocimetry data from complex flows. It leads to the definition of a "local Deborah number", which is a a degree of polymer chains being stretched away from their equilibrium conformation along

the streamlines. Hence a snapshot image for the spatial distribution of polymer conformation across complex flow domain at any given instant can be mapped out from the corresponding velocity field. By applying such novel technique, an useful amount of extra quantitative information was extracted from the velocity measurements presented in Chapter 5. The technique has also been used to critically evaluate the appropriateness of the nominal dimensionless parameters commonly used in the literature in the study of complex viscoelastic flows.

Finally, in Chapter 7 the key results of this thesis are summarized, conclusions are drawn and some suggestions for future work are given.

Chapter 3

Experimental Methodology

3.1 Introduction

This Chapter provides a detailed description of the experimental methods to quantitatively characterize the molecular properties, the material functions and the flow behaviour of polymer solutions in microfluidics.

Section 3.2 describes the principles of the gel-permeation-chromatography (GPC) technique used to perform the molecular analysis. Section 3.3 focuses on the experimental techniques to measure rheometric properties under steady and small amplitude oscillatory shear flows, squeeze flow under piezoelastic-axial vibration (PAV), and capillary break-up extensional flow. The limitations of commercial devices (ARES rheometer with double-wall Couette, Vilastic-3 Analyzer) in the characterisation of low-viscosity fluids at high shear rates are discussed. Section 3.5 focuses on a technique to measure pressure drops in microfluidics. Section 3.6 gives a detailed description of the micro-particle image velocimetry ($\mu - PIV$) system for quantitative velocity measurements in complex microfluidic flows. The spatial resolution of $\mu - PIV$ experiments is discussed. The experimental validation is also presented.

3.2 Model polymer sample and GPC technique

1wt.% (5M) PAAm aqueous solution was purchased from Polysciences Europe GmbH and used as received. The molecular characterisation of the polymer was performed by means of a gel-permeation chromatographic (GPC) system. GPC, also known as molecular-exclusion chromatography, is a technique which separates molecules based on their size. It is particularly appropriate to characterize polymers with an average molecular weight higher than 2000 g/mol, and a molecular size in a range from 30 up to 400 nm (Harris, 2003).

In GPC, polymer sample in a form of its dilute solution is pumped at a constant flow rate (usually smaller than 1 ml/min) through a column containing a stationary phase. This medium is given by numerous micro particles, forming micro-pores which can only be penetrated by some smaller molecules. Thus, large molecules are not trapped by stationary phase and are quickly eluted, while smaller molecules are eluted after a longer time. A detector, located at the bottom of the column, measures the refractive index of eluate, proportional to the polymer concentration, as a function of time. For a given stationary phase, a quantitative relationship between the elution volume, V_e, and the molecular weight of polymer, the so-called calibration curve, can be established through GPC measurements using standard polymer samples with known molecular weight and nearly monodispersity (Harris, 2003). By comparing the measured V_e of an unknown eluate with the calibration curve, the molecular weight and distribution of molecular weight of the polymer sample can be calculated.

The resolution of a GPC column is dependent on the column length, the particle size and the pore size. In this work, a high-performance TSK G6000 PW column from Tosoh Bioscence with a carefully controlled pore size ($ID = 7.5$ mm, length $= 60$ cm, mean particle size $= 17\,\mu m$, mean pore size > 100 nm, calibration range up to 8000000 g/mol) was used. GPC flow was controlled by a Waters 510 pump, and an ERC 751A 125 differential refractometer was used as a detector. Deionised water was used as a solvent.

3.3 Rheometric characterization

3.3.1 Shear flow in Couette geometry

Steady shear viscosities over a range of low and medium shear rates ($0.2 \leq \dot{\gamma} \leq 1200\, s^{-1}$) were characterized by an ARES rheometer (TA instruments) equipped with a double-wall Couette geometry. A schematic diagram of this system is shown in Fig. 3.1.

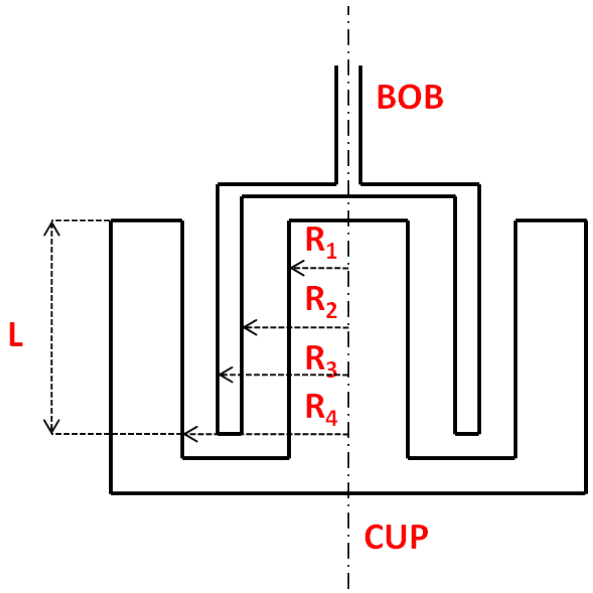

Figure 3.1: Schematic diagram of the double-wall Couette geometry employed in this work. Here $R_1 = 13.975$ mm, $R_2 = 14.75$ mm, $R_3 = 16$ mm, $R_4 = 17$ mm, and the effective bob length is $L = 31.9$ mm.

The sample is loaded in the space between the lower (*cup*) and the upper (*bob*) tools. The cup is connected to a machine motor, which imposes an angular velocity $\dot{\theta}$, and the bob is connected to a force transducer which measures the torque T, with a measurement range $2 \cdot 10^{-7} N \cdot m \leq T \leq 2 \cdot 10^{-2} N \cdot m$. $\dot{\theta}$ is related to the nominal shear rate $\dot{\gamma}$ by:

$$\dot{\gamma} = \dot{\theta} \left[\frac{1}{(\frac{R_2}{R_1})^2 - 1} + \frac{1}{1 - (\frac{R_3}{R_4})^2} \right] \tag{3.1}$$

and T is related to the nominal, averaged measured shear stress $\overline{\tau}$ by a simple expression:

$$T = \tau_1 2\pi R_2^2 L + \tau_2 2\pi R_3^2 L = \overline{\tau} 2\pi L (R_2^2 + R_3^2) \tag{3.2}$$

where τ_1 and τ_2 are the shear stress on the inner and outer surfaces of bob re-

spectively. The range of measurable shear stresses for this geometry is thus is $0.002 \leq \tau \leq 21.1$ Pa. Because of a relatively large measurement surface in comparison with other geometries, like truncated cone or parallel plates, the double-wall Couette tools are particularly suitable in rheological characterisation of low viscosity fluids. An upper limit to the measurable shear viscosity $\eta = \frac{\overline{\tau}}{\dot{\gamma}}$ is given by the well-known inertial instability observed for the first time by Taylor (1923). It leads to a false increase of apparent shear viscosity at high shear rates. The analysis of Larson (1992) predicts that, for a single-gap Couette geometry, these inertial effects become important at $2Re^2\varepsilon \cong 3430$, where $\varepsilon = \frac{R_2 - R_1}{R_1}$ and $Re = \frac{\rho\dot{\gamma}(R_2-R_1)^2}{\eta}$ is a characteristic Reynolds number. The criterion for the onset of the inertial instability in the double-wall Couette geometry used in this work is thus given by $\eta = 3.43 \cdot 10^{-6}\dot{\gamma}$, if a density $\rho \cong 1000\, Kg/m^3$ is assumed.

3.3.2 Oscillatory shear flow in capillary geometry

The linear viscoelastic characterisation of polymer solutions over a range of low and medium frequencies $0.1 \text{ Hz} \leq \omega \leq 10 \text{ Hz}$ was performed by a Vilastic-3 Viscoelasticity Analyzer (Vilastic Scientific Inc.). It imposes an oscillatory flow to a fluid sample loaded in a vertically placed capillary tube, and measures the pressure drop of the fluid flow. In shear flow experiments, the sample fills up a measurement tube, with a circular cross section of radius $R = 0.05$ cm and length $L = 6.4$ cm, and is forced to flow at a given oscillatory flow rate $Q(t) = Q_0 \sin(\omega t)$ by a coupling fluid (usually water). A sensor measures the pressure drop between the two ends of tube. Following the theoretical analysis by Thurston (1975), the pressure drop between upper and lower part of tube, ΔP, is related to the wall shear stress τ by the following momentum balance:

$$\Delta P \pi R^2 - \tau 2\pi RL = \rho L \frac{dQ}{dt}. \tag{3.3}$$

From Eq. 3.3, the relationships between the components of ΔP in-phase and out-of-phase with $Q(t)$ (denoted as $\Delta P'$ and $\Delta P''$ respectively), and the viscous modulus

G'' and the elastic modulus G' can be derived as:

$$\Delta P' = \frac{2L}{R}\omega G''\dot{\gamma} \tag{3.4}$$

$$\Delta P'' = \left(\frac{R\rho\omega}{3} - \frac{2\omega G'}{R}\right) L\dot{\gamma} \tag{3.5}$$

where $\dot{\gamma} = \frac{4Q_0}{\pi R^3}$ is the nominal shear rate at the wall and $\gamma = \dot{\gamma}/\omega$ is the nominal strain. This machine can perform dynamic tests with frequency over a range $0.01 \leq \omega \leq 100$ Hz and nominal strains over a range $0.001 \leq \gamma \leq 100$. It can measure dynamic viscosities $\eta' = \omega G''$ on a range $0.0005\,Pa \cdot s \leq \eta' \leq 50\,Pa \cdot s$, and an "elasticity" $\eta'' = \omega G'$ as low as $\frac{1}{100}$ of η'. The minimum measurable shear stress is $\tau_{min} = \eta_{min} \cdot \gamma_{0,min} \cdot \omega_{min} \cong 3 \cdot 10^{-8}$ Pa, significantly lower than the τ_{min} measurable with the ARES rheometer equipped with double Couette. Such a high sensitivity, together with the imposed oscillatory shear flow, makes Vilastic-3 ideal for performing the viscoelastic characterisation of low-viscosity fluids. This rheometer is very useful for characterising the rheology of blood in nearly physiological conditions (Chang et al., 2002; Thurston and Henderson, 2006).

3.3.3 Oscillatory shear flow at high frequecies

The linear viscoelastic characterisation of model fluids over a range of high frequencies $10^2 < \omega < 5 \cdot 10^5$ Hz was performed by a Piezoelastic Axial Vibrator (PAV). It is essentially a squeeze-flow rheometer to oscillate testing fluid between two parallel plates. The lower plate is connected to a piezoelastic actuator, which imposes a known oscillatory force F, with a frequency f between 1 and 6000 Hz. The consequent displacement of lower plate when no fluid is loaded, x_0, is measured. Sample to be characterized is positioned between the two plates in a latter time, and the lower plate displacement x at a same F is measured. The ratio x/x_0 can be correlated to the complex squeeze stiffness K^* of the model fluid at the imposed frequency. For an incompressible fluid in the linear viscoelastic regime, K^* is correlated with the complex modulus of the fluid at a given frequency ω, $G(\omega)^* = G'(\omega) + iG''(\omega)$ by

the formula of Kirschenmann and Pechhold (2002):

$$K^* = \frac{2}{3\pi}\frac{d^3}{R^4}\left[\frac{1}{G^*} + \frac{3}{2}\left(R/d\right)^2 k^*\right] \tag{3.6}$$

where $5 \leq d \leq 200\,\mu m$ and $R = 10$ mm is the gap between the plates, $R = 10$ mm is the plates radius, ρ is the fluid density and k^* is the dynamic compressibility of the fluid, which becomes important for low viscosity fluids in the high frequency range (Vadillo et al., 2010). k^* can be determined by performing several experiments at different values of d, thus G^* is accurately measured across all the frequency range of the PAV. This technique has been proven to provide a reliable viscoelastic characterization of fluids like colloidal suspensions and low viscosity inks (Crassous et al., 2005; Vadillo et al., 2010) at frequencies up to several KHz. Therefore, PAV enables to extend the measurement range towards a high frequency range not achievable by conventional rheometric techniques, which can only provide reliable viscoelastic data at frequencies not higher than 40-50 Hz.

3.3.4 Capillary-driven extensional flow

The elongational properties of model fluids were tested by means of a Capillary Break-Up Extensional Rheometer (CaBER, Thermo Fisher Scientific). The principle of measurement of CaBER is depicted in Fig. 3.2.

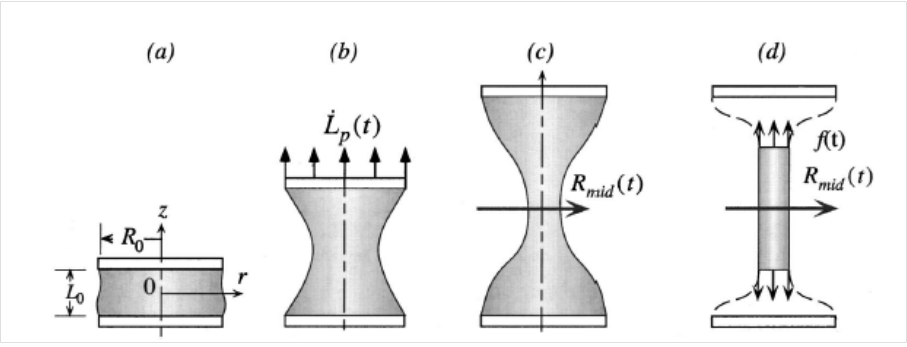

Figure 3.2: A scheme of measurement procedure of CaBER rheometer: after an initial extension with a rate of $\dot{L}_P$, the sample diameter, whose thinning is driven by surface tension, is monitored by a laser detector (McKinley and Tripathi, 2000)
.

The essential components of the CaBER are two plates with fixed radius R

and an infrared laser micrometer. The upper plate is connected to a motor which allows for vertical motion. The material to be studied is loaded between the plates, which are positioned at an initial distance L_0 (Fig. 3.2a). At $t = 0$, the upper plate is put in motion with a velocity $\dot{L}_p$, so that the fluid sample is necked (Fig. 3.2b). At a $t > 0$, after the gap between the plates has reached a final value L, the imposed strain ends, and the evolution of the midfilament diameter of the sample $D_{mid}(t)$ is monitored by the laser detector (Fig. 3.2 (c) and (d)). Plates with radius $R_0 = 2$ or 3 mm could be used, and the minimum diameter measurable by laser micrometer is $D_{min} \cong 10\,\mu m$. The break-up mechanism of filament is strongly dependent on rheological properties of sample itself, and has been studied for both Newtonian fluids and polymer solutions by several authors (McKinley and Tripathi, 2000; Anna and McKinley, 2001; Rodd et al., 2005b). While the diameter of Newtonian fluids is always axially non-uniform until break-up occurs (Fig. 3.2 (c)), by adding an even small quantity of a long-chain polymer to a Newtonian solvent, it is possible to observe an *elastic regime* in filament thinning. Under these conditions, the filament becomes almost axially uniform and much longer persistent in time (Fig. 3.2 (d)).

Apart from the rheometric properties of fluid, there are a number of factors that need to be considered for better CaBER measurements, and will be discussed below.

Capillary length

A particular care must be taken in choice of plates radius R_0 and initial distance L_0. In order to prevent a collapse of the initially loaded fluid column under the action of gravity, L_0 should not be bigger than the *capillary length* $L_{cap} = \sqrt{\frac{\sigma}{\rho g}}$, i.e. $L_0 \leq L_{cap}$. Following Slobozhanin and Perales (1993), this criterion can be arranged as:

$$\frac{R_0}{L_0} \leq \frac{1}{\sqrt{Bo}} \tag{3.7}$$

where $Bo = \frac{\rho g R_0^2}{\sigma}$ is the characteristic *Bond* number.

Characteristic timescales

CaBER experiments possess several characteristic times. The first is the viscous characteristic break-up time. Liang and Mackley (1994) showed that the mid-filament diameter D_{mid} of a Newtonian liquid filament decays linearly with time under the action of capillary forces:

$$D_{mid}(t) = D_0 - \frac{\sigma t}{3\eta_0} \tag{3.8}$$

where t is the time. The characteristic timescale of a viscous filament decay is thus $t_v \cong \frac{\eta D_0}{2\sigma}$. Other characteristic times of CaBER experiments are given by the intrinsic relaxation times of testing fluids. A relaxation time λ can be extracted by fitting the measured midfilament diameter in elastic regime with the theoretical predictions given by Bazilevsky et al. (1988) and by Anna and McKinley (2001), which suggest $D_{mid} \propto \exp(-\frac{t}{3\lambda})$. A third fundamental timescale is the Rayleigh break-up time t_R, which is essentially the break-up timescale for a non-viscous liquid jet. Its expression is given by the seminal work of Rayleigh (1879):

$$t_R = \sqrt{\frac{\rho R_0^3}{\sigma}}. \tag{3.9}$$

From these three characteristic times, it is possible to define some important non-dimensional groups characterizing the capillary-force-driven experiments. The first one is the *Ohnesorge* number, which is defined as the ratio of the viscous time to the Rayleigh time (Ohnesorge, 1936; Rodd et al., 2005b):

$$Oh = \frac{\eta_0}{\sqrt{\rho \sigma R_0}}. \tag{3.10}$$

If $Oh << 1$, Rayleigh analysis for inviscid liquid jets becomes valid and the filament break-up process becomes dominated only by inertial forces. Thus, capillary break-up rheometry is only applicable to "viscous enough" materials, for which Oh is not excessively small. On the other hand, the ratio between λ and t_v defines the

elasto-capillary number Ec (Clasen et al., 2006):

$$Ec = \frac{\lambda\sigma}{\eta_0 R_0}. \tag{3.11}$$

It is a measure for the relative duration of elastic and viscous regimes in CaBER measurements of complex fluids.

3.4 Microfluidic flow geometries

Four different microfluidic flow geometries were used in this work: three contraction-expansion flow channels with the contraction ratio $\beta = 4, 8$ and 16 and labelled as Flowcell $1, 2$ and 3 respectively, and one straight channel of length L = 25 mm, width $w = 100\,\mu m$ and depth $h = 48.5\,\mu m$, labelled as Flowcell 4. Characteristic dimensions are given in Table 3.1, and a schematic diagram of Flowcell $1, 2$ and 3 is presented in Fig. 3.3. The microfluidic chips are made of poly(methyl methacrylate) (PMMA) and aromatic epoxy, and were fabricated by standard soft lithographic method (Epigem Ltd, UK). The internal surfaces were treated by oxygen plasma to make them hydrophilic. The length L of the narrow channel in the Flowcells 1,2, and 3 was set to be 20 mm so that the ratio L/w_c is much larger than unity for each geometry. Such a design minimizes the effects of flow dynamics in the downstream expansion section on the flow dynamics in the upstream contraction region. Two pressure taps were deployed at P_1 and P_2 positions, which are 45 mm apart and symmetrically located with respect to the centre of the narrow channel, to measure the pressure drop across the contraction-expansion flow. The inlet and outlet of the flow channel were located far away from the contraction and expansion planes. Fluid flows were driven by a Nexus 5000 high force syringe pump (Chemyx).

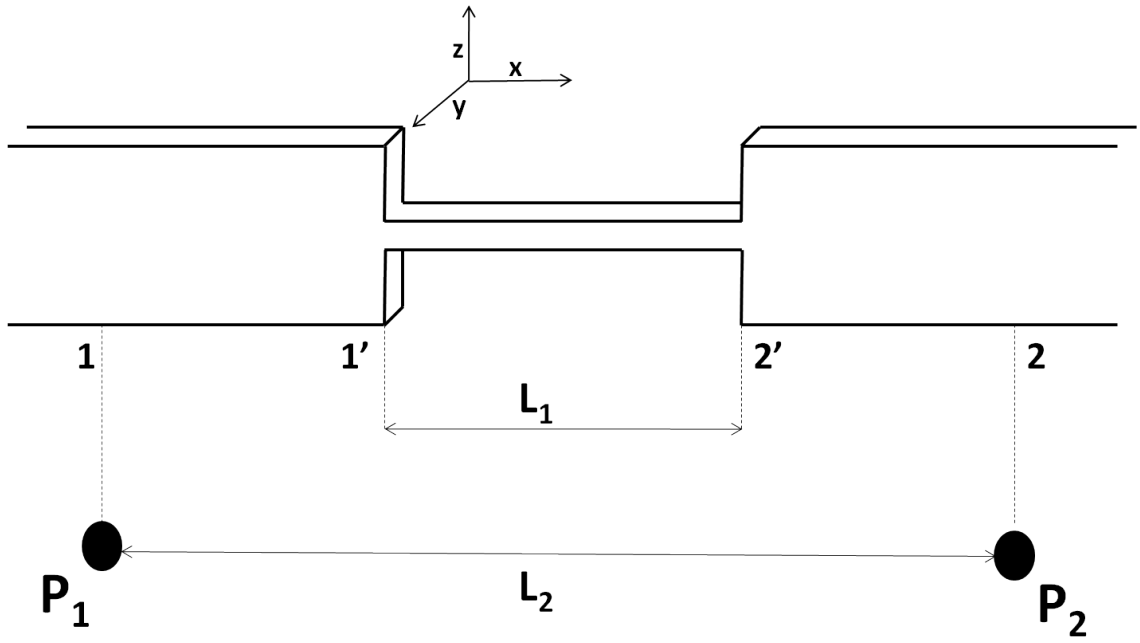

Figure 3.3: Schematic diagram of employed microfluidic contraction devices (The Flowcells 1,2 and 3). 1 and 2 are the positions of pressure taps.

	Flowcell 1	Flowcell 2	Flowcell 3
$w_u\,[\mu m]$	800	800	400
$w_c\,[\mu m]$	200	100	25
$L_1\,[mm]$		45	45
$L_2\,[mm]$	20	20	20
h $[\mu m]$	47	47	47
$D_h\,[\mu m]$	76.1	63.9	32.6
β	4 : 1 : 4	8:1:8	16:1:16
α	1/17	1/17	2/17
ε_H	1.38	2.07	2.77

Table 3.1: Geometric parameters of the Flowcells 1, 2 and 3 used in this work. Here $D_h = \frac{2w_c h}{w_c + h}$ is the hydraulic diameter of downstream channel, $\beta = \frac{w_u}{w_c}$ is the contraction ratio, $\alpha = \frac{h}{w_u}$ is the aspect ratio of upstream channel and $\varepsilon_H = \ln \frac{w_u}{w_c}$ is the Hencky strain.

3.5 Pressure measurements in microfluidics

Two pairs of pressure sensors, provided by Linkam Scientific Ltd., were used in this work. Each pair consists of two identical linear strain gauge pressure transducers encapsulated in a single unit. Each sensor measures the gauge pressure at the positions 1 and 2 respectively as indicated in Fig. 3.3, and allows a maximum measurable value of 1 bar and 10 bars for the first and second pair respectively. A schematic diagram of the microfluidic rig for pressure measurements is presented in Fig. 3.4. Before running each experiment, the microfluidic chip was completely filled up with the test fluid using the syringe pump, and then let at rest for one hour at least, to allow any residual stresses to relax. A Digitron 2089P digital manometer was also used, in order to obtain independent pressure measurements. The pressure signals were collected at 50 Hz by means of a data acquisition platform. It consists of a NI CompacDAQ 9172 chassis, an NI 9237 data acquisition modulus and a software written in LabView (National Instruments). The sensors were calibrated over their entire working range by applying a series of known pressures. Their responses are linear in their entire operative range (see Fig. 3.5a). Fig. 3.5b shows some typical baseline signals sampled for 1 second from pressure sensors. From these measurements, the minimum measurable pressures were estimated as 0.04 mbar and 0.26 mbar respectively, about 0.004% and 0.0026% of their full measurement scales. Prior to running experiments, both microchip and pressure sensors unit were completely filled up with test fluid. Before each experiment was run, pressure signals were off-set by software. The pressure measurement technique was validated under flow conditions using the Flowcell 4 described in Section 3.4, and DI water as a tested fluid.

The pressure drops corresponding to three consecutive step changes of flow rate from 0 to 2 ml/hr, as measured by the 10-bar sensors, are shown in Fig. 3.6. The measured pressure drops quickly reach a steady state. The noise observed in the steady pressure signals is small, approximately 0.004% of the full range of sensors. The pressure signals are highly reproducible, as the relative difference between the steady state pressure drops $\Delta P_{1,s}$ and $\Delta P_{2,s}$, corresponding to the first and second

run respectively, was estimated as $\delta_1 = \frac{\Delta P_{1,s} - \Delta P_{2,s}}{\Delta P_{1,s}} \cong 0.7\%$. Also, the relative difference between $\Delta P_{1,s}$ and the steady steady pressure drop $\Delta P_{3,s}$ corresponding to the third run was estimated as $\delta_2 = \frac{\Delta P_{1,s} - \Delta P_{3,s}}{\Delta P_{1,s}} \cong 2\%$.

The mean steady state pressure drops of DI water in a range of flow rates $1 \leq Q \leq 40$ ml/hr across the Flowcell 4 are presented in Fig. 3.5. For each flow rate, the mean steady state ΔP was obtained by an ensemble average of pressure drop readings over five minutes period after it reaches a steady state so that the measurement noise is minimized. As shown in Fig. 3.7, the experimental data were found to be in a very good agreement with the analytical solution of the Navier-Stokes equations for Poiseuille flows through rectangular ducts, given by White (1991):

$$\Delta P = \frac{3\eta L}{4ba^3} \frac{Q}{1 - \frac{192a}{\pi^5 b} K} \tag{3.12}$$

where η is the fluid viscosity, $a = w_c/2$, $b = h/2$ and $K = \sum_{i=1,3,5,\ldots}^{+\infty} \frac{\tanh(\frac{i\pi b}{2a})}{i^5}$.

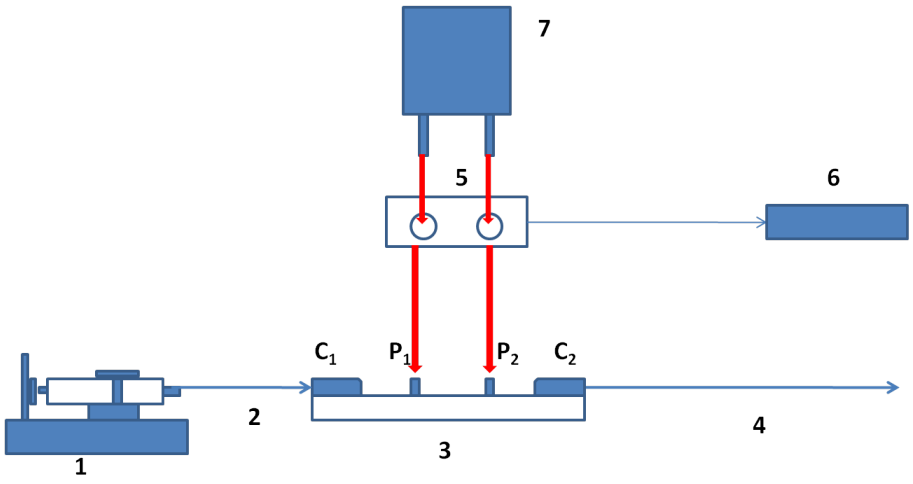

Figure 3.4: Schematic diagram of the microfluidic rig. The numbers indicate (1): the syringe pump; (2) the inlet pipe; (3) the microfluidic chip; (4) the outlet pipe; (5) the unit containing the pressure sensors; (6) the NI cDAQ data acquisition system; (7) the Digitron 2086P Digital Manometer. P_1 and P_2 are the pressure taps. C_1 and C_2 are the connectors between tubing and microchip. The connections between the pressure taps and the pressure sensor, and those between the pressure sensor and the Digitron manometer, are schematically indicated by means of red arrows.

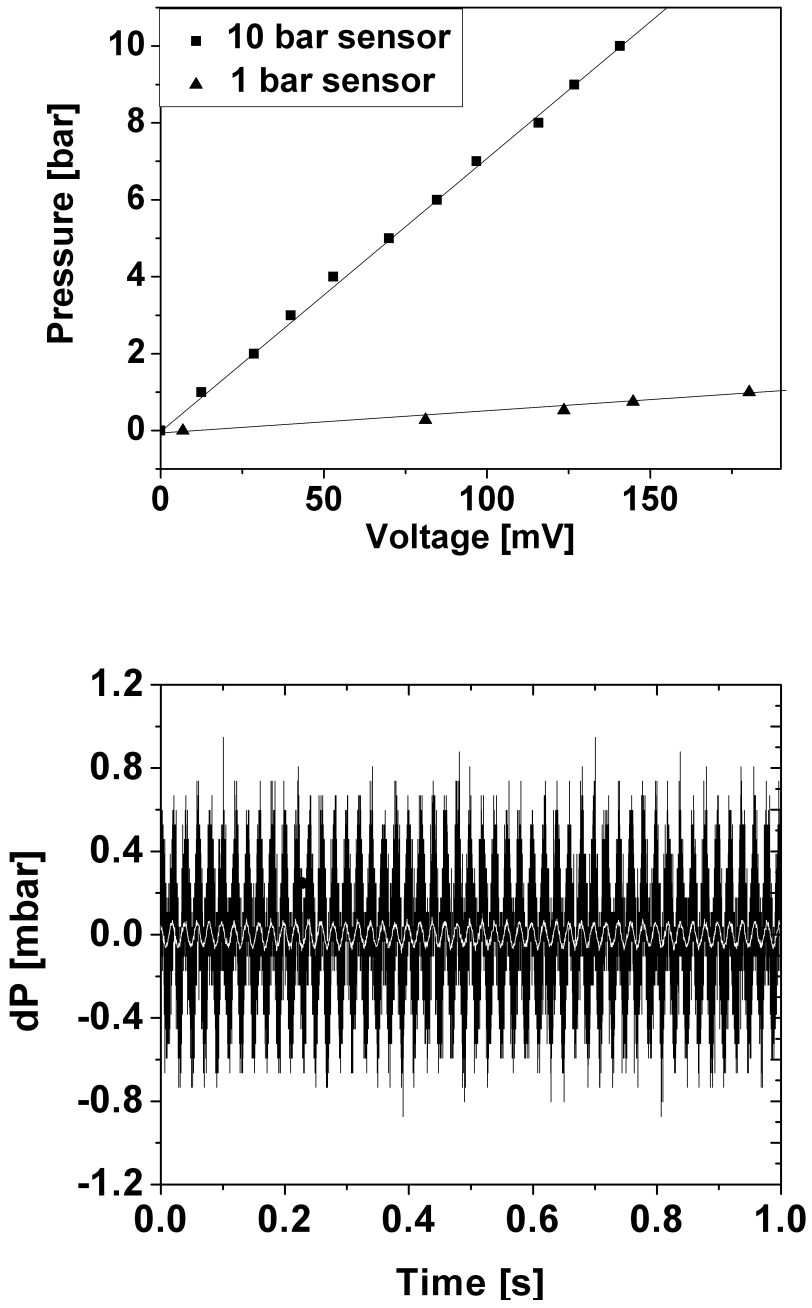

Figure 3.5: (a) Calibration curves for 1 and 10 bar sensors. (b) Pressure signals from 1 bar (white) and 10 bar (black) sensors when no pressure is imposed.

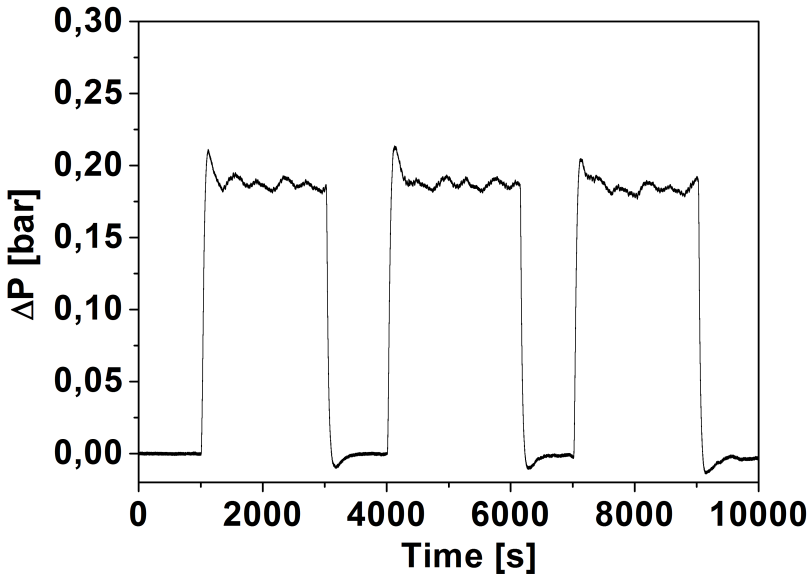

Figure 3.6: Pressure drops across the Flowcell 4 corresponding to three consecutive step-rate changes of water flow rate from 0 to 2 ml/hr, as measured by the 10 bar-range pressure sensors.

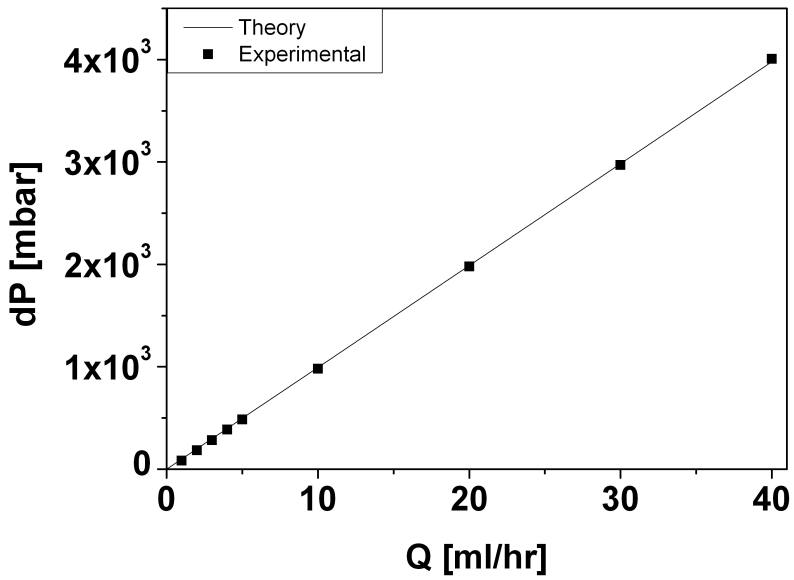

Figure 3.7: Comparison of the experimental pressure drops of water, as measured across the Flowcell 4, with the analytical prediction for Newtonian flows through rectangular ducts.

3.6 Micro-particle image velocimetry

Micro-particle image velocimetry ($\mu - PIV$) is a technique which performs quantitative measurements of a velocity field with a spatial resolution of only a few μm. It constitutes a natural extension of the traditional PIV technique, which does not allow measurements at spatial resolutions lower than $0.2\ \mathrm{m} - 1\ \mathrm{mm}$ (Wereley and Meinhart, 2005).

In PIV measurements, fluid is seeded with tracing fluorescent particles, properly chosen in order to faithfully follow the fluid flow. Fluid is then illuminated by a pulse laser with a specified time delay between consecutive pulses Δt, and images are recorded by a camera. A software then computes the particles displacement in Δt and, consequently, the velocity field. The schematic diagram of the micro-PIV system employed in this work, made by TSI Inc., is shown in Fig. 3.8. It consists of three main modules: an Nd:YAG double-pulsed laser (minimum time difference between two consecutive pulses $\Delta t_{min} \cong 10$ ns, wave length $\lambda = 532$ nm, frequency $f = 15$ Hz, power $P = 15$ mJ), a TE2000-E inverted microscope (Nikon Corp.) equipped with various lenses with magnification $M = 10X$, $20X$ and $40X$ respectively, and a SensiCam 12-bit camera (1280×1024 pixel resolution, pixel pitch $P = 12\,\mu m$). The laser beam travels by means of a light-guide from laser to the microscope, where a diffuser expands the diameter of the laser beam into 20 mm. The motion of fluids (seeded with fluorescent particles) is then illuminated, and the camera records consecutive pairs of images. A careful control of timing between pulse laser and camera is performed by a synchronizer. The position of the focusing plane can be tuned by a motorized controller, with a resolution of 0.05 microns. Acquired images are then processed by a software using a cross-correlation algorithm supplied by Insight-3G software (TSI Inc.), in order to obtain velocity vector fields (Santiago et al., 1998; Meinhart et al., 1999).

3.6.1 Spatial resolution in PIV experiments

The crucial element in micro-PIV experiments is to accurately resolve the displacements of seeding particles using the optical system. The in-plane resolution of a

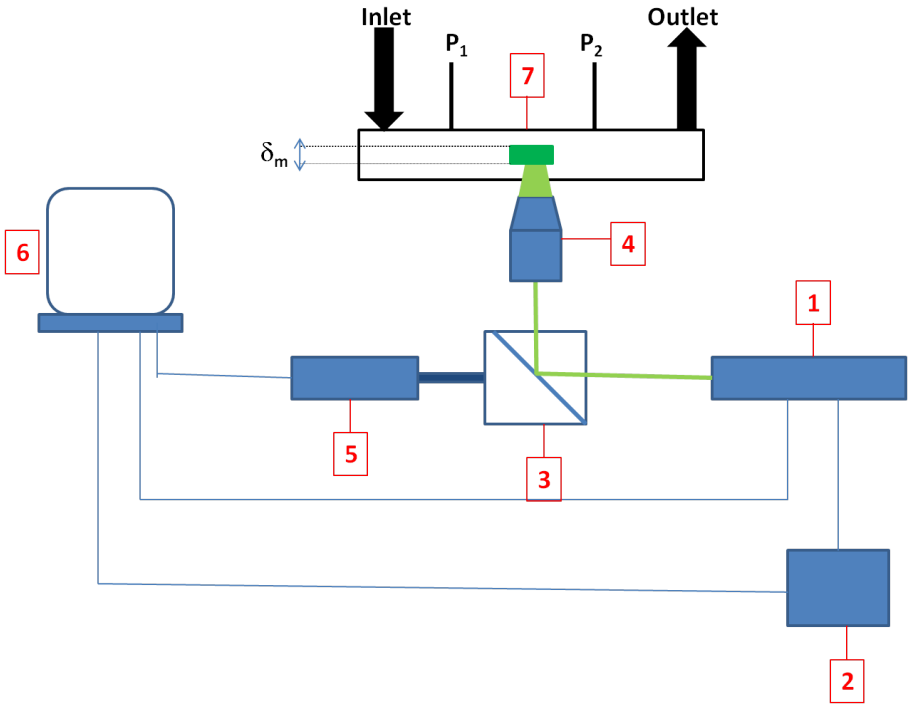

Figure 3.8: Schematic diagram of the micro-PIV system used in this work. Numbers refer to: (1): double-pulsed laser device (2): synchronizer system (3): filter cube of the TE-2000 microscope (4): magnification lens (5): CCD camera (6): control computer (7): micro-fabricated flowcell. Inlet, outlet, pressure taps P_1 and P_2 are represented. The PIV measurement depth δ_m is also indicated.

$\mu - PIV$ system is quantifiable by means of the diffraction-limited diameter of the *point-spread function*, d_s, associated to a self-luminous object as imaged by optics with a circular aperture. It can be calculated by the formula of Olsen and Adrian (2000):

$$d_s = 2.44(M+1)\frac{\lambda}{2NA} \tag{3.13}$$

where M is the magnification of lens and $NA = n\sin(\alpha/2)$ is the numerical aperture (n is the diffraction index of the medium placed between microfluidic device and optics, and α is the angular aperture of lens). If the objective lens features an infinity correction, d_s can be estimated by+ (Meinhart and Wereley, 2003):

$$d_s = 1.22M\lambda\sqrt{\left(\frac{n}{NA}\right)^2 - 1}. \tag{3.14}$$

The diameter of the particle image recorded by the CCD camera, d_e, is given by a convolution between d_s and the magnified diameter of particle itself, Md_p, which is

estimated by (Santiago et al., 1998):

$$d_e = \sqrt{d_s^2 + (M d_p)^2}. \tag{3.15}$$

The image diameter as projected back into the flow is given by $d_{pb} = \frac{d_e}{M}$. Although conventional $\mu - PIV$ technique aims at providing 2D velocity field measurements over a fixed plane, particles are in facts imaged within a finite depth. The depth of measurement in $\mu - PIV$ experiments δ_m, defined as twice the distance from the focusing plane at which a flowing particle becomes unfocused, is estimated by Meinhart et al. (2000):

$$\delta_m = \frac{3n\lambda}{NA^2} + \frac{2.16 d_p}{\tan(\alpha/2)} + d_p. \tag{3.16}$$

The values of d_e and δ_m related to the objective lenses employed in this work, labelled as Lens No. 1, 2 and 3 respectively, are given in Table 3.2.

3.6.2 Seeding particles and Brownian motion

The reliability of velocity measurements in $\mu - PIV$ is strongly dependent on the quality of the acquired particle images. In $\mu - PIV$ experiments, the entire volume of fluid is illuminated, so that all the particles within the field of view contribute to the image. The background noise resulting from unfocused particles can be reduced by means of a proper choice of the experimental conditions. The analysis of Olsen and Adrian (2000) suggests that the particle visibility Vis, defined as the ratio of the intensity of the light emitted by an in-focus particle to the intensity of the background light due to the unfocused particles, is given by:

$$Vis = \frac{4M^2\beta^2(s_0 - a)(s_0 - a + h)}{\pi c L s_0^2 (M^2 d_p^2 + 1.49(M+1)^2\lambda^2/NA^2)} \tag{3.17}$$

where c is the number of seeding particles in the unit volume of fluid, s_0 is the distance of the object plane from the lens, a is the distance of the object plane from the top of the microchannel and h is the microchannel depth.

The tested fluids were seeded with epifluorescent particles (Duke Scientific Co.) with a diameter $d_p = 1.0\,\mu m$. They are excited by the $\lambda_0 = 532$ nm laser light and emit light at wave length of $\lambda = 560$ nm. A particle concentration $c_p = 0.02$ wt.%. was employed. This resulted in a particle visibility much bigger than the unity for all the objective lenses used in this work ($7.0 \leq Vis \leq 116.7$, see Table 3.2). For a steady flow, and in regions where local velocity gradients are small, the error in velocity measurements due to Brownian motion of seeding particles, ε_B, can be estimated as (Santiago et al., 1998):

$$\varepsilon_B = \frac{1}{v}\sqrt{\frac{2D}{\Delta t}} = \frac{1}{v}\sqrt{\frac{2k_BT}{3\eta\pi d_p \Delta t}} \tag{3.18}$$

where v is the local fluid velocity and D is the diffusivity coefficient of particles, which can be expressed as $D = \frac{k_BT}{3\eta\pi d_p}$, with k_B and T being the Boltzmann constant and the fluid temperature respectively, following Einstein's derivation. Eq. 3.18 suggests that the error due to Brownian motion in $\mu - PIV$ experiments can become large if the velocity field of very low speed flow need to be measured.

In order to reduce the measurement error due to Brownian motion, Wereley et al. (2002) suggest performing an ensemble-average of instantaneous PIV velocity vector fields over a certain number of consecutive captures. In this work, instantaneous velocity fields were averaged over 50 consecutive captures just in cases where the flow field appeared to be time-independent.

Lens	M	NA	Technique	d_e $[\mu m]$	d_{pb} $[\mu m]$	δ_m $[\mu m]$	working distance [mm]	Vis	Spatial resolution with 50% overlap $[\mu m]$
No. 1	10X	0.3	Single lens	23.8	2.38	18.81	16	7.0	28.8
No. 2	20X	0.45	Infinity corrected	25.8	1.29	9.06	7 - 8.1	78.9	14.4
No. 3	40X	0.6	Infinity corrected	34.6	0.86	5.8	2.7-3.7	116.7	7.2

Table 3.2: Specifications of the $\mu - PIV$ microscope objective lenses in this work.

3.6.3 Image processing

The Insight 3G software implements a cross-correlation algorithm to each pair of acquired images to produce the velocity fields. It divides each pair of images in a number k of small sub regions, commonly called interrogation areas, with a size of

$p \times q$ pixels. For each interrogation area IA_k, a discrete cross-correlation function Φ_k between the distributions of gray values in the first and second image is calculated:

$$\Phi_k(m,n) = \sum_{i=1}^{p} \sum_{j=1}^{q} f_k(p,q) g_k(p+m, q+n) \tag{3.19}$$

where (m,n) is a position along IA_k, and f_k and g_k are the gray value distributions along IA_k for the first and second image respectively. The position along IA_k of the maximum of $\Phi_k(m,n)$ provides an indication of the particles displacement within IA_k. Insight 3G estimates the cross-correlation function by a Fast Fourier Transform-based algorithm. In this work, it was chosen to systematically divide the image pairs in interrogation areas of 48×48 pixels, with a 50% overlap.

The linear size of each interrogation cell as projected back into the flow are shown in Table 3.2. Each IA contains $3-4$ particles approximately, which resulted in adequately high values of correlation peaks for a large range of imposed Δt.

3.6.4 PIV measurements of water in microfluidics

Prior to perform velocity measurements of complex fluids in microfluidics, the micro-PIV technique has been tested by measuring the flow field of DI water. These experiments are useful to validate the experimental technique and the velocity measurement methods through comparison of the experimental results with the theoretical results of Newtonian fluid (water) flow. Hence the quality of seeding particles tracking the flow, and the overall performance of the optical setting up and the data analysis method can be assessed.

Fig. 3.9 shows ensemble-averaged velocity fields of the flow of DI water through the Flowcell 3 described in Section 3.4, at two different flow rates ($Q = 0.4$ and 1 ml/hr respectively). Each velocity field was obtained by performing an ensemble-average over 50 consecutive velocity fields measured at the $y = 0$ plane, after the pressure drop has reached the steady state. Fig. 3.10 shows the axial velocity components v_x, extracted from the velocity fields in Fig. 3.9a and Fig. 3.9b along the $z = 0$ line, normalized by the average velocity $< v >$ and plotted as a function of x/w_c. These

velocity profiles show that the entry flow of Newtonian fluid starts at $x/w_c \cong -10$.

Fig. 3.11a and Fig. 3.11b show the v_x component of the velocity field plotted as a function of both y/w_c and z/h, measured for the Flowcell 2 and Flowcell 3 and at a position $x/w_c << -1$, where the flow is fully developed, at flow rates $Q = 2$ and $Q = 1$ ml/hr respectively. Images were acquired using the No. 1 and No. 2 lenses for the Flowcell 2 and 3 respectively. Velocity values at a given y/h coordinate were obtained in the following way: the focus of microscope was fixed at a given vertical position, an ensemble-averaged velocity field was produced (following the same procedure as for the velocity fields previously described), and an average of v_x values at a given x and for $-0.2 < z/w_c < 0.2$ (thus in a zone where the v_x vs z profile is constant) was taken. Velocity measurements on both the z and y directions are compared with the analytical prediction for Newtonian flows through rectangular ducts reported by White (1991):

$$v(y,z) = \frac{12Q}{ab\pi^3} \frac{\sum_{i=1,3,5,\ldots}^{\infty} \cos\frac{i\pi y}{2a}\left(1 - \frac{\cosh(\frac{i\pi z}{2a})}{\cosh(\frac{i\pi b}{2a})}\right)}{1 - \frac{192a}{\pi^5 b}K} \tag{3.20}$$

where a,b and K have the same meaning as in Section 3.5. Measured velocity values appeared to be lower than the analytical predictions. The errors were estimated as $\varepsilon \cong 17\%$ for the flow measurements with a magnification $M = 10X$ through the Flowcell 2, and $\varepsilon \cong 10\%$ for the flow measurements with $M = 20X$ through the Flowcell 3. Note that under the experimental conditions ($\Delta t = 80$ and $30\,\mu s$ in Flowcells 2 and 3 respectively) the errors due to Brownian motion are estimated as $\varepsilon_{B,Flowcell2} = 0.7\%$ and $\varepsilon_{B,Flowcell3} = 1.1\%$, following Eq. 3.18. The error in PIV experiments could be a consequence of the relatively large measurement depth of the optics, as δ_m resulted to be 19.3% and 40.0% of the full channel depth ($h = 47\mu m$) for the measurements taken at $M = 20X$ and $M = 10X$ respectively. A high speed confocal microscopy technique (Kinoshita et al., 2006b,a) can considerably reduce such a measurement error, but it is not cost-effective for the present study.

The $\mu - PIV$ experiments with polymer solutions presented in the following pages were performed with the No.1 lens (thus $\delta_m = 18.8\,\mu m$) for the No. 1 and No.2 Flowcells, with the No.2 lens (thus $\delta_m = 9.06\,\mu m$) for the No.3 Flowcell, and

with the No. 3 lens (thus $\delta_m = 5.8\,\mu m$) for the No.4 Flowcell. As long as there is no slipping between seeding particles and test fluid, which is true for all polymer solutions studied here, the uncertainties of the $\mu - PIV$ measurements in polymer solutions are essentially the same as those observed for Newtonian flow.

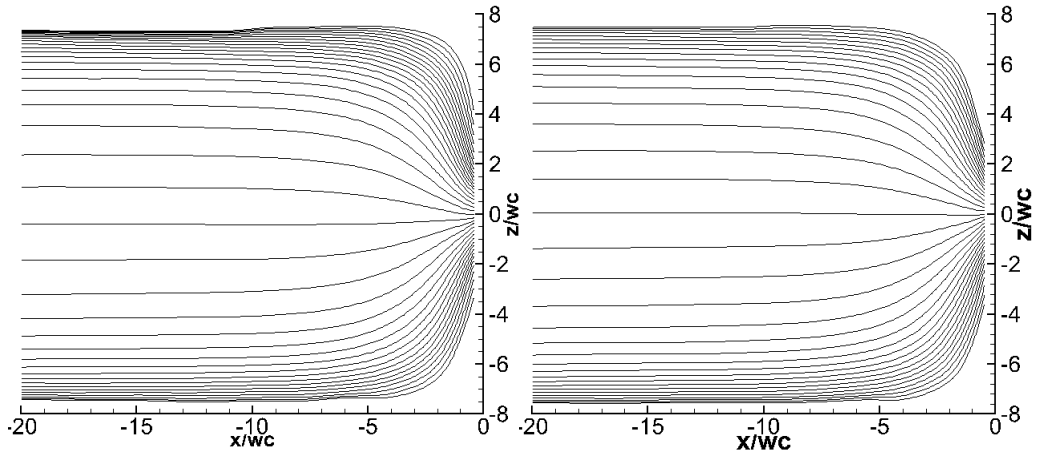

Figure 3.9: Time-averaged, PIV-generated centreplane velocity fields for the flow of water through the Flowcell 3 described in Section 3.4 at flow rates $Q = 0.4$ ml/hr (a) and $Q = 1$ ml/hr (b).

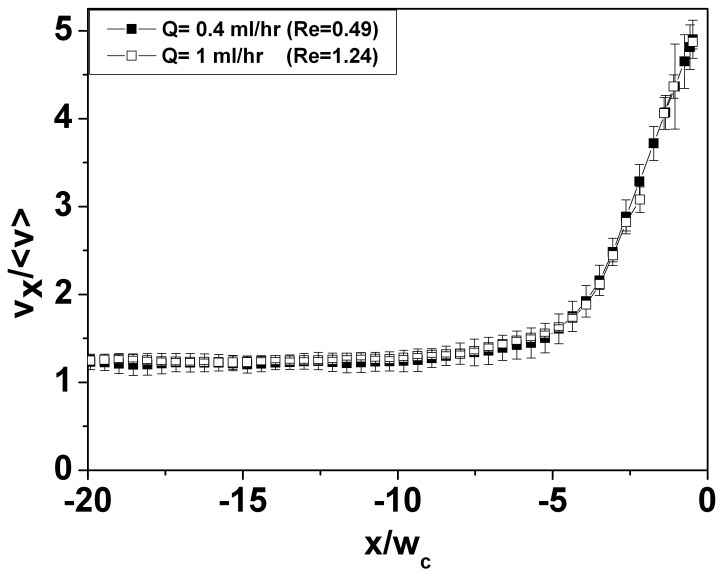

Figure 3.10: PIV-generated, time-averaged v_x components of the velocity profiles of water plotted as a function of x/w_c and at $y = 0$, at two imposed flow rates ($Q = 0.4$ and $Q = 1$ ml/hr respectively), for the Flowcell 3 described in Section 3.4.

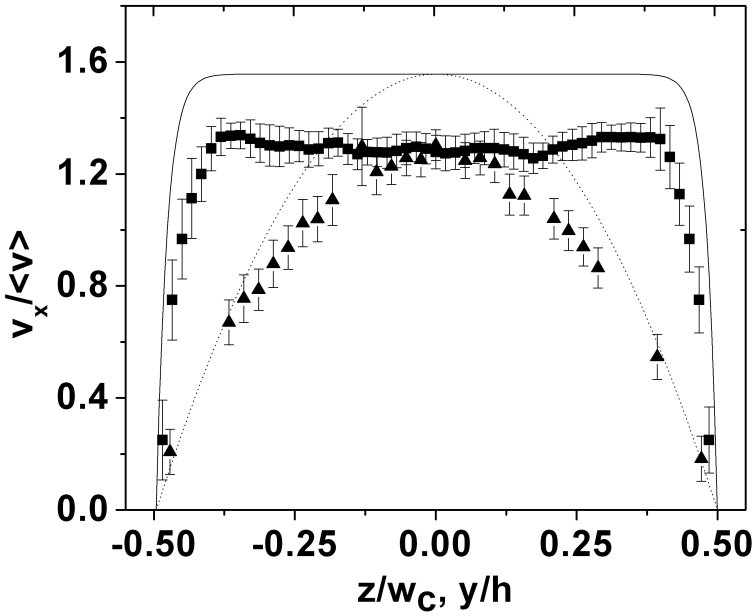

(a)

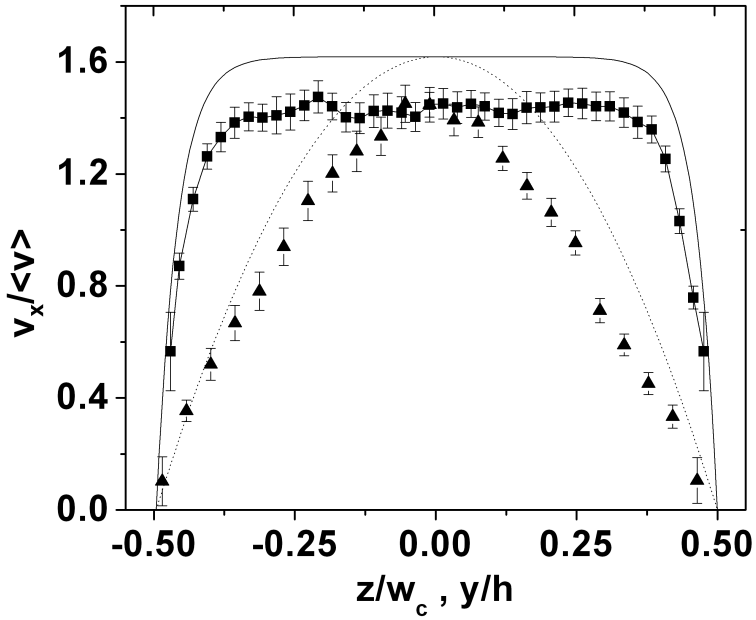

(b)

Figure 3.11: Comparison of the v_x components of PIV-generated, time-averaged velocity profiles of water, plotted along both y and z directions, with the analytical prediction of Poiseuille flow for Newtonian fluids through rectangular ducts for the Flowcell 2 (a) and the Flowcell 3 (b). Symbols and lines refer to: (*squares*) $\frac{v_x}{<v>}$ vs z/w_c experimental; (*triangles*) $\frac{v_x}{<v>}$ vs y/w_c experimental; (*continuous lines*) analytical prediction of $\frac{v_x}{<v>}$ vs z/w_c; (*dashed lines*) analytical prediction of $\frac{v_x}{<v>}$ vs y/w_c.

Chapter 4

Molecular and rheometric characterization of model fluids

4.1 Introduction

This Chapter presents the results of the molecular analysis of the polyacrylamide sample, and the rheometric characterisation of PAAm aqueous solutions. It is organized as follows. Section 3.2 reports the Gel Permeation Chromatography (GPC) analysis of the PAAm. Section 4.3 presents the viscous and the elastic modulus of a model solution, as measured under small amplitude oscillatory shear flow. A combined use of Vilastic-3 and PAV rheometers allowed for obtaining the relaxation spectrum across a wide range of frequencies ($4 \leq \omega \leq 4 \cdot 10^4$ rad/s). The shear viscosities measured by both ARES rheometer and the straight microchannel geometry described in Section 3.4 over a broad range of nominal shear rates ($0.1 \leq \dot{\gamma} \leq 4 \cdot 10^4\, s^{-1}$) are presented in Section 4.4. The results obtained from capillary-force-driven flows of PAAms using CaBER rheometer are presented in Section 4.5.

4.2 Molecular characterisation

The molecular weight distribution of PAAm sample, characterized by means of the GPC system described in Section 3.2, is shown in Fig. 4.1. Molecular moments

are shown in Table 4.1 and compared with the characteristics of the polyethylene oxide (PEO) sample used in the work of Li et al. (2011), which investigates the flow of PEO aqueous solutions through an 8:1 contraction geometry almost identical to the Flowcell 2 presented here (see Table 3.1). The PAAm material used in this work features a larger molecular weight and a much broader polydispersity index. Differences in molecular characteristics of polymers result in differences in flow behaviour in microfluidics.

The mean radius of gyration of PAAm molecules in water was calculated by the formula $R_g = 0.0749 * M_w^{0.64 \pm 0.01}\, \mathring{A}$ proposed by François et al. (1980), from which overlap concentration was calculated by $c^* = \frac{M_w}{N_a (2R_g)^3}$, following a simple cubic packing approximation. The original 1 wt.% (5M) PAAm aqueous solution from Polysciences Europe GmbH was subsequently diluted with DI water, in order to obtain three solutions with PAAm concentrations of 0.1 wt.%, 0.25 wt.% and 0.5 wt.%, ranging from $3.3c^*$ to $16.6c^*$ respectively.

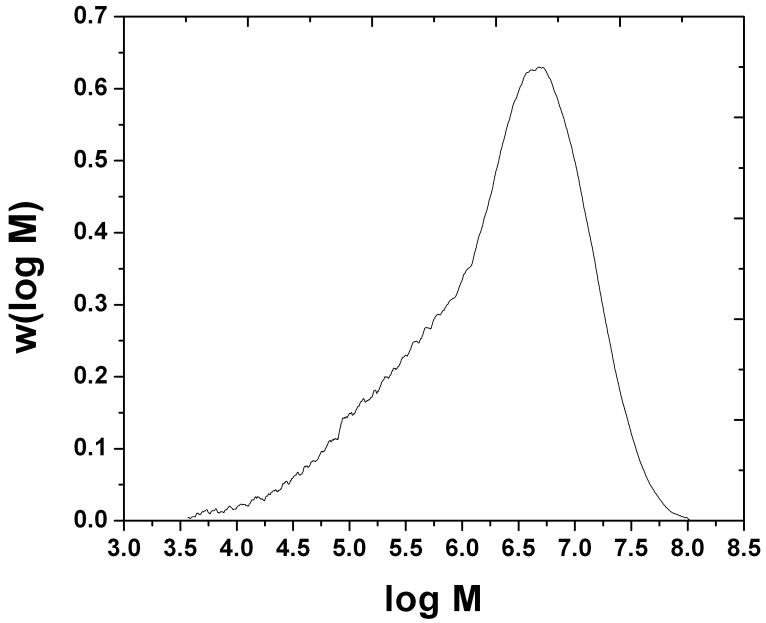

Figure 4.1: Molecular weight distribution of polyacrylamide sample.

Material	$10^{-6} \cdot M_n$	$10^{-6} \cdot M_w$	$10^{-6} \cdot M_z$	M_w/M_n	M_z/M_w	R_g [Å]	c^* [$wt.\%$]
PAAm	0.16	5.7	17.9	34.4	3.15	1578	0.031
PEO	6.4	4.82	14.1	7.5	2.90	1690	0.0206

Table 4.1: Molecular characteristics of polyacrylamide sample. The molecular moments of the PEO sample used in Li et al. (2011) are shown for a comparison.

4.3 Linear viscoelasticity

The linear viscoelasticity region of the $16.6c^*$ PAAm solution was determined by dynamic strain-sweep tests conducted at 1 Hz with both ARES and Vilastic-3 rheometers (see Section 3.3.1 and Section 3.3.2). As shown in Fig. 4.2, the fluid response becomes non-linear at a strain $\gamma \geq 30\%$. Storage and loss moduli of the $16.6c^*$ PAAm solution as a function of frequency are presented in Fig. 4.3. For low and medium frequencies ($2 \leq \omega \leq 100$ rad/s), measurements were carried out by means of Vilastic-3 with an imposed strain $\gamma = 30\%$. In the high frequency range ($100 \leq \omega \leq 6 \cdot 10^3$ rad/s), which is inaccessible to ARES and Vilastic-3 due to onset of inertial effects, it was necessary to use the piezoelastic axial vibrator (PAV) described in Section 3.3.3. IRIS software (IRIS Development, USA) was used to obtain the relaxation spectrum. It fits the experimental G',G" data by the multi-mode Maxwell model:

$$G'(\omega) = \sum_{i=1}^{N} G_i \frac{(\omega\lambda_i)^2}{1 + (\omega\lambda_i)^2} \tag{4.1}$$

$$G''(\omega) = \sum_{i=1}^{N} G_i \frac{\omega\lambda_i}{1 + (\omega\lambda_i)^2} \tag{4.2}$$

The G_i, λ_i values are found by minimization of the average square deviation between the fitted and the measured viscous and elastic moduli (Baumgaertel and Winter, 1989). The 5-modes relaxation spectrum is shown in Table 4.2.

4.4 Shear flow

The steady shear viscosities of the materials used in present work were characterized by means of the ARES rheometer equipped with a double-wall Couette tool

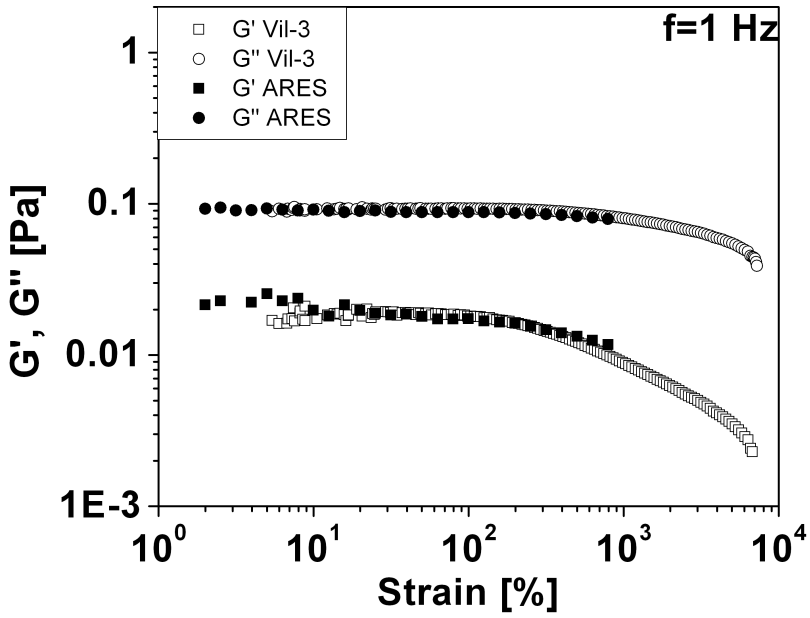

Figure 4.2: strain sweep of the 16.6c^* PAAm solution performed at $f = 1$ Hz.

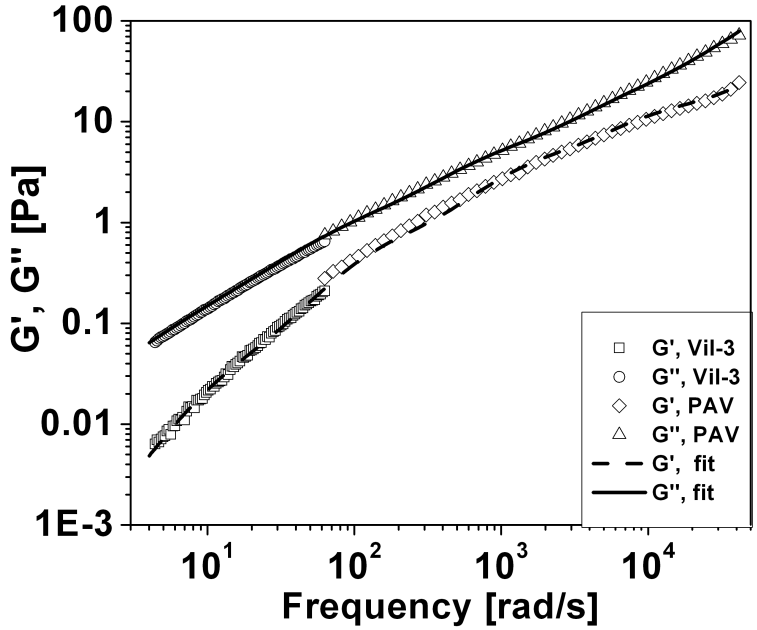

Figure 4.3: G' and G'' of the 16.6c^* PAAm aqueous solution as a function of frequency.

described in Section 3.3.1, in a range of low and medium shear rates ($0.2 \leq \dot{\gamma} \leq 1200\, s^{-1}$). The onset of Taylor-Couette instabilities constitutes an upper limit for the measurements of the PAAm solutions performed in this geometry, and can be quantified by means of the equation $\eta_{crit} = 3.43 * 10^{-6}\dot{\gamma}_{crit}$ (see Section 3.3), which

Mode i	G_i [Pa]	λ_i [ms]	$\eta_i = G_i\lambda_i$ [mPa*s]
1	689.7	0.0027	1.86
2	10.26	0.1128	1.16
3	3.894	0.9695	3.78
4	0.6733	9.232	6.22
5	0.03802	83.93	3.19
Solvent	-	-	1
Total			**17.2**

Table 4.2: The relaxation spectrum of the $16.6c^*$ aqueous PAAm solution.

is represented as a dashed line in Fig. 4.5. The viscosity in very high shear rate flow was characterized by means of the Flowcell 4 described in Section 3.4. A range of flow rates, 0.2 ml/hr $\leq Q \leq$ 28 ml/hr, was imposed, corresponding to shear rates $270\,s^{-1} \leq \dot{\gamma} \leq 38000\,s^{-1}$. Mean steady pressure drops of polymer solutions and water are plotted in Fig. 4.4. Their viscosities can be related to measured steady pressure drops by means of a Poiseuille-like equation:

$$\eta = f\frac{\Delta P D_h^4}{QL} \tag{4.3}$$

where f is a geometric constant of the microchannel in use, and is determined by fitting measured pressure drops of water (for which the viscosity is known, e.g. $\eta = 1$ mPa $\cdot$ s at $T = 20°$ C) with Eq. 4.3. We estimated $f = 1.028$ for the used microchip. The shear viscosities as measured with both ARES and microfluidic rheometers are then plotted in Fig. 4.5 as a function of the nominal shear rate, which is defined by $\dot{\gamma} = \frac{2Q}{hw_c}$ for the microchannel geometry. There are excellent agreements between these two techniques. The $3.3c^*$ and $8.3c^*$ solutions appear to be very weakly shear thinning in the range of Wi measured. A more pronounced shear thinning is observed for the $16.6c^*$ PAAm solution. Fig. 4.5 also shows the complex viscosity modulus $|\eta^*| = \frac{\sqrt{G'^2+G''^2}}{\omega}$ of the $16.6c^*$ PAAm solution, deduced from the linear viscoelasticity measurements in Fig. 4.3 and plotted as a function of the angular frequency ω. $|\eta^*|$ overlaps with the steady shear viscosity η at low and medium shear rates, and becomes lower than η for $\dot{\gamma} \geq 10^2\,s^{-1}$. The $16.6c^*$ PAAm solution does not follow the empirical Cox-Merz rule (for which $|\eta^*(\omega)| = \eta(\dot{\gamma})$ at

$\dot{\gamma} = \omega$, see Larson (2001)). Note that Kulicke and Porter (1980) reported that the Cox-Merz rule is not valid for 5 wt. % polyacrylamide solutions with nearly the same average molecular weight of polymer as in the present work. Such discrepancy between dynamic and steady shear viscosities has also been reported for associative polymers (Pellens et al., 2004).

Note that the novel microfluidic technique presented here can measure steady shear viscosity of the PAAm solutions, with the minimum inertial effects and sample volume, in shear rates at least two order of magnitude higher than what can be reliably obtained from most commercial rheometers. It is of great interest to industrial applications such as inkjet printing and enhanced oil recovery in porous media.

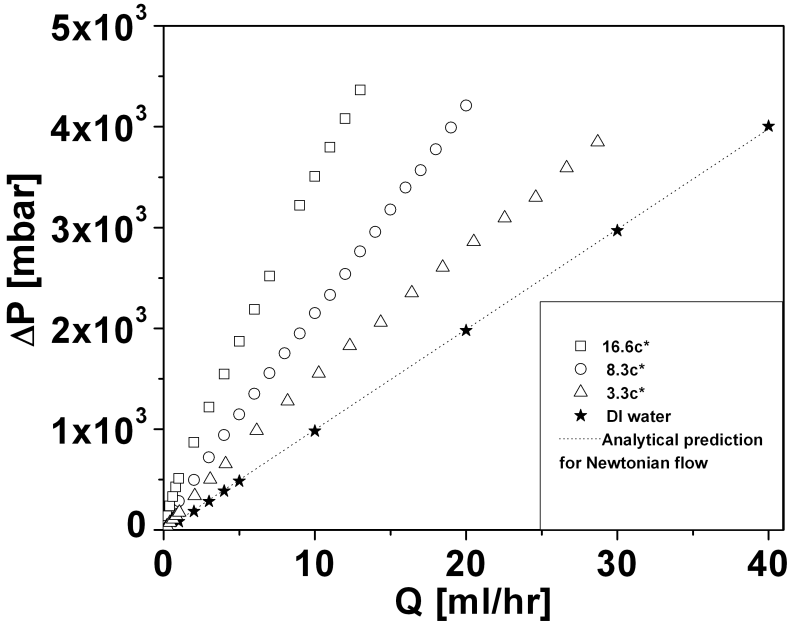

Figure 4.4: Pressure drops of PAAm solutions and of DI water through a straight microchannel as a function of the volumetric flow rate Q.

4.5 Capillary break-up extensional rheometry

A relaxation time of the polymer solutions was also measured using CaBER. These measurements were performed using plates with a radius $R_0 = 2$ mm, an initial gap height between the plates $h_0 = 2$ mm and a final gap height $h_f = 7.55$ mm. The plates were smaller than those used elsewhere (Rodd et al., 2005b,a, 2007) to ensure

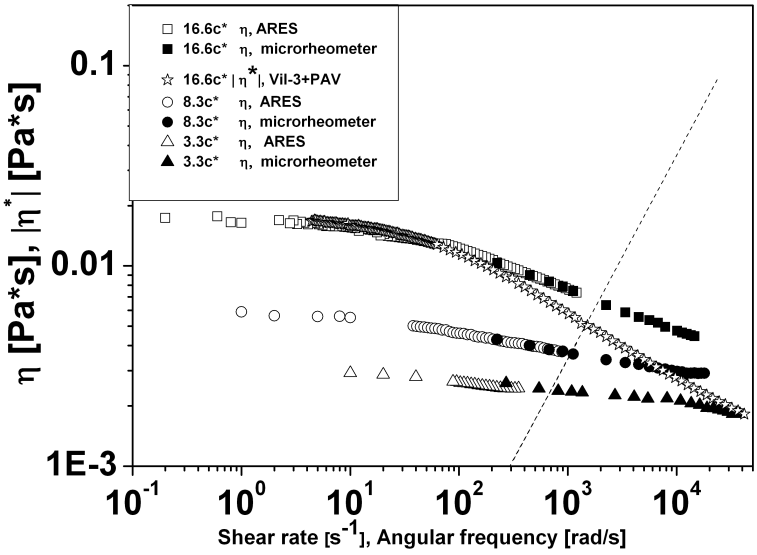

Figure 4.5: Shear viscosities as a function of the shear rate for the studied polymer solutions, as measured with ARES rheometer and the microfluidic device, and the complex viscosity modulus as a function of angular frequency for the $16.6c^*$ PAAm solution. Shear rates in microscopic flow are defined similarly as in Table 5.1.

the filament thinning flow with a relatively large Ohnesorge number $Oh = \frac{\eta_0}{\sqrt{\rho\sigma R_0}}$, and hence minimize the inertial noises in CaBER measurements (see Section 3.3.4). Characteristic Oh values are given in Table 4.3. The chosen value of the initial gap allows for Bond numbers smaller than unity for each fluid (see Table 4.3), so that the initial fluid column is nearly cylindrical.

The images of the progressive capillary-force-driven filament failure of the $16.6c^*$ PAAm solution, captured by an high speed camera, are shown in Fig. 4.6: (a) immediately after the end of pre-stretching, (b)-(d) the formation of a thin, axially *uniform* filament and (e) eventually pinching off after approximately 0.07 s. This could be due to the relatively large Elastocapillary numbers in the CaBER experiments, $19 \leq Ec \leq 31$ (see Table 4.3). The midfilament diameter is plotted as a function of time for the three PAAm solutions in Fig. 4.7. It decays in a nearly exponential fashion. There is no viscous thinning regime in the curves. Moreover, the slope of curves and the breakup times are increased as the PAAm's concentration is increased. The longest relaxation times were extracted by fitting the curves with the model proposed by Anna and McKinley (Anna and McKinley, 2001). The

results are between 2.55 and 9.95 ms (see Table 4.3). Note that the relaxation time extracted from the CaBER measurement is within the characteristic time range of the relaxation spectrum obtained from the small amplitude oscillatory shear experiments (see Table 4.2).

In Fig. 4.8, the ratios between the CaBER determined relaxation time and the Zimm relaxation time $\lambda_{CaBER}/\lambda_{Zimm}$ are plotted as a function of c/c^*. The $\lambda_{CaBER}/\lambda_{Zimm}$ ratios for aqueous solutions of a $M_w = 18*10^6$ g/mol PAAm sample from Huang (2010) are also shown. The data appear to follow a same curve. A linear fitting gives a slope $m \cong 1$, much higher than the predicted value $m_{theory} = \frac{2-3\nu}{3\nu-1} = 0.086$ derived from the equilibrium scaling theories (see Section 2.2.1). This could be due to the highly non-equilibrium state of the polymer chains experienced in capillary-force-driven experiments, and to the high polydispersity of the PAAm samples used here.

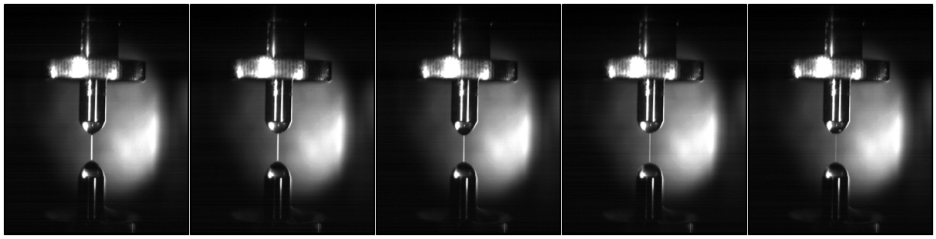

(a) $t = 0$ s (b) $t = 0.017$ s (c) $t = 0.034$ s (d) $t = 0.053$ s (e) $t = 0.07$ s

Figure 4.6: Capillary-force-driven thinning of a 0.25 wt.% PAAm solution as a function of time.

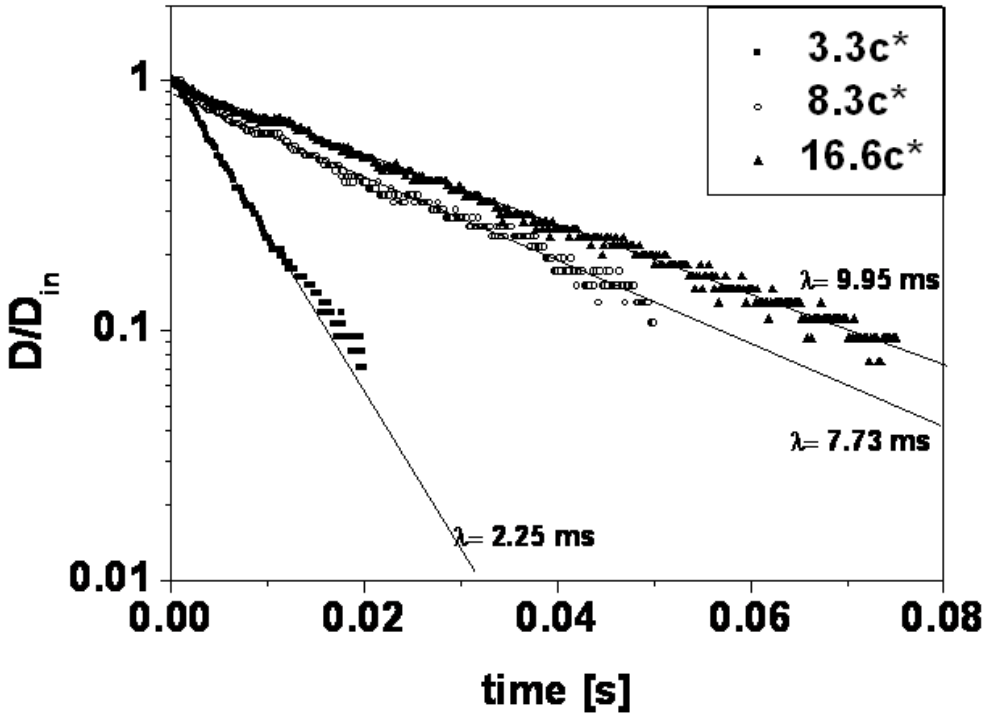

Figure 4.7: Midfilament diameter decay as function of time for three PAAm solutions.

Fluid property	0.1% PAAm	0.25% PAAm	0.5% PAAm
η_0 $[Pa \cdot s]$	0.0024	0.0061	0.0174
λ_{CaBER} [ms]	2.25	7.73	9.95
$\lambda_{CaBER}/\lambda_{Zimm}$	1.8	6.3	8.1
ρ [g/cm^3]	0.998	0.994	0.89
c/c^*	3.3	8.3	16.6
σ [mN/m]	66.1	65.1	60.5
Bo	0.592	0.599	0.577
Oh	0.0066	0.017	0.053
Ec	18.8	39.9	31.0

Table 4.3: Fluid properties and CaBER flow parameters of PAAm solutions. Zimm relaxation time was estimated as 1.277 ms following the formula proposed by Tirtaatmadja et al. (2006). *Bo*, *Oh* and *Ec* are the Bond, Ohnesorge and Elastocapillary numbers defined for CaBER experiments with the experimental conditions described in Section 4.5. The surface tension σ was measured by a CIR100 Interfacial Rheometer (Camtel Ltd).

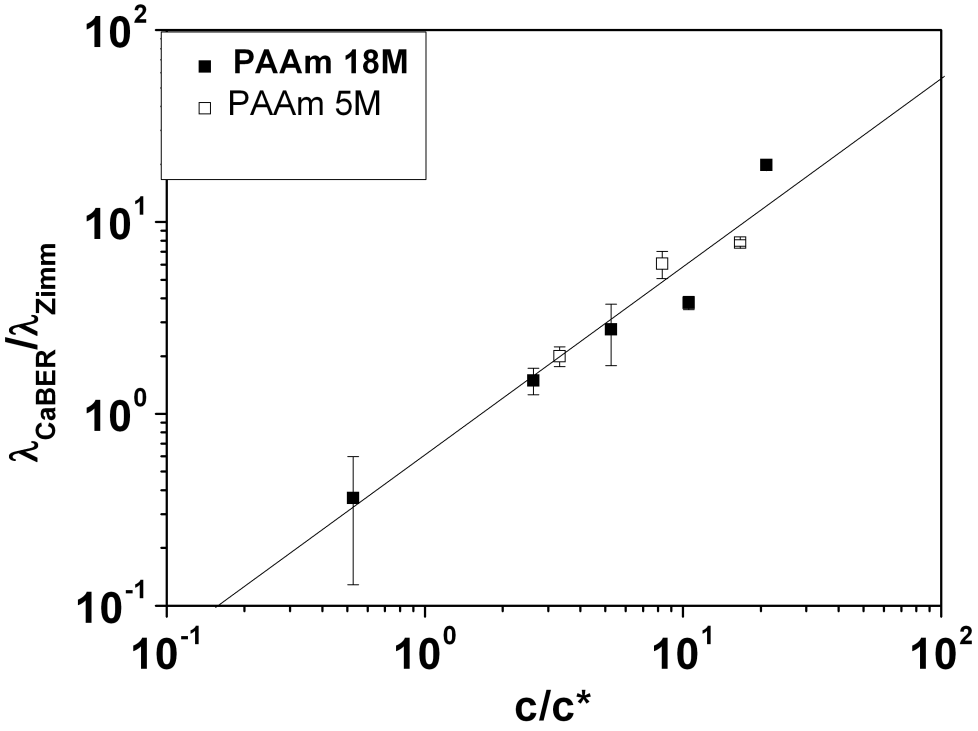

Figure 4.8: The effect of polymer concentration on $\lambda_{CaBER}/\lambda_{Zimm}$ for several semi-dilute PAAm solutions. The data labeled as "PAAm 5M" are from the present work. The data labeled as "PAAm 18M" are from Huang (2010) The straight line is the fitting with a slope $m = 1 \pm 0.11$.

Chapter 5

Flow characterization of PAAm aqueous solutions in microfluidics

5.1 Introduction

This Chapter presents the results of quantitative flow characterisation of the model PAAm solutions through the micro-fabricated geometries introduced in Chapter 3.

Following the convention broadly adopted in the literature (see for exemple (Rodd et al., 2005a, 2007)), the nominal Reynolds number Re, Weissenberg number Wi and Elasticity number El are defined as:

$$Re = \frac{\rho \langle v_c \rangle D_h}{\eta_0} = \frac{2\rho Q}{\eta_0(h + w_c)} \tag{5.1}$$

$$Wi = \lambda \dot{\gamma}_c = \frac{2\lambda \langle v_c \rangle}{w_c} \tag{5.2}$$

$$El = \frac{Wi}{Re} = \frac{\lambda \eta_0 (w_c + h)}{\rho w_c^2 h} \tag{5.3}$$

where Q is the flow rate; η_0, λ and ρ are the zero-shear viscosity, the CaBER-measured relaxation time and the density respectively; h and w_c have a same meaning as in Section 3.4; $D_h = \frac{2hw_c}{h+w_c}$ is the hydraulic diameter of downstream channel and $\dot{\gamma}_c = \frac{2\langle v_c \rangle}{w_c}$, with $\langle v_c \rangle$ being an average velocity, is the nominal shear rate in the downstream channel. A range of $\dot{\gamma}$, Wi, Re and El flows to be performed in each contraction geometry are listed in Table 5.1. By tuning both the polymer concen-

tration (thus the rheometric properties of fluid), and the geometry of microchannels, it was possible to study a wide range of Weissenberg ($1.4 \leq Wi \leq 131.7$) and Elasticity numbers ($13.3 \leq El \leq 476.8$) flows, and different vortex growth mechanisms in the upstream contraction were identified.

This approach is motivated by the fact that, as suggested in Section 2.4, mapping the rich flow phenomena on a *Wi-Re* space defined by a single characteristic length scale of flow geometry (usually the width of the downstream narrow channel) is not sufficient in general. For a general 3-D contraction flow geometry with a uniform depth, the contraction ratio β and the upstream channel aspect ratio α need to be specified. A full quantitative investigation of the flow of well-characterised polymer solutions through different micro-fabricated geometries is thus a necessary step to close the existing knowledge gap between molecular dynamics and the highly nonlinear flow behaviour in microfluidics.

The Chapter is organized as follows. Section 5.2 discusses the effect of the Weissenberg number on the middleplane velocity profiles of a $8.3c^*$ PAAm solution through the No.4 Flowcell introduced in Section 3.4. Section 5.3 presents a $\beta - Wi$ diagram which summarizes the observed flow patterns at low Elasticity number flows ($14.8 \leq El \leq 25.5$). In Section 5.4, 5.5 and 5.6, the flow characterisation by $\mu - PIV$ of the PAAm solutions through the Flowcell 1, 2 and 3 respectively are presented. The effects of both Wi and El are discussed in detail. Section 5.7 discusses the effect of Weissenberg number on the centreline velocity profiles and elongational rates for the $El = 25.5$ and $El = 14.8$ flows through the 4:1:4 and 8:1:8 geometries respectively. Section 5.8 discusses the effect of increasing Wi on the size of vortex structures for all the El flows discussed here. The excess pressure drops measured across the contraction, and their correlation with the observed vortex structures, are reported in Section 5.9.

5.2 Poiseuille flow

The centreplane, ensemble-averaged velocity profiles of the $8.3c^*$ PAAm solution through the No.4 Flowcell (straight microchannel) described in Section 3.4 are shown

		3.3c^* PAAm	8.3c^* PAAm	16.6c^* PAAm
Flowcell 1	$\dot{\gamma}\,[s^{-1}]$	\	\	$591 - 10343$
	Re	\	\	$0.05 - 4.02$
	Wi	\	\	$1.4 - 102.9$
	El	\	\	25.5
Flowcell 2	$\dot{\gamma}\,[s^{-1}]$	\	$591 - 15366$	$591 - 13002$
	Re	\	$0.31 - 6.8$	$0.1 - 2.12$
	Wi	\	$4.5 - 100.5$	$5.9 - 129.4$
	El	\	14.8	60.8
Flowcell 3	$\dot{\gamma}\,[s^{-1}]$	$473 - 52955$	\	$945 - 13239$
	Re	$0.08 - 8.95$	\	$0.02 - 0.27$
	Wi	$1.06 - 119.1$	\	$9.4 - 131.7$
	El	13.3	\	476.8

Table 5.1: Nominal shear rates and flow dimensionless numbers for the three studied PAAm solutions in the used flowcells.

in Fig. 5.1, over a range of Weissenberg numbers $52.3 \leq Wi \leq 261$. The images were captured in the middle of the 25 mm long channel, far away from the inlet and the outlet regions. The data were then normalized by the maximum velocity measured at the $z = 0$ position. The velocity profiles show a nearly parabolic shape, and overlap in the range of Wi flows. There is little shear-thinning feature in the velocity profile as the flow rates are nearly in the second Newtonian plateau of the nonlinear shear viscosity flow curve shown in Fig. 4.5.

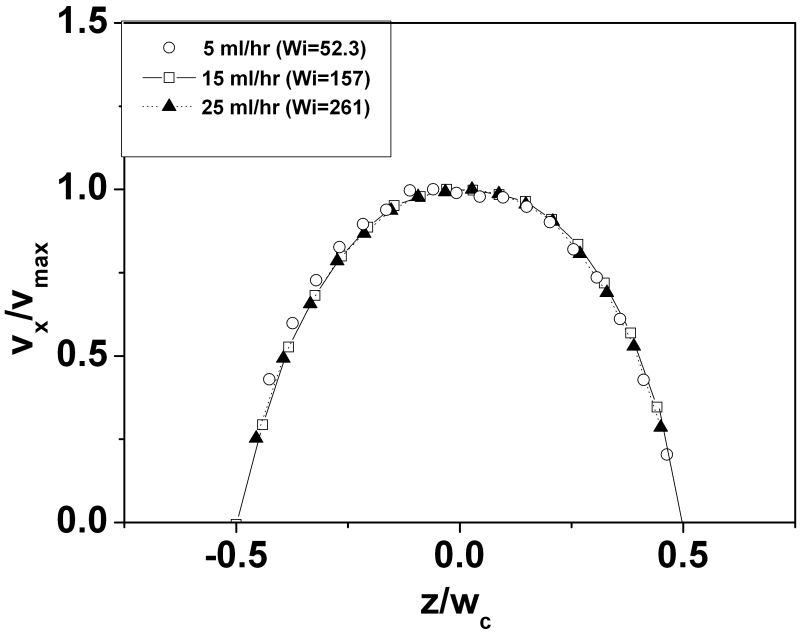

Figure 5.1: Velocity profiles for the 8.3c^* PAAm solution through a rectangular microchannel (No.4 Flowcell) over a range $52.3 \leq Wi \leq 261$.

5.3 Summary of flow regimes in a $\beta - Wi$ diagram

The overall flow patterns as a function of Wi are summarized in Fig. (5.2) for the three contraction flows at low El ($El = 25.5$, 14.8 and 13.3). The diagram is divided into three main regions, which are classified as Newtonian-like flow, lip vortex flow and corner vortex flow respectively. For each contraction ratio β, the first onset of viscoelastic flow is at $Wi \cong 20$. Lip vortices are in a region of $20 \leq Wi \leq 40$ for $\beta = 8$ and $\beta = 16$ contraction flows. The corner vortex flow eventually emerges in all the contraction flows at a sufficiently high Wi, and appears to be strongly time-dependent in the contraction flows with $\beta = 8$ and $\beta = 16$. Unlike the flows at lower contraction ratios, the flow patterns occurred in the flow of $\beta = 16$ appear asymmetric in almost all viscoelastic flow regimes. The differences in their contraction ratio and aspect ratio could have a significant effect on vortex enhancement mechanism as already suggested by the 3D simulations of Omowunmi and Yuan (2010).

5.4 4:1 contraction flow

Fig. 5.3 shows the flow patterns of the $16.6c^*$ PAAm solution through a 4 : 1 contraction (the Flowcell 1) at $El = 25.5$, for a range of Wi ($5.9 \leq Wi \leq 88.2$). At low flow rate ($Wi \leq 14.7$), the flow is essentially Newtonian-like. At $Wi = 14.7$, the streamlines start to bend near the corners of contraction. At $Wi = 22.0$, two corner vortices become visible. These recirculation regions become larger as with Wi is increased. The flow patterns appeared to be symmetric and stable for the entire range of Wi flows studied, similar to the observations of Gulati et al. (2008) for the high El flow of a DNA solution through a 2 : 1 contraction. The flow patterns of 4 : 1 and 2 : 1 contraction flows with a shallow aspect ratio of the upstream channel are not dependent very much on El.

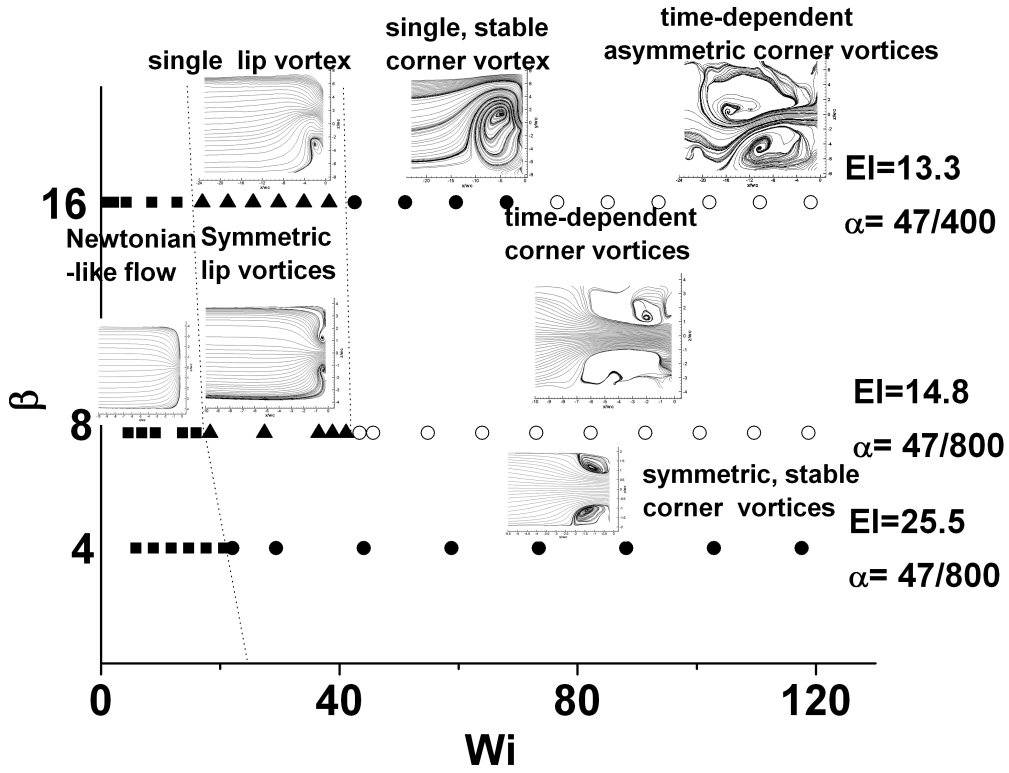

Figure 5.2: A summary of flow patterns in different contraction ratios as a function of *Wi*. Squares indicate Newtonian-like flow; triangles indicate lip vortex flow; circles indicate corner vortex flow. The filled symbols indicate apparently stable flow and the empty symbols indicate time-dependent flow.

5.5 8:1 contraction flow

5.5.1 Effect of *Wi* on viscoelastic flow behaviour

Fig.5.4 shows the flow patterns of the $8.3c^*$ and $16.6c^*$ PAAm solutions through a 8 : 1 contraction (the Flowcell 2) at $El = 14.8$ and 60.8, respectively, for a range of Wi ($4.6 \leq Wi \leq 91.3$). Note that El was changed by tuning the concentration of PAAm for a given flow geometry. Here the dependences of the flow patterns on Wi are very different from those observed in the 4 : 1 contraction flow. There is an onset of *lip* vortices at $Wi = 13.7$ for the flow of $El = 14.8$ and at $Wi = 20.6$ for the flow of $El = 60.8$. These flow structures grow slowly in size with increasing Wi. At $Wi \cong 40$, lip vortices are transformed into much larger corner vortices and their sizes depend more strongly on Wi. At even higher Wi the flow has a certain divergent feature, as can be seen in Fig. 5.4i and 5.4j. For PAAm solutions, the minimum Wi at which viscoelastic flows occur is considerably lower than what was

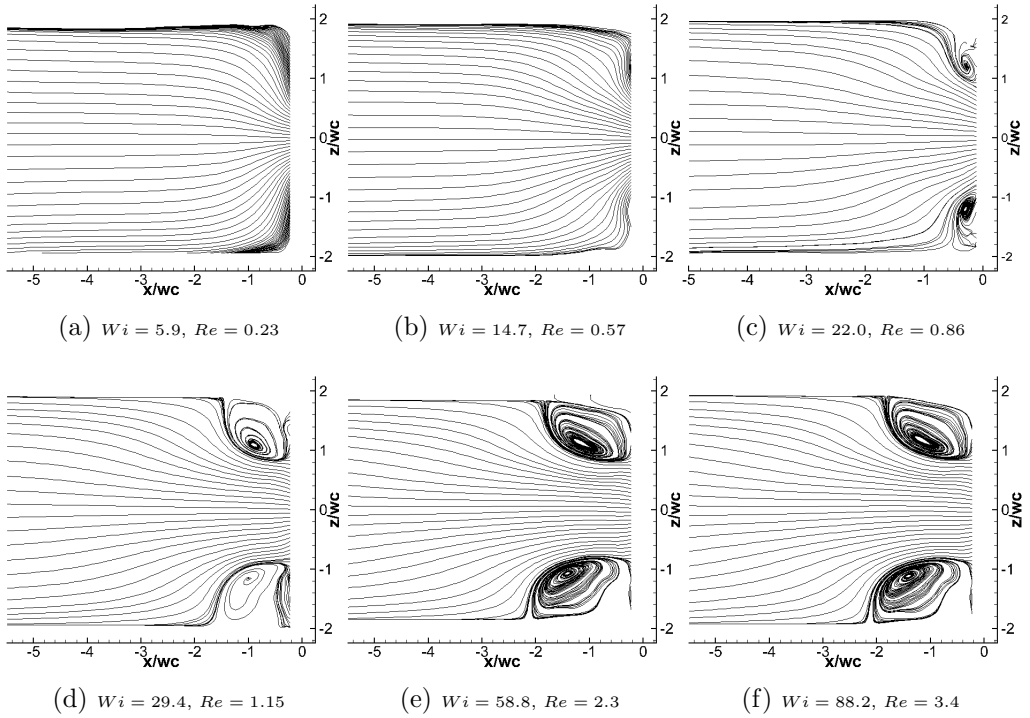

(a) $Wi = 5.9$, $Re = 0.23$ (b) $Wi = 14.7$, $Re = 0.57$ (c) $Wi = 22.0$, $Re = 0.86$

(d) $Wi = 29.4$, $Re = 1.15$ (e) $Wi = 58.8$, $Re = 2.3$ (f) $Wi = 88.2$, $Re = 3.4$

Figure 5.3: Time-averaged streamlines for the 16.6 c* PAAm solution through a 4 : 1 planar contraction (El = 25.5) at flow rates (a) $Q = 2$ ml/hr, (b) $Q = 5$ ml/hr, (c) $Q = 7.5$ ml/hr, (d) $Q = 10$ ml/hr, (e) $Q = 20$ ml/hr and (f) $Q = 30$ ml/hr.

observed ($Wi_t \cong 30$) by Li et al. (2011) for PEO solutions in a nearly identical 8:1 contraction flow geometry and in similar range of *El*. This could be a consequence of the higher molecular weight and broader molecular weight distribution of the PAAm sample used here.

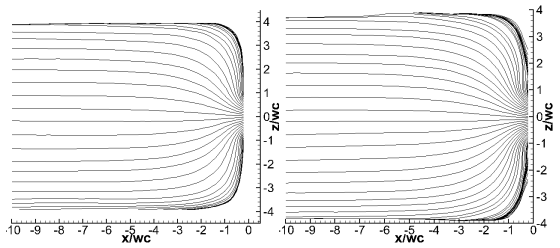

(a) $Wi = 4.6, Re = 0.31$ (b) $Wi = 5.9, Re = 0.1$

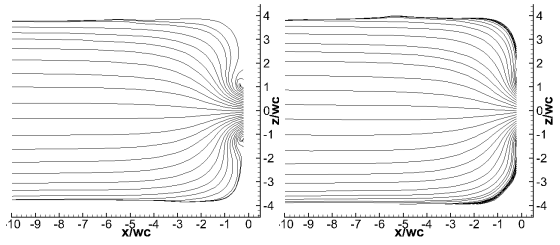

(c) $Wi = 13.7, Re = 0.93$ (d) $Wi = 14.7, Re = 0.24$

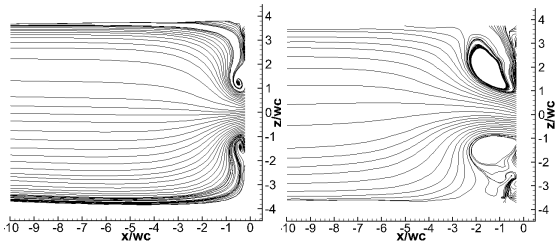

(e) $Wi = 18.3, Re = 1.23$ (f) $Wi = 20.6, Re = 0.34$

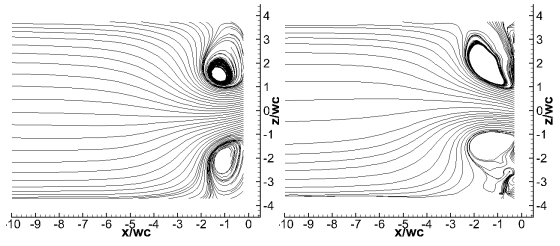

(g) $Wi = 43.4, Re = 2.93$ (h) $Wi = 38.2, Re = 0.63$

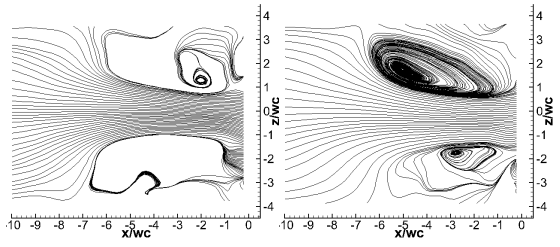

(i) $Wi = 91.3, Re = 6.15$ (j) $Wi = 82.3, Re = 1.37$

Figure 5.4: Typical flow patterns through a 8 : 1 planar contraction. The left column shows, from top to bottom, the velocity fields for the $El = 14.8$ flow of the 8.3 c* PAAm solution at flow rates $Q = 0.5$, 1.5, 2, 4.75 and 10 ml/hr respectively. The right column shows, from top to bottom, the velocity fields for the $El = 60.8$ flow of the 16.6 c* PAAm solution at flow rates $Q = 0.5$, 1.25, 1.75, 3.25 and 7 ml/hr respectively.

5.5.2 Effect of *El* on vortex dynamics

Fig. 5.5 reports the temporal evolution of streamlines in the flows of $El = 14.8$ and $El = 60.8$, respectively, at a similar Wi ($Wi \cong 20$) in the lip vortex flow regime. The vortex structures appear time-dependent in the low El flow. Increasing the Elasticity number (relatively decreasing the flow inertia) results in markedly more stable steady lip vortices as shown in the flow of $El = 60.8$. Fig. 5.6 shows the temporal evolution of streamlines for the both El flows in the corner vortex flow regime at an high Wi ($Wi \cong 90$). In the both cases, the vortex structures appear strongly time-dependent, and the streamlines in the vortex region are less closed and are three-dimensional in nature, especially for the low El flow. The vortex was originated near the wall (Fig. 5.6a), then propagated toward the upstream (Fig.5.6c). There is even coexistence of two vortices on the one side of the flow channel (Fig.5.6a, 5.6c and 5.6e). The phenomena are more pronounced in the low El flow, and exhibit strong interplay between elastic and inertial forces.

These results also show that increasing Re at a fixed Wi (thus reducing El) stabilizes the elastic flow structures, while magnitude and location of the vortices remain approximately the same. This is in agreement with several previous studies by Rodd et al. (2005a, 2007) and by Li et al. (2011).

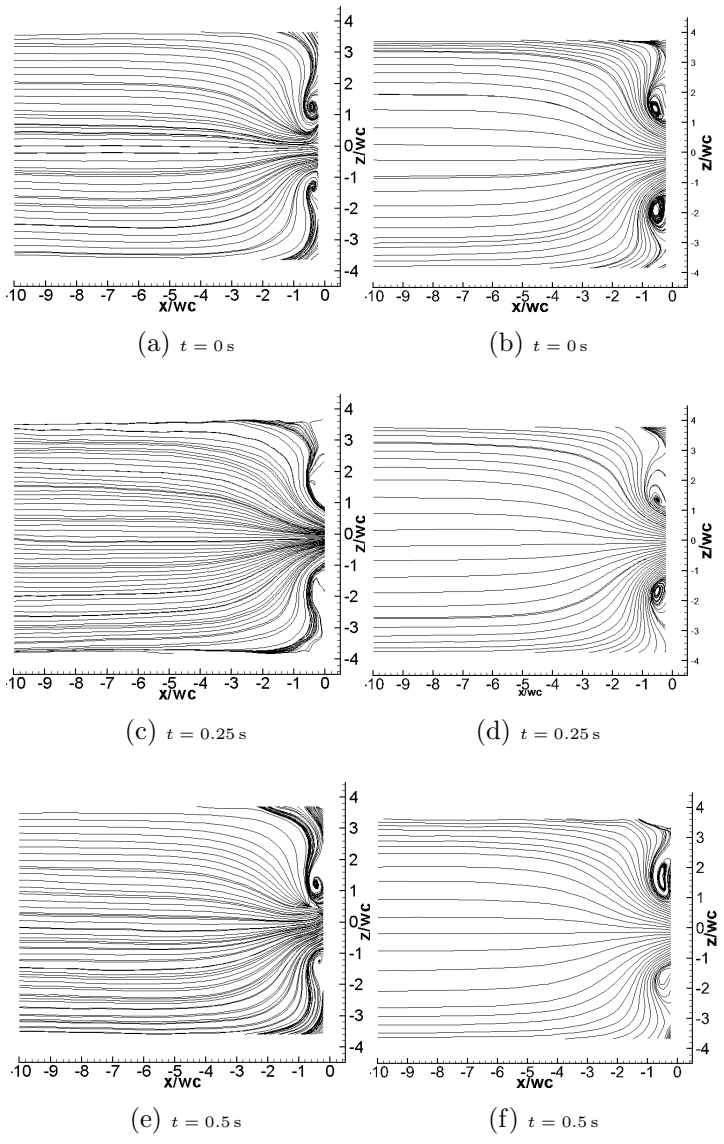

(a) $t = 0\,\mathrm{s}$ (b) $t = 0\,\mathrm{s}$

(c) $t = 0.25\,\mathrm{s}$ (d) $t = 0.25\,\mathrm{s}$

(e) $t = 0.5\,\mathrm{s}$ (f) $t = 0.5\,\mathrm{s}$

Figure 5.5: Time evolution in 8 : 1 contraction flow and under the lip vortex flow regime. The left column is for the $El = 14.8$ flow of the $8.3c^*$ PAAm solution at $Q = 2$ ml/hr, $Wi = 18.3$ and $Re = 1.23$. The right column is for the $El = 60.8$ flow of the $16.6c^*$ PAAm solution at $Q = 1.75$ ml/hr, $Wi = 20.6$ and $Re = 0.34$.

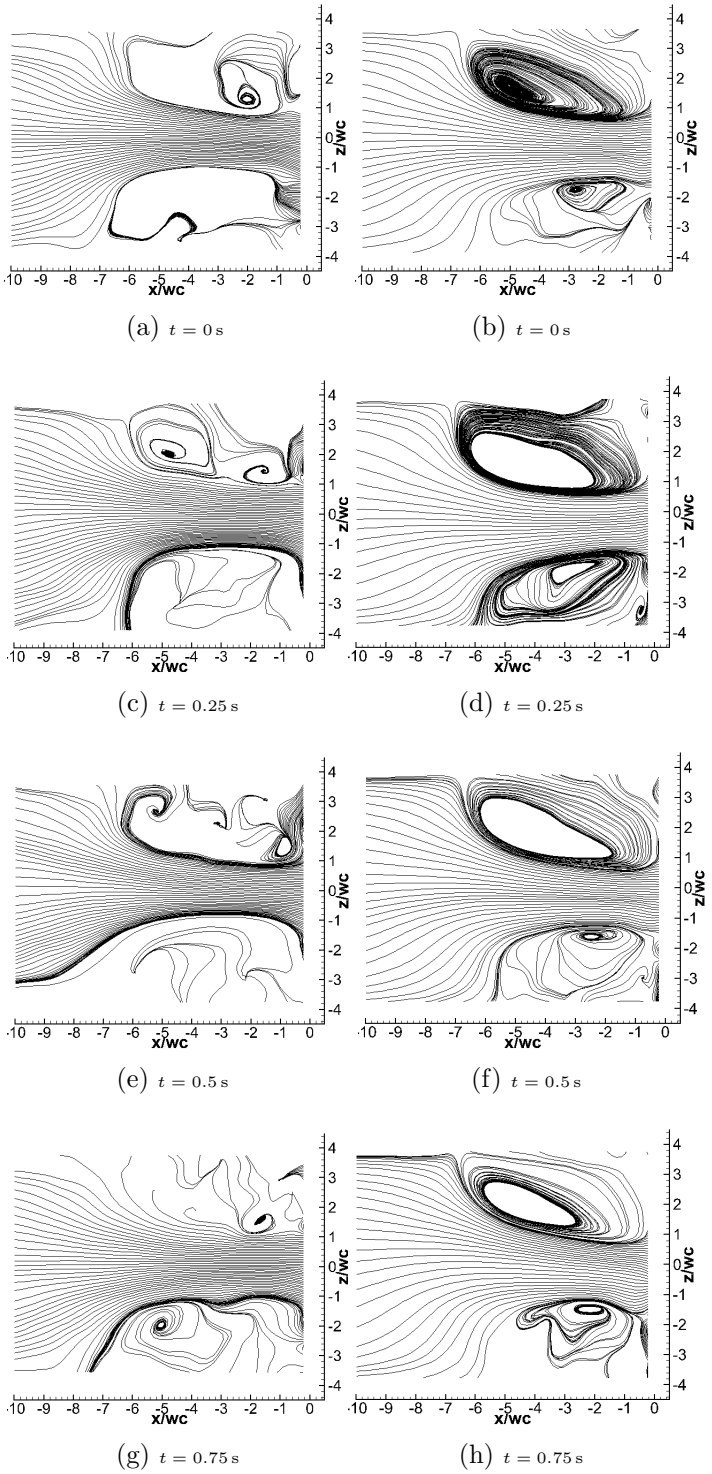

(a) $t = 0\,\mathrm{s}$ (b) $t = 0\,\mathrm{s}$

(c) $t = 0.25\,\mathrm{s}$ (d) $t = 0.25\,\mathrm{s}$

(e) $t = 0.5\,\mathrm{s}$ (f) $t = 0.5\,\mathrm{s}$

(g) $t = 0.75\,\mathrm{s}$ (h) $t = 0.75\,\mathrm{s}$

Figure 5.6: Time evolution of streamlines in the 8:1 contraction flow and under the high Wi flow regime. The left column is for the $El = 14.8$ flow of the $8.3c^*$ PAAm solution at $Q = 10$ ml/hr, $Wi = 91.4$ and $Re = 6.2$. The right column is for the $El = 60.8$ flow of the $16.6c^*$ PAAm solution at $Q = 7$ml/hr, $Wi = 82.3$ and $Re = 1.36$.

5.6 16:1 contraction flow

5.6.1 Effect of *Wi* on viscoelastic flow behaviour

Fig.5.7 shows the flow patterns of the $3.3c^*$ and $16.6c^*$ PAAm solutions in a 16:1 contraction flow (the Flowcell 3) at $El = 13.3$ and 476.8 respectively, in a range of Wi ($8.8 \leq Wi \leq 131.7$). Fig. 5.7a and 5.7b are time-averaged over 50 consecutive images, and the others are instantaneous captures. A *single* lip vortex starts to emerge near the contraction throat at $Wi \cong 35$. In a similar manner to what observed in the 8 : 1 contraction flow, the lip vortex rapidly grows into a much larger corner vortex with a small increase of Wi. The corner vortex appears to be bigger in the lower El flow. At $Wi \cong 75$, another smaller secondary corner vortex becomes visible. At even higher Wi, the both vortices grow to approximately a same size, as can be seen in Fig. 5.7i and 5.7j. Again, the minimum Weissenberg number ($Wi = 35$) at which the lip vortex occurs in the 16 : 1 contraction flow is significantly lower than that reported by Rodd et al. (2005a) for PEO solutions in a similar flow geometry but $El \leq 8.4$.

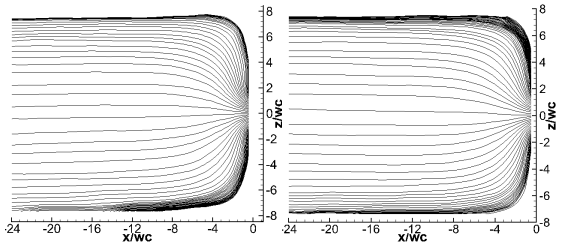

(a) $Wi = 8.8$, $Re = 0.72$ (b) $Wi = 9.6$, $Re = 0.02$

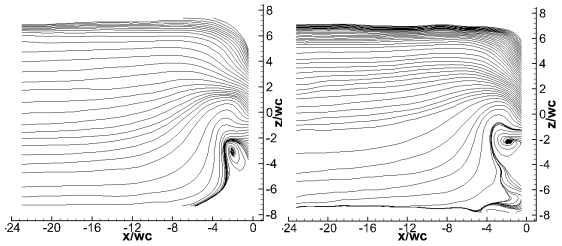

(c) $Wi = 34.0$, $Re = 2.75$ (d) $Wi = 37.6$, $Re = 0.08$

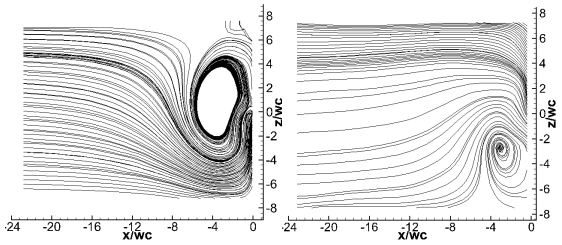

(e) $Wi = 38.25$, $Re = 3.1$ (f) $Wi = 56.4$, $Re = 0.12$

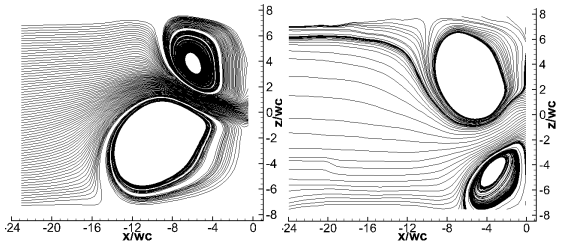

(g) $Wi = 76.6$, $Re = 6.2$ (h) $Wi = 75.3$, $Re = 0.16$

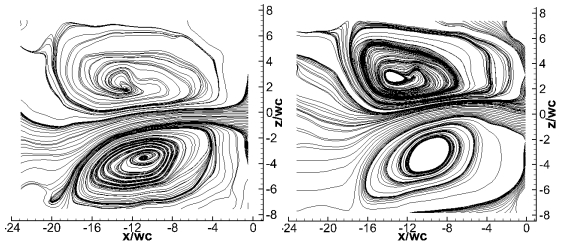

(i) $Wi = 119.1$, $Re = 9.6$ (j) $Wi = 131.7$, $Re = 0.28$

Figure 5.7: Typical flow patterns through a 16 : 1 planar contraction. The left column shows, from top to bottom, the velocity fields for the $El = 13.3$ flow of the $3.3c^*$ PAAm solution at flow rates $Q = 0.2$, 0.8, 0.9, 1.8 and 2.8 ml/hr respectively. The right column shows, from top to bottom, the velocity fields for the $El = 476.8$ flow of the $16.6c^*$ PAAm solution at flow rates $Q = 0.05$, 0.2, 0.3, 0.4 and 0.7 ml/hr respectively.

5.6.2 Effect of *El* on vortex dynamics

The effect of *El* on the stability of the flow pattern in the single lip vortex flow regime is shown in Fig. 5.8. For the lower *El* flow, vortex is always located at a nearly same position ($z/w_c \cong -3$). For the flow of $El = 476.8$, it periodically *flips* between the two re-entrant corners. Such a bistable character of vortex dynamics at an high Elasticity number flow could be used in a microfluidic logic device as suggested by Groisman et al. (2003). Different from what was observed in a moderate *Wi* flow, in the double vortex flow regime ($Wi \cong 120$) the temporal flow patterns of the different *El* flows are very similar. In contrast to the results of Rodd et al. (2005a) (increasing *El* makes the flow more stable), it was found that increasing *El* in a window of *Wi* ($35 \leq Wi \leq 75$) actually results in a much more time-dependent evolution of vortex structures. These differences could be attributed to various factors, such as the much longer downstream channel adopted in this work, a much higher *El* flow ($El = 476.8$ vs. $El \leq 89$ in the work of Rodd et al. (2005a)), and the much higher average molecular weight and molecular weight distribution of PAAm samples used here.

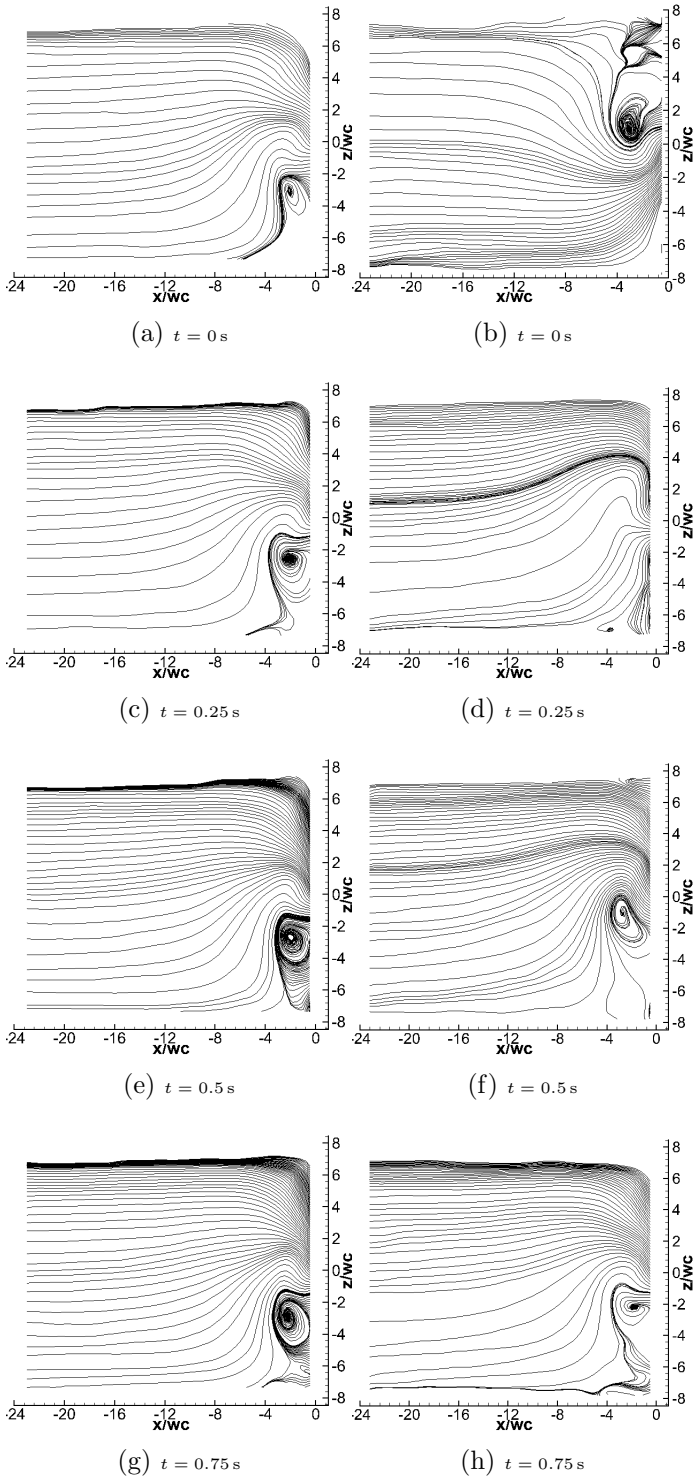

(a) $t = 0\,\mathrm{s}$ (b) $t = 0\,\mathrm{s}$

(c) $t = 0.25\,\mathrm{s}$ (d) $t = 0.25\,\mathrm{s}$

(e) $t = 0.5\,\mathrm{s}$ (f) $t = 0.5\,\mathrm{s}$

(g) $t = 0.75\,\mathrm{s}$ (h) $t = 0.75\,\mathrm{s}$

Figure 5.8: Time evolution of the streamlines for two El flows for $\beta = 16$ in the single lip vortex flow regime. The left column is for the $El = 13.3$ flow of the $3.3c^*$ PAAm solution at $Q = 0.8$ ml/hr, $Wi = 34.0$ and $Re = 2.6$. The right column is for the $El = 476.8$ flow of the $16.6c^*$ PAAm solution at $Q = 0.2$ ml/hr, $Wi = 37.6$ and $Re = 0.08$.

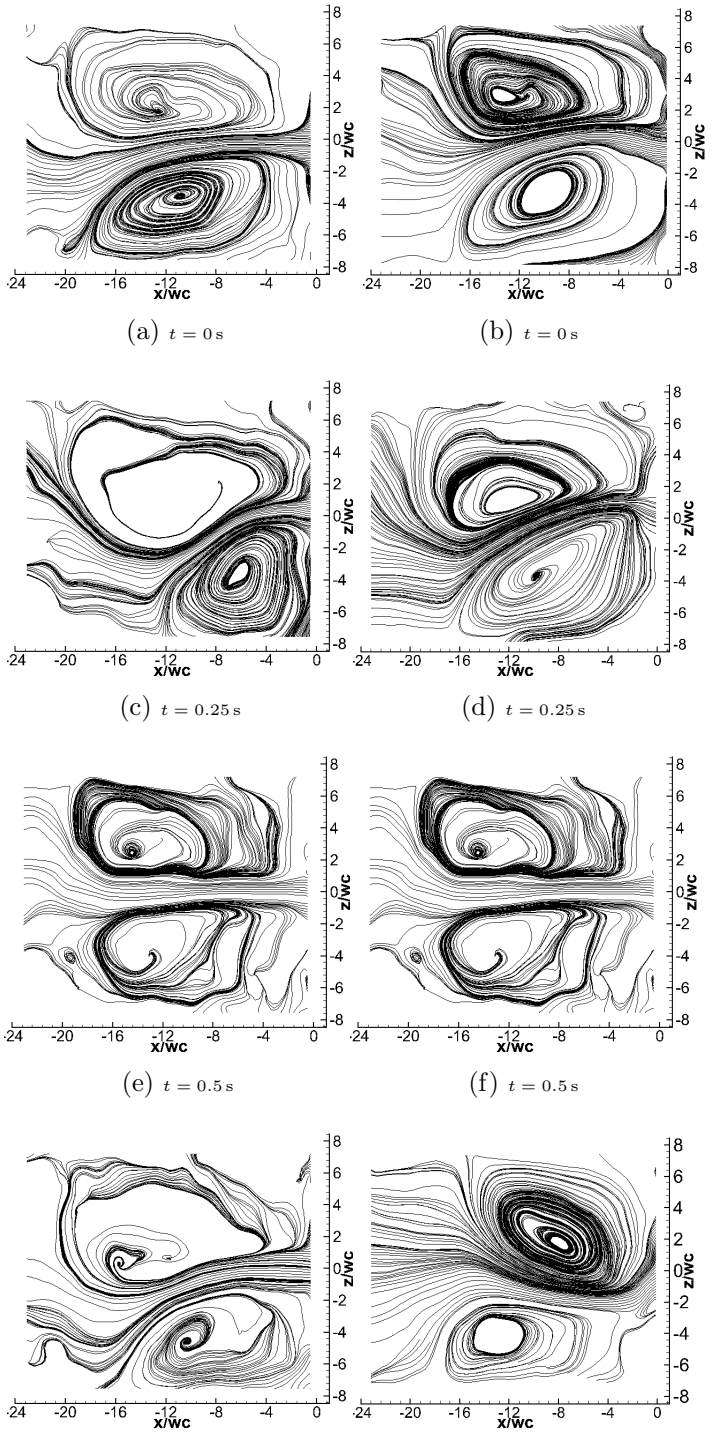

(a) $t = 0\,\mathrm{s}$ (b) $t = 0\,\mathrm{s}$

(c) $t = 0.25\,\mathrm{s}$ (d) $t = 0.25\,\mathrm{s}$

(e) $t = 0.5\,\mathrm{s}$ (f) $t = 0.5\,\mathrm{s}$

(g) $t = 0.75\,\mathrm{s}$ (h) $t = 0.75\,\mathrm{s}$

Figure 5.9: Time evolution of the streamlines for two El flows with $\beta = 16$ in the double corner vortex flow regime. The left column is for the $El = 13.3$ flow of the $3.3c^*$ PAAm solution at $Q = 2.8$ ml/hr, $Wi = 119.0$ and $Re = 9.1$. The right column is for the $El = 476.8$ flow of the $16.6c^*$ PAAm solution at $Q = 0.7$ ml/hr, $Wi = 131.6$ and $Re = 0.28$.

5.7 Centreline velocity profiles and local elongational rates

The centreline velocity profiles, normalized by the average upstream velocity, $< v >= \frac{Q}{hw_u}$, for the flows with the contraction ratio $\beta = 4$, $El = 25.5$ and $\beta = 8$, $El = 14.8$ are plotted in Fig. 5.10a and Fig. 5.11a, respectively, over a range of Wi ($5.9 \leq Wi \leq 73.5$ and $4.6 \leq Wi \leq 82.2$). A steady state flow can be reached in all the 4:1 contraction flow and in the 8:1 contraction flow at low flow rate ($Wi \leq 40$). Their velocity profiles were then extracted from ensemble-averaged micro-PIV vector fields over 50 consecutive captures. For other time-dependent flow the centreline velocity profiles were extracted from an instantaneous velocity field as long as its streamline bunch close to the flow axis is nearly symmetric. For the flow of $\beta = 8$, the measured velocity profile in the Newtonian flow regime at $Q = 2$ ml/hr is also plotted for a comparison. In the $4:1$ contraction flows, the velocity profile at $Wi = 29.4$ significantly deviates from that at a lower Wi ($Wi = 5.9$) because the flow has entered the corner vortex flow regime. At $Wi \geq 44.1$, the centreline velocities are approximately linearly increased along the flow axis. These observations are very different from the PTT-model based numerical simulations of Alves et al. (2004) for two-dimensional $\beta = 4$ contraction flow, for which the dimensionless velocity profiles do not depart from the Newtonian one up to $Wi = 100$. The results here presented are also in a great contrast with the observations of Gulati et al. (2008) for the $El = 10^5$ flow of a DNA solution through a $2:1$ contraction (thus with a lower nominal Hencky strain than what reported here), which did not report any such centerline velocity profile up to $Wi \cong 188$. In the $8:1$ contraction flow, at low Wi the velocity profile is very similar to the Newtonian fluid. The velocity acceleration region shifts toward the upstream region when the lip vortices occur from $Wi \geq 13.7$. At $Wi = 73.1$, the presence of large corner vortices is reflected by the appearance of a minimum in the velocity profile at $x/w_c \cong -0.5$, which moves slightly into the upstream region with further increase of Wi. The addition of polymer to water results in a dramatic change of the dimensionless velocity profile

even for close values of Re, as shown by a comparison between the velocity profile of water at a flow rate $Q = 2$ ml/hr (thus at $Re = 6.54$) and the one for the flow of the $16.6c^*$ PAAm solution at $Q = 9$ ml/hr (thus at $Re = 5.55$). Li et al. (2011) also reported a minimum in the centreline velocity profile in the lip vortex regime, but it occurs at a lower Wi ($\cong 30$), for a PEO solution in flow of $El = 20$. It is interesting that, even though the flow geometry is very similar and the values of Wi and El are close, the dependence of the velocity profile on the flow rate in the PAAm and the PEO solutions is still significantly different.

The profile of extensional rate can be readily calculated from the centreline velocity profile to reveal the deformation history undergone by PAAm molecules flowing along the centreline and to provide some physical insight to the nonlinear fluid dynamics. The profiles of extensional rate are shown in Fig. 5.10b and in Fig. 5.11b. In flow of $\beta = 4$, $El = 25.5$, the local extensional rates are systematically increased as the flow rate is increased, and become approximately constant for $Wi \geq 44.1$. In the higher contraction flows, the profile of the local extensional rate increases as the flow rate is increased over a range of Weissenberg numbers $4.6 \leq Wi \leq 27.4$. The onset of the velocity *minima* in the high Wi flow regime is coupled with a strong uniaxial compression-extension mechanism: the extensional rates become negative prior the contraction, before reaching positive values in the vicinity of the contraction plane. At a similar value of El, nearly a constant extensional rate in the 4 : 1 contraction geometry over a wide range of Wi make itself advantageous over the 8 : 1 contraction geometry (at expense of smaller Hencky strain) if flow of a constant local extensional rate was required.

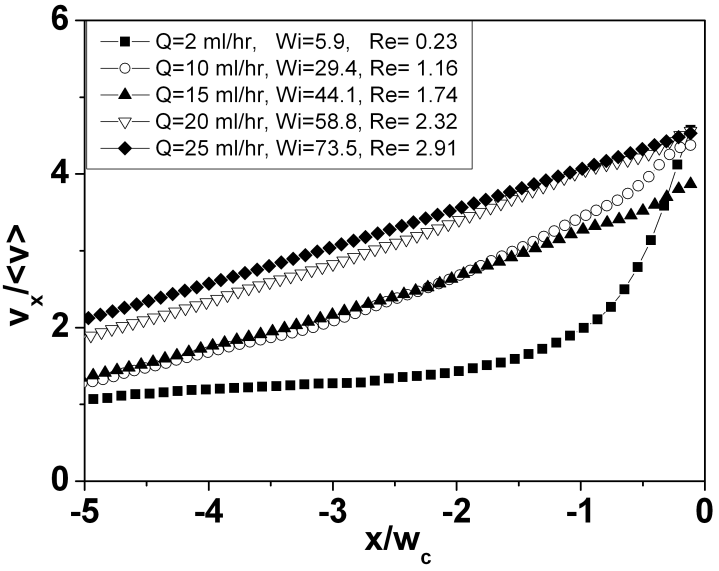

(a)

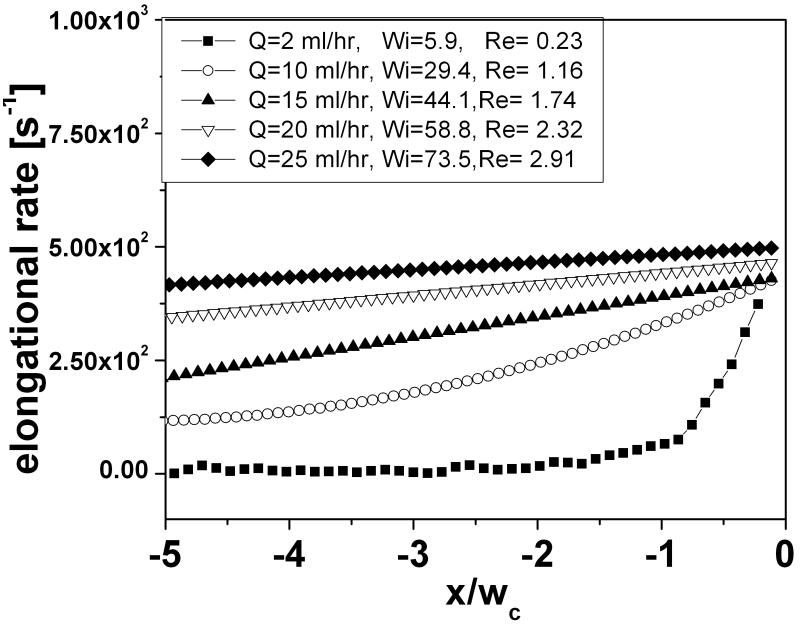

(b)

Figure 5.10: Effect of Wi on centreline velocity profiles for the flows of $El = 25.5$, $\beta = 4$ (a) and on the correspondent local elongational rates (b).

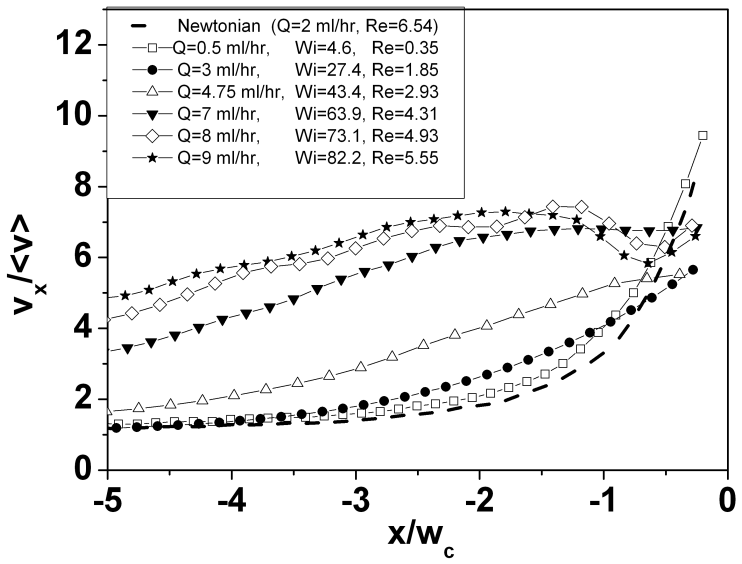

(a)

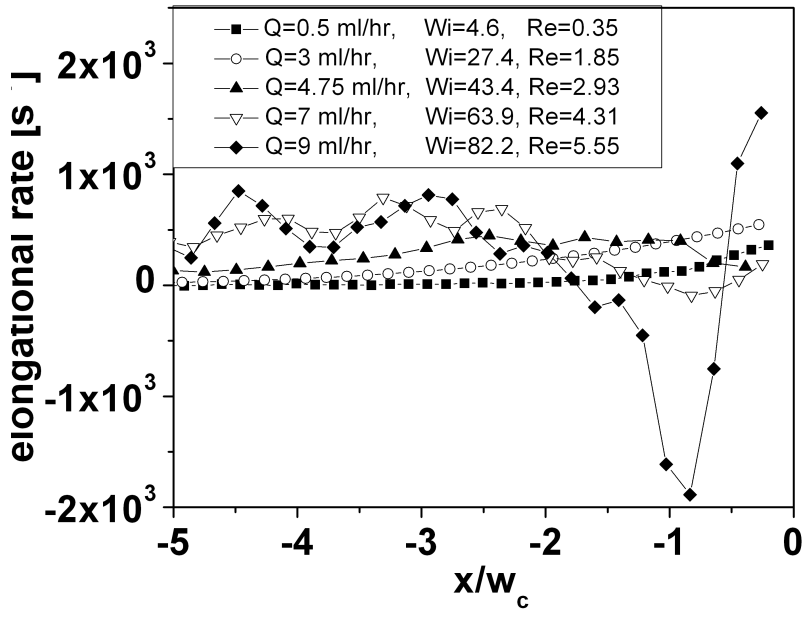

(b)

Figure 5.11: Effect of Wi on centreline velocity profiles for the flows of $El = 14.8$, $\beta = 8$ (a) and on the correspondent local elongational rates (b).

5.8 Vortex size

The non-dimensional vortex size defined as L_v/w_c, is plotted in Fig. 5.12 as a function of *Wi*. For the 16 : 1 contraction flow, in which vortex mechanisms are always asymmetric, only the results of the biggest size of vortex are presented. For the 4 : 1 and 8 : 1 contraction flows, the characteristic vortex sizes approximately collapse into a single curve, having nearly linear dependence on *Wi*. This could be due to the fact that symmetric corner vortices were observed over a large range of *Wi*, $38.2 \leq Wi \leq 120$ for $\beta = 4$, and $38 \leq Wi \leq 130$ for $\beta = 8$. Not only exhibiting highly asymmetric flow nature, the vortex sizes in the 16 : 1 contraction flow are also bigger than those in the lower contraction flows. The higher *El*, the bigger the vortex sizes. The dependence of vortex size on *Wi* is nonlinear. It simply reflects the fact that the transition from single lip to single corner vortex regime at $Wi \cong 40$ is accompanied by a sudden increase in the vortex size.

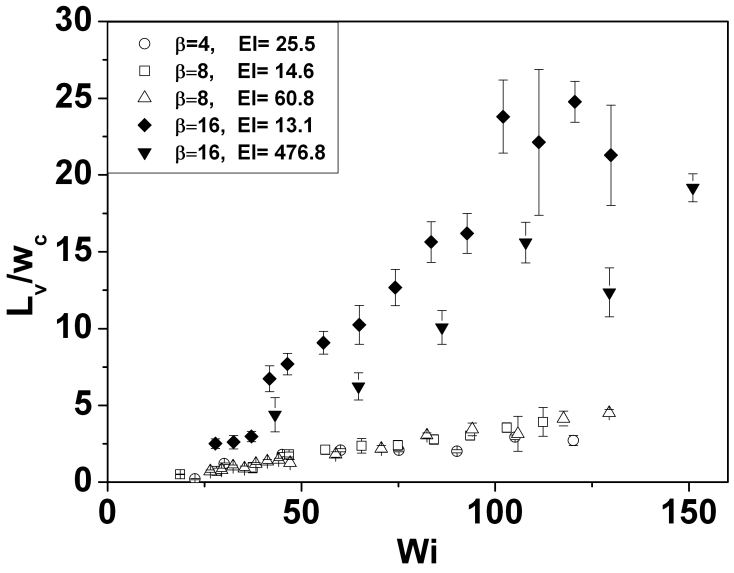

Figure 5.12: Plot of the vortex size as a function of *Wi*.

5.9 Excess pressure drop and correlation with vortex size

In order to reveal the dependence of pressure drops on the various flow regimes in the contraction flow, a dimensionless excess pressure drop $\Delta P'$ was introduced. It is defined as (with reference to Fig. 3.3):

$$\Delta P' = \frac{\Delta P_{12} - \Delta P_{1'2'} - \Delta P_s}{\Delta P_s} \tag{5.4}$$

where ΔP_{12} is the mean steady state pressure drop measured between P_1 and P_2, $\Delta P_{1'2'}$ is the pressure drop directly measured over the 20 mm middle section of a 40 mm long straight microchannel, with the same cross-section as the narrow channel of the contraction-expansion flow geometry. $\Delta P_s = \Delta P_{11'} + \Delta P_{2'2} = [\frac{d(\Delta P_{12} - \Delta P_{1'2'})}{dWi}] \cdot Wi$ accounts for the shear predominated contribution to pressure drops in upstream and downstream large channels, and is obtained by fitting the diagram of $\Delta P_{12} - \Delta P_{1'2'}$ in the limit of $Wi \to 0$.

ΔP_{12} and $\Delta P_{1'2'}$ are plotted as a function of Wi in Fig. 5.13a and 5.13b for the $\beta = 8$, $El = 14.8$ and $\beta = 16$, $El = 13.3$ contraction flows, respectively. Pressure data are superimposed with the data of the non-dimensional vortex sizes. ΔP_{12} start to deviate from the data of the narrow channel as Wi is increased. $\Delta P'$ as a function of Wi are presented in Fig. 5.14a and 5.14b. For the $8:1$ contraction, four flow regimes can be clearly identified. At $Wi \leq 20$, where the flow is essentially Newtonian-like, $\Delta P'$ is zero, then it suddenly increases with Wi, in the vortex growth flow regime. After reaching a maximum at $Wi \cong 150$, $\Delta P'$ decreases, as polymer chains have reached their finite extendibility, before approaching a plateau at even higher Wi.

Fig. 5.14b shows $\Delta P'$ as a function of Wi for the flow of $\beta = 16$ and $El = 13.3$. The first increase of $\Delta P'$ approximately corresponds to the onset of the single lip vortex ($Wi \cong 25$). When flow enters the single corner vortex regime ($40 \leq Wi \leq 70$ approximately), the sudden increase in vortex size is accompanied by a significant increase of $\Delta P'$. At even higher Wi, the formation of a secondary vortex

is accompanied by a decrease of $\Delta P'$. Thus, the single corner vortex flow regime could be responsible for the peak in dimensionless excess pressure drop. Different contraction ratios result in a different behaviour of $\Delta P'$ even at a close value of *El*.

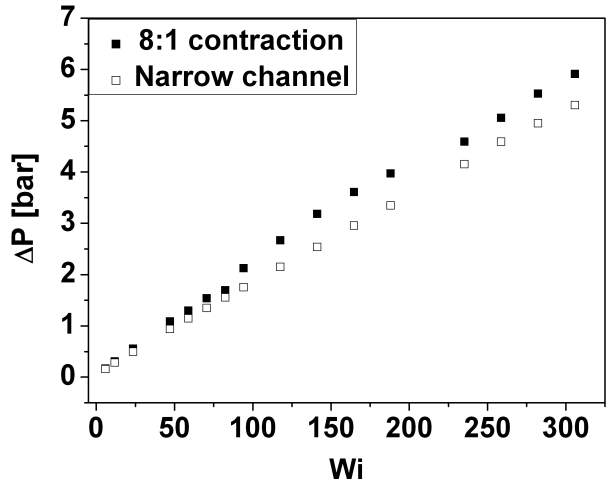

(a)

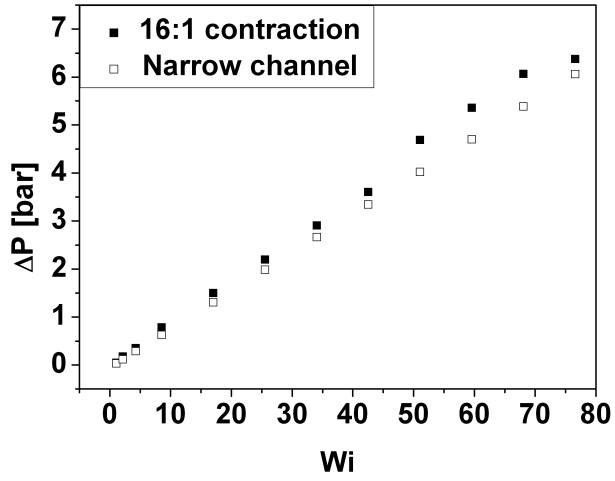

(b)

Figure 5.13: Pressure drops measured across the contraction-expansion flow and the straight narrow channel flow for the 0.25 wt.% PAAm in the $8:1$ contraction flow (a), and for the 0.1 wt.% PAAm in the $16:1$ contraction flow (b).

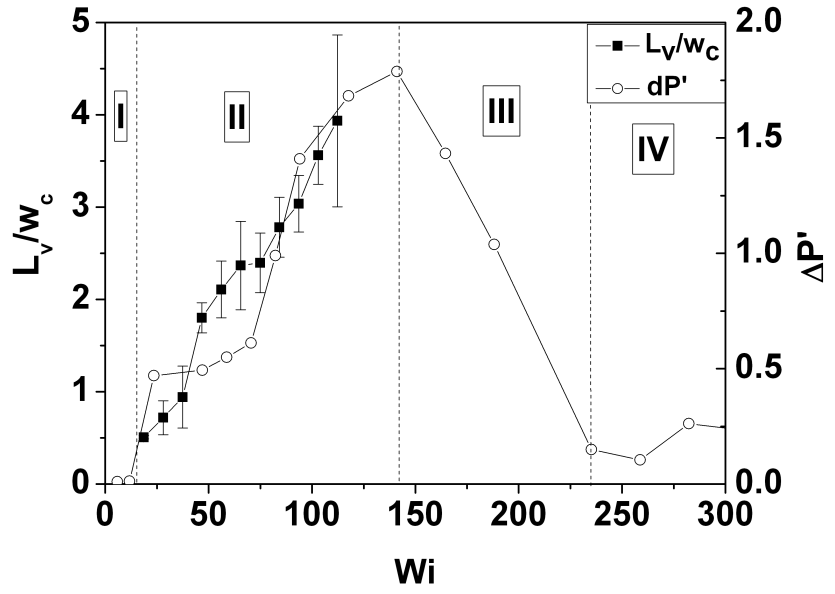

(a)

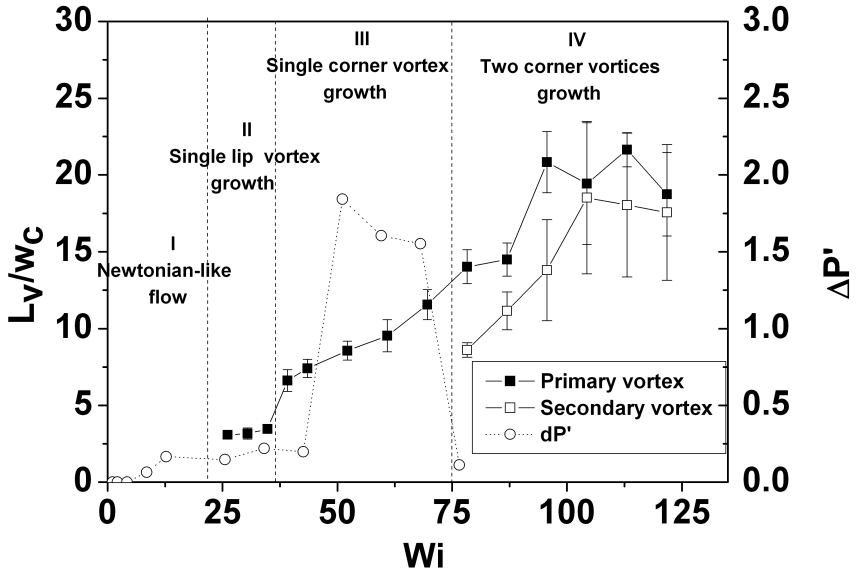

(b)

Figure 5.14: Dimensionless excess pressure drop vs. Wi for the flow of $\beta = 8$, $El = 14.8$ (a) and for the flow of $\beta = 16$, $El = 13.3$ (b).

Chapter 6

Quantitative analysis of non-linear dynamics in microfluidics

6.1 Introduction

In Chapter 5, non-linear dynamics of the contraction flows of highly polydisperse PAAm solutions are presented. The vortex growth mechanisms are caused by the high elongational viscosity of polymer solutions. When the fluid approaches the contraction plane, the polymer chains are extended and large elastic stresses are generated as a consequence. Thus, in order to gain a better understanding of the high Wi flows through contraction geometries, it is important to link the quantitative flow measurements with polymer deformation within fluid elements. This will require quantifying the local stretch experienced by the polymer chains, hence to relate the stress field across the entire flow geometry, if the constitutive relationship is known.

Moreover, simultaneous measurements of the local deformation rate field and of the pressure distribution along the flow geometry would allow for a better design of microfluidic rheometers.

As it has been shown in many examples in Chapter 5, the complex flows through sudden contractions are such that some streamlines are curved, especially in the vicinity of the contraction throat. Moreover, the nonlinear flows are often highly asymmetric and time-dependent in high Wi flow. It is therefore very important to choose a relevant reference frame to evaluate the local deformation rate along

the velocity direction, such as the streamline coordinate system, which has been used in the past for better simulations of complex viscoelastic fluid flows (Finnigan, 1983; Luo and Tanner, 1986a,b). This Chapter will present a numerical method to compute the local extensional rate experienced by fluid elements along the flow direction from the velocity field data obtained by micro-particle image velocimetry. It will be used to extract useful quantitative information from the experimental data presented in Chapter 5.

6.2 Definitions

Let us consider a velocity vector field V which describes the flow of a given fluid at a fixed instant t. As shown in Fig. 6.1, a streamline s is a line that is everywhere tangent to the velocity field. Given $\underline{v} \in \mathbf{V}$ located at the point $\underline{r} = (x, z)$ measured from the origin $\underline{O}$, the streamline which passes by $\underline{r}$ satisfies the equation:

$$\frac{dx}{v_x} = \frac{dz}{v_z}. \tag{6.1}$$

The streamline describes a trajectory of an infinitesimal fluid element P that is imagined to move along the flow. The positions of P along s at given "fictitious times" τ and $\tau + d\tau$, as measured from the origin $\underline{O}$, are given by $\underline{r}(\tau)$ and $\underline{r}(\tau + d\tau)$, which correspond to local speeds of the fluid element v_ξ and $v_\xi + \partial v_\xi$ respectively.

The distance percurred in $d\tau$ by the fluid element P travelling along s is given by:

$$\partial\xi = \left|\underline{r}(\tau + d\tau) - \underline{r}(\tau)\right|. \tag{6.2}$$

Thus, the local extensional rate $\dot{\varepsilon}$ can be calculated by:

$$\dot{\varepsilon}(\underline{r}, t) = \frac{\partial v_\xi}{\partial \xi}. \tag{6.3}$$

Eq. 6.3 is used to define the *local Deborah number* De:

$$De(\underline{r}, t) = \lambda \left|\dot{\varepsilon}\right| \tag{6.4}$$

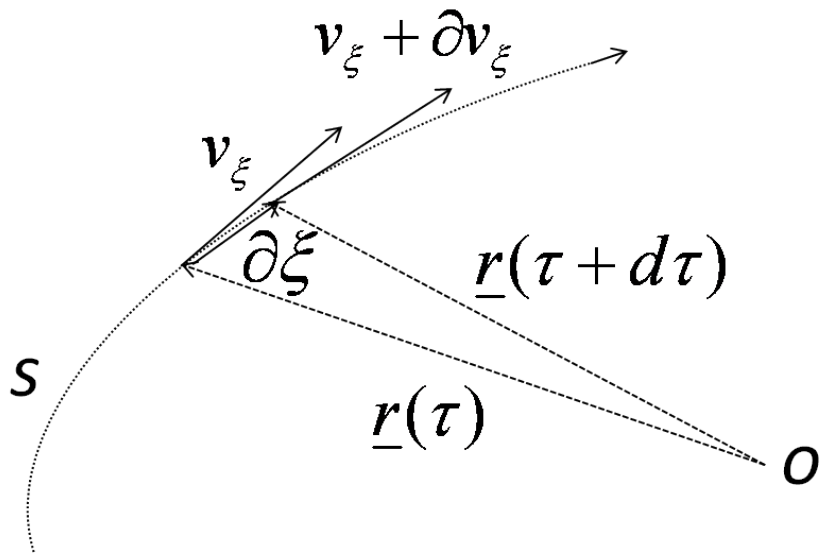

Figure 6.1: Schematic diagram of the path of a massless fluid element along a streamline. The positions of such a particle at τ and $\tau + d\tau$ are denoted as $\underline{r}(\tau)$ and $\underline{r}(\tau + d\tau)$.

where λ is a characteristic relaxation time of the fluid, and can be measured separately, as shown in Chapter 3 and Chapter 4. From its definition, the local Deborah number is an instant measure of the strength of the extension or compression rate experienced by fluid elements moving along the flow field. Thus, it gives an indication of the local stretch experienced by the polymer chains at local flow conditions. Different from the nominal Weissenberg number defined in Section 2.4, and used in Chapter 5 and in the literature, *De* cannot be estimated *a priori*, but is experimentally measured from an instantaneous velocity field.

It must be stressed out that, as observed by Keller and Odell (1985), in order to fully stretch a polymer chain under extensional flow it is necessary not only to impose an extensional rate comparable to the inverse of the fluid relaxation time, but also to maintain it for a long enough time, so that the polymer macromolecule will accumulate a sufficient strain. This suggests that, in order to completely quantify the elongational deformation of polymer chains in complex flow, not only the local Deborah number, but also the total strain accumulated by the fluid elements must be quantified. The numerical method presented in the following pages only allows for quantifying the *De* field from $\mu - PIV$ measurements of complex flows in microfluidics. The development of a method for computing the total strain along individual pathline from experimental velocimetry data should thus be subject of

future work.

6.3 Implementation of the numerical method

6.3.1 Streamlines integration and processing

Let $\mathbf{V}$ be a two-dimensional instant or ensemble-averaged velocity vector field obtained from PIV. Given $\underline{v} = (v_x, v_z) \in \mathbf{V}$ located at $\underline{r} = (x, z)$, the streamline s which passes by $\underline{r}$ should satisfy the equation:

$$\frac{dx}{v_x} = \frac{dz}{v_z}. \tag{6.5}$$

Let $dx = v_x d\tau$ and $dz = v_z d\tau$, where τ is a time interval. Eq. 6.5 can be rewritten as:

$$\underline{v} = \frac{d\underline{r}}{d\tau}. \tag{6.6}$$

The integration of Eq. 6.6 yields:

$$\underline{r}(\tau + h) = \underline{r}(\tau) + \int_{\tau}^{\tau+h} \underline{v} d\tau \tag{6.7}$$

where h is an integration step size. Eq. 6.7 is useful to determine two consecutive points $\underline{r}(\tau)$ and $\underline{r}(\tau + h)$ along s. The streamlines can be generated from any 2D velocity fields by a predictor-corrector algorithm provided in Tecplot Focus 2008 software (Tecplot Inc.). It integrates Eq. 6.6 numerically by the two-step, second order Runge-Kutta method to obtain the points of every streamline. A bi-linear interpolation of the experimental data is performed to evaluate the velocity vectors along the streamline. The initial point from which each streamline is drawn, the integration step size and the maximum number of steps N_{max} computable for every streamline are required to be specified. The software can reduce h up to a pre-fixed value h_{min}, if more than one interrogation area is jumped during each integration step, or if the boundaries of the measurement region are encountered.

If $\underline{r}_i = (x_i, z_i)$ and $\underline{r}_{i+1} = (x_{i+1}, z_{i+1})$ are two consecutive points along s, at

which the speeds are $|\underline{v}_i|$ and $\left|\underline{v}_{i+1}\right|$ respectively, the distance from $\underline{r}_i$ to $\underline{r}_{i+1}$ is given by $\Delta\xi(\underline{r}_i) = \sqrt{(x_i - x_{i+1})^2 + (z_i - z_{i+1})^2}$. The local elongational rate $\dot{\varepsilon}(\underline{r}_i)$ and the local Deborah number $De(\underline{r}_i)$ are computed as follows:

$$\dot{\epsilon}(\underline{r}_i) = \frac{|\underline{v}_i| - \left|\underline{v}_{i+1}\right|}{\Delta\xi(\underline{r}_i)} \tag{6.8}$$

$$De(\underline{r}_i) = \lambda_{CaBER}\,|\dot{\varepsilon}(\underline{r}_i)| \tag{6.9}$$

where λ_{CaBER} is the CaBER-determined fluid relaxation time (see Section 4.5).

6.3.2 Effect of integration step size on local Deborah number

The streamlines with respect to a measured velocity field in contraction flow were computed starting from the contraction plane, $x = 0$, and moving toward the upstream of the flow until far away from the contraction region. In order to evaluate the effect of changing the integration step h on the estimated De, the method described in Section 6.3.1 has been evaluated using an ensemble averaged velocity vector field for the $El = 60.8$, $Wi = 35.3$ flow of the $16.6c^*$ PAAm solution through a 8:1 contraction as shown in Fig. 6.2a. The profiles of the local Deborah number calculated along the central streamline $z = y = 0$ for 4 different integration step sizes are shown in Fig. 6.2b. Here the black symbols indicate the results from a direct differentiation of the centreline velocity with one sampling point per each interrogation area. The other four curves were computed along the central streamline with various integration steps. The curves are basically overlap each other. The shorter $|h|$, the higher the density of points. The De intensity pattern corresponding to the velocity field in Fig. 6.2a is given in Fig. 6.2c. The maximum values of De, as measured along all the velocity field in Fig. 6.2a, are listed in Table 6.1. The intensity patterns of De presented in the following paragraphs have been obtained using a step size $h = -1$ s, a minimum step size $h_{min} = 10^{-3}$ s and a maximum number of steps $N_{max} = 1000$.

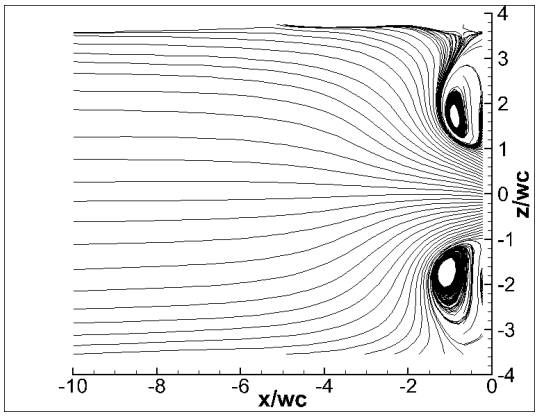

(a)

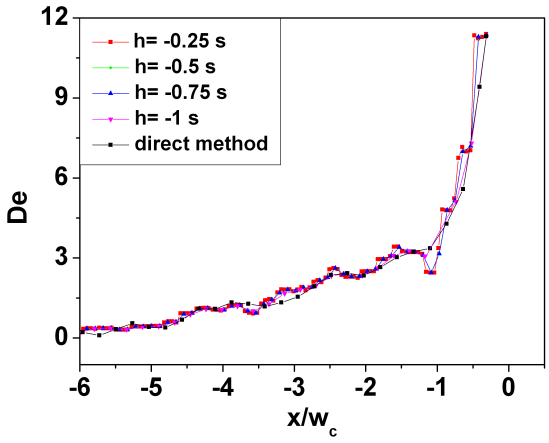

(b)

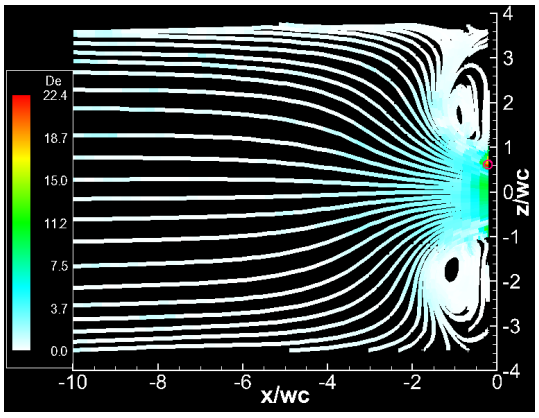

(c)

Figure 6.2: (a) an ensemble-averaged velocity field from the $El = 60.8$, $Wi = 35.3$ flow of a $16.6\,c^*$ PAAm solution, through an $8:1$ contraction (see Chapter 5).(b) Effect of changing the integration step size on the local Deborah number measured along the red coloured streamline in (a).(c) The corresponding intensity pattern of De obtained with $h = -1$ s. The location of the maximum measured local Deborah number is circled in red.

Integration step size [s]	-0.25	-0.5	-0.75	-1	-1.5
De_{max}	24.6	23.7	23.7	22.4	22.5

Table 6.1: Effect of changing the integration step size on the maximum measured De relatively to the velocity vecor field in Fig. 6.2a.

6.4 Local deformations in $4:1$ planar contraction flow

Fig. 6.3 shows the velocity fields and the corresponding intensity patterns of the local Deborah number extracted for the $El = 25.5$ flow of the 16.6 c^* PAAm solution past through a 4:1 contraction geometry (the Flowcell 1) at nominal Weissenberg numbers Wi = 8.8, 22, 44.1 and 73.0, respectively. The points where the local Deborah number is maximum, $De = De_{max}$, are circled in red.

In the Newtonian flow regime, De_{max} is at the position $x = z = 0$ approximately. The stretch appears to be pronounced ($De > 1.6$) on the vicinity of contraction throat ($x/w_c \geq -0.8$, $-0.5 \leq z/w_c \leq 0.5$). When the corner vortices appear (at a $Wi_t \cong 22$), De_{max} moves to a point at $x/w_c = 0$, $z/w_c = 0.5$ approximately. At the transition to the corner vortex flow regime, $De_{max} = 21.7$. The position of De_{max} remains approximately the same with a further increase of Wi. At $Wi = 73$, De_{max} slightly moves up to the upstream region. In the corner vortex flow regime, the extensional stretch appears to be higher in the vicinity of the lip of the contraction ($x/w_c \cong 0, z/w_c \cong 0.5$), than within the contraction throat. Note that the analysis of Binding (1988) has already predicted that, for shear-thinning fluids flowing through a planar contraction, the maximum elongational rate occurs on the lips of contraction in the corner vortex flow regime. Moreover, the experimental data show that the De measured at $z/w_c = +0.5$ were always different from the De at $z/w_c = -0.5$ for all Wi in the corner vortex flow regime. The difference between the local Deborah numbers measured at the two lips of contraction ($x \cong 0, z/w_c = \pm 0.5$) is almost monotonically increasing with Wi, as it is shown in Fig. 6.5.

Fig. 6.4 shows the temporal evolution of De at $Wi = 73$. The position of De_{max} appear to be approximately in a stationary at $x/w_c = -0.2, z/w_c = 0.5$.

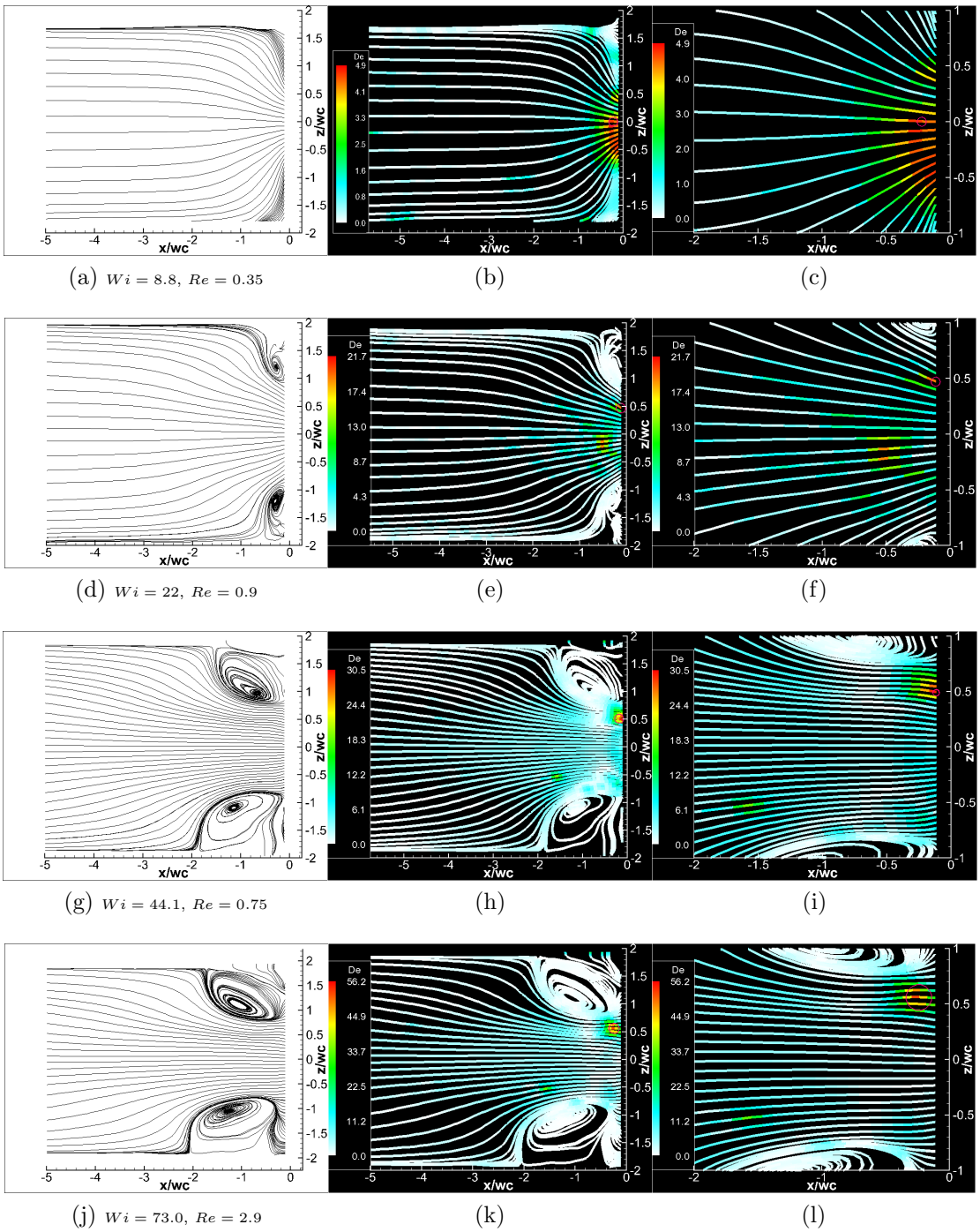

(a) $Wi = 8.8,\ Re = 0.35$ (b) (c)

(d) $Wi = 22,\ Re = 0.9$ (e) (f)

(g) $Wi = 44.1,\ Re = 0.75$ (h) (i)

(j) $Wi = 73.0,\ Re = 2.9$ (k) (l)

Figure 6.3: De fields for the El = 25.5 flow of the $16.6c^*$ PAAm solution past through a 4:1 contraction geometry (the Flowcell 1). The left column shows, from top to bottom, the ensemble-averaged velocity fields at flow rates $Q = 3, 7.5, 15$ and 25 ml/hr respectively. The corresponding intensity patterns of De are shown in the middle column. In the right column, the De fields have been magnified in the vicinity of the maximum measured De.

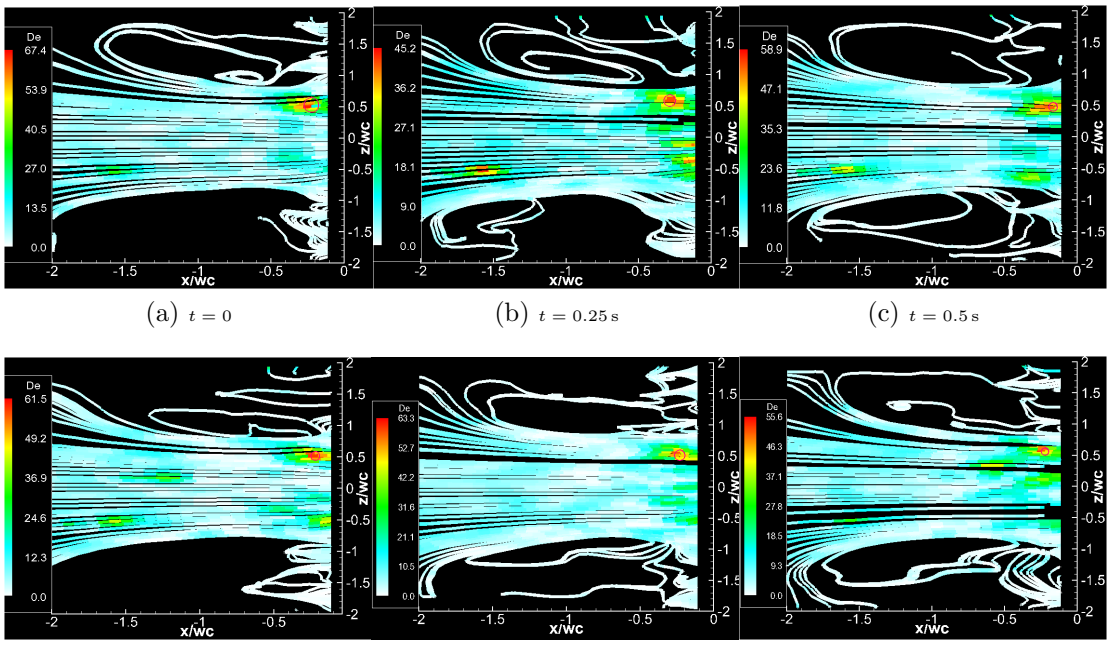

(a) $t = 0$ (b) $t = 0.25\,\mathrm{s}$ (c) $t = 0.5\,\mathrm{s}$

(d) $t = 0.75\,\mathrm{s}$ (e) $t = 1\,\mathrm{s}$ (f) $t = 1.25\,\mathrm{s}$

Figure 6.4: Snapshots of the De field at various instants t for the El = 25.5 flow of the 16.6c^* PAAm solution past through a 4:1 contraction geometry (the Flowcell 1) at $Q = 25$ ml/hr ($Wi = 73$).

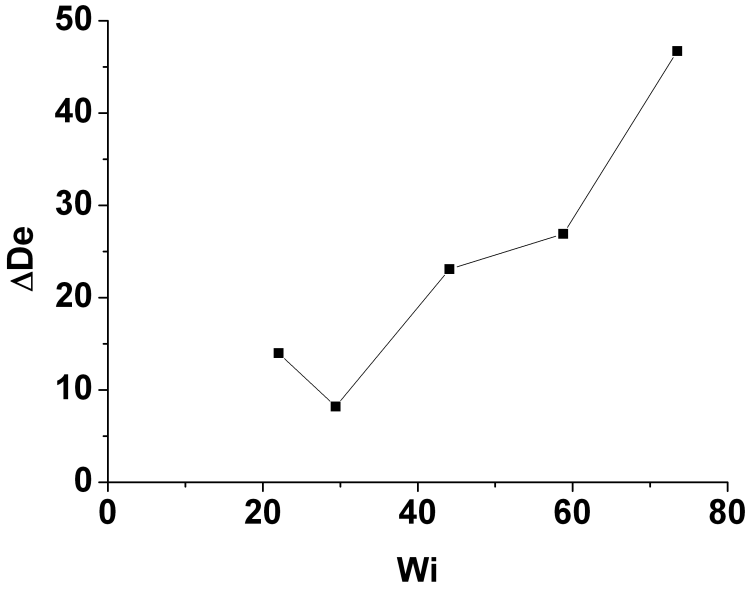

Figure 6.5: Difference between the local Deborah numbers measured at the two lips of contraction for $El = 25.5$ and $\beta = 4$.

6.5 Local deformations in $8:1$ planar contraction flow

Fig. 6.6 shows the velocity fields and the corresponding intensity patterns of the local Deborah number for the $El = 60.8$ flow of the $16.6\,c^*$ PAAm solution past through a 8:1 contraction geometry (the Flowcell 2) at nominal Weissenberg numbers $Wi = 5.9$, 17.6, 35.3 and 94.1, respectively.

In the Newtonian-like flow regime ($Wi = 5.9$), the region of considerable stretch ($De > 1$) is confined within an area $-1 \leq z/w_c \leq 1$, $-2 \leq x/w_c \leq 0$ in the vicinity of the contraction throat. The maximum De ($De_{max} \cong 4$) is located at a position ($x/w_c = 0$, $z/w_c \cong -0.25$). At $Wi = 17.6$, immediately before the transition to the lip vortex flow regime, the intensity of the stretch propagates toward the upstream along both the x and the z directions, while the position of De_{max} is not changed. At $Wi = 35.3$, within the lip vortex flow regime, the position of De_{max} moves towards a point with $z/w_c = 0.6$ in the vicinity of the lip vortex. At $Wi = 73.0$, within the time-dependent corner vortices flow regime, the position of De_{max} shifts toward the upstream of the flow.

Fig. 6.7 shows the snapshots of the De field at various instants at $Wi = 73$. Different from the $4:1$ contraction flow at a similar Weissenberg number, the position of De_{max} is located in the upstream region away from the contraction plane, and is much more time-dependent.

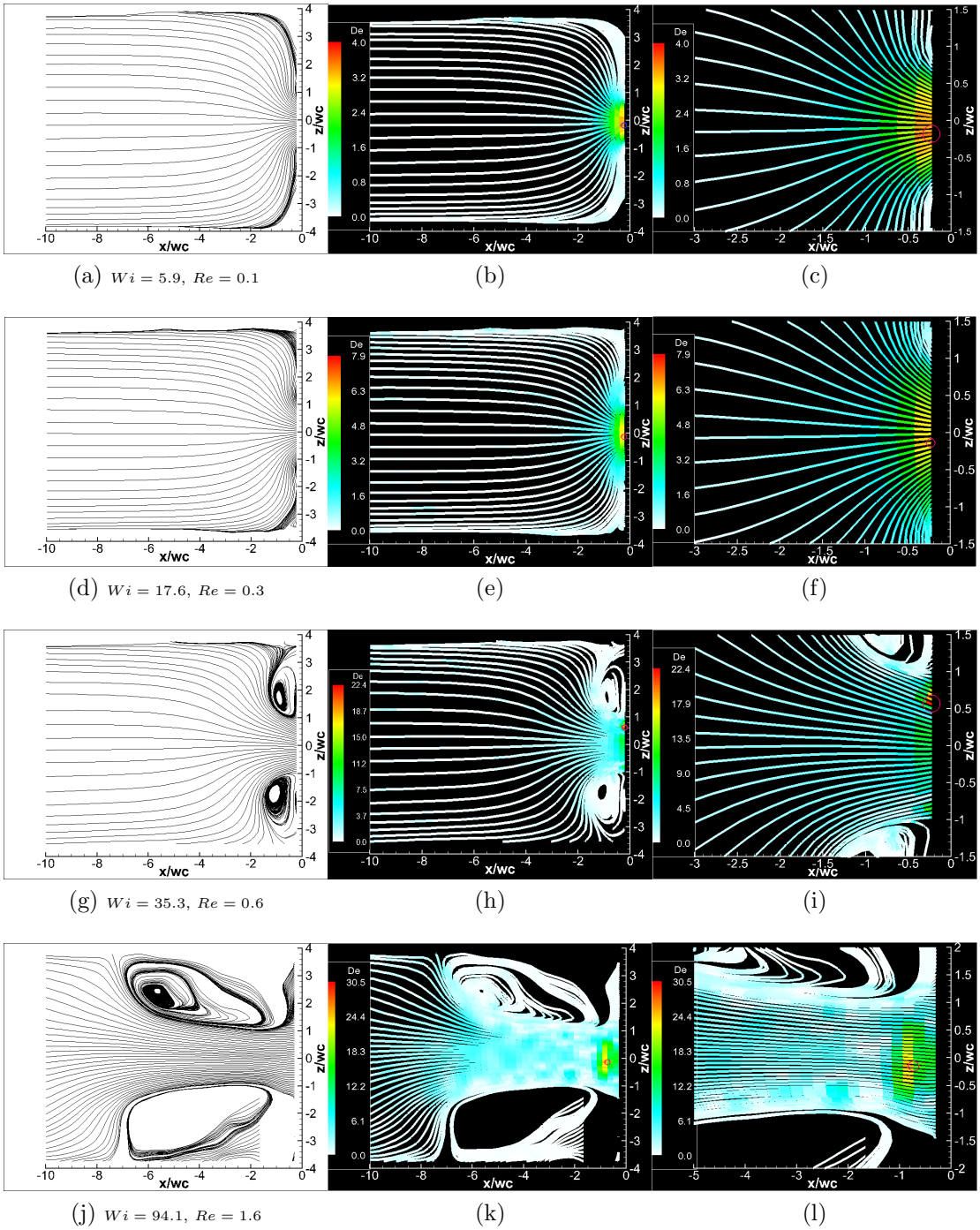

(a) $Wi = 5.9,\ Re = 0.1$ (b) (c)

(d) $Wi = 17.6,\ Re = 0.3$ (e) (f)

(g) $Wi = 35.3,\ Re = 0.6$ (h) (i)

(j) $Wi = 94.1,\ Re = 1.6$ (k) (l)

Figure 6.6: De fields for the El = 60.8 flow of the $16.6c^*$ PAAm solution through the Flowcell 2 ($\beta = 8$). The left column shows, from top to bottom, the velocity fields at flow rates $Q = 0.5$ ml/hr (ensemble-averaged), $Q = 1.5$ ml/hr (ensemble-averaged), $Q = 3$ ml/hr (ensemble-averaged) and $Q = 8$ ml/hr (instantaneous). The corresponding intensity patterns of De are shown in the middle column. In the right column, the De fields have been magnified in the vicinity of the maximum measured De.

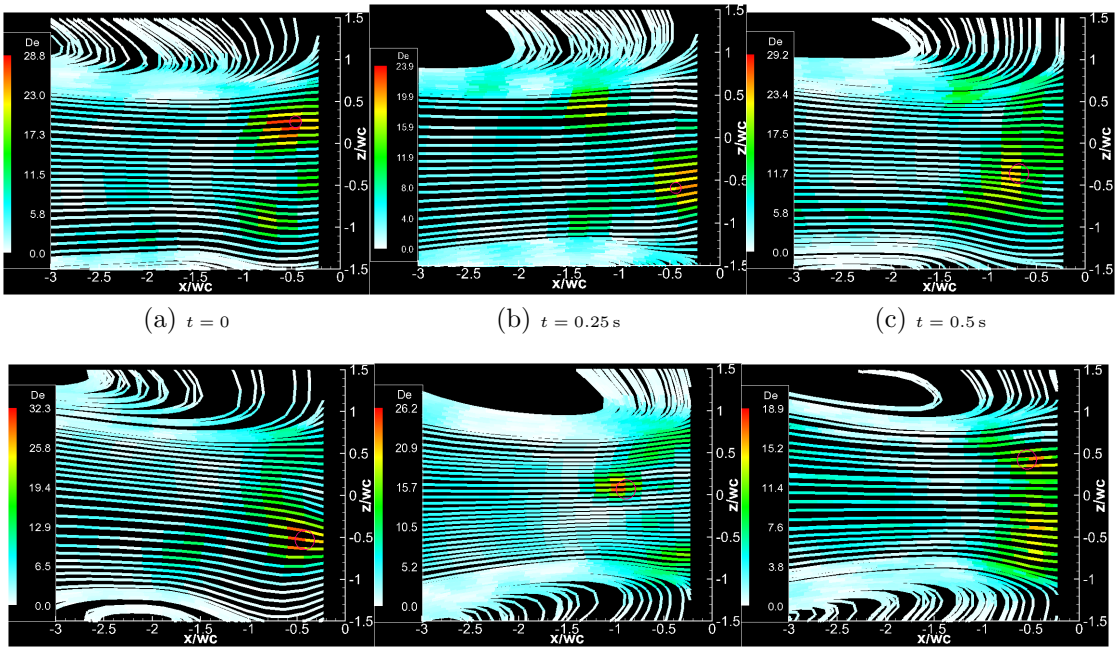

(a) $t = 0$ (b) $t = 0.25\,\mathrm{s}$ (c) $t = 0.5\,\mathrm{s}$

(d) $t = 0.75\,\mathrm{s}$ (e) $t = 1\,\mathrm{s}$ (f) $t = 1.25\,\mathrm{s}$

Figure 6.7: Snapshots of the De field at various instants t for the El = 60.8 flow of the 16.6c^* PAAm solution through the Flowcell 2 ($\beta = 8$) at $Q = 7$ ml/hr ($Wi = 73$).

6.5.1 Lateral profiles of the local Deborah number

The profiles of the local Deborah number along a line of $x/w_c = -0.4$, under different nominal Weissenberg numbers, $Wi = 5.9$ and 17.6 (within the Newtonian-like flow regime), and $Wi = 26.5$ (within the lip vortex flow regime) are presented in Fig. 6.8. The re-entrant corners of the contraction flow geometry are located at $z/w_c = \pm 0.5$, as indicated by the two solid lines. At $Wi = 5.9$, the stretch is pronounced ($De \cong 3$) for $|z/w_c| \leq 0.5$, thus within the width of the narrow channel. For $0.5 \leq |z/w_c| \leq 4$, De quickly decays to zero. At $Wi = 17.6$, immediately before the formation of lip vortices, the maximum De has increased, and its profile is much broader than the profile at $Wi = 5.9$. At $Wi = 26.5$, corresponding to the lip vortex flow regime, two local *maxima* in the De profile appear at $z/w_c = \pm 1$ approximately, in correspondence of the positions where the two vortices detach from the flow stream.

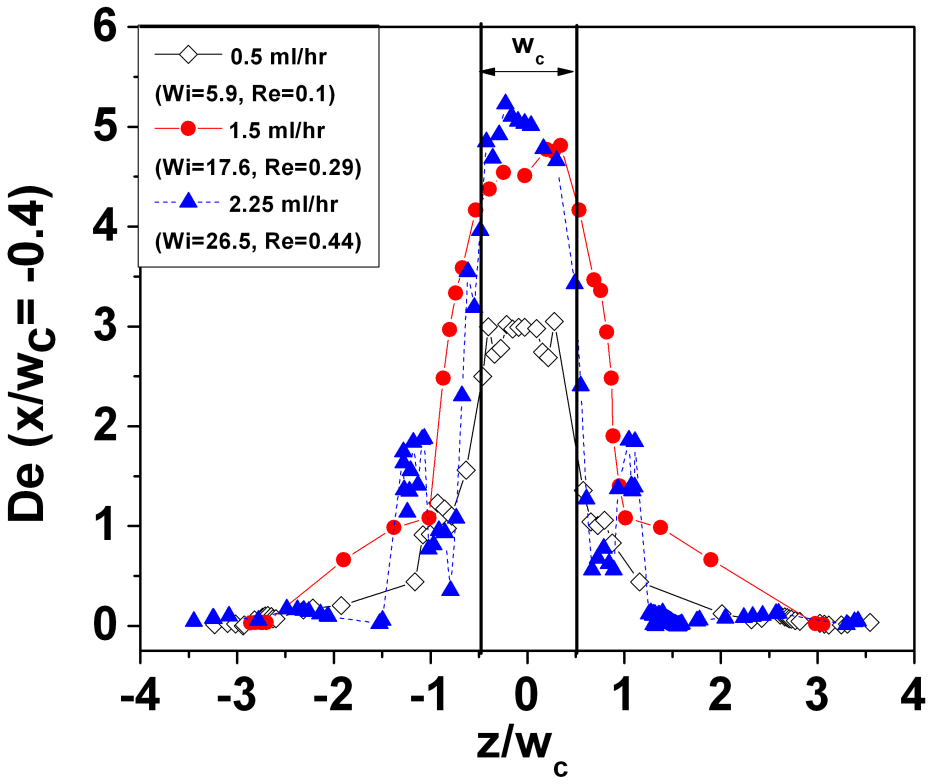

Figure 6.8: Lateral profiles of De at $x/w_c = -0.4$ for $\beta = 8, El = 60.8$ and $5.9 \leq Wi \leq 26.5$.

6.6 Local deformations in $16:1$ planar contraction flow

Fig. 6.6 shows the velocity fields and the corresponding intensity patterns of the local Deborah number for the $El = 476.8$ flow of the $16.6\,c^*$ PAAm solution past through a 16:1 contraction geometry (the Flowcell 3) at nominal Weissenberg numbers $Wi =$ 9.4, 18.8, 37.6 and 94.1, respectively.

At $Wi = 9.4$, corresponding to the Newtonian-like flow regime, the maximum of the local Deborah number ($De_{max} \cong 1.4$) is located at a position $x/w_c \cong 0, z/w_c \cong -0.4$ very close to the centre of the contraction plane. At $Wi = 18.8$, immediately before the onset of the single lip vortex flow regime, the intensity of stretch propagates towards the upstream region along x and z directions in a similar manner as in case of the 8:1 contraction, and the position of the maximum De shifts towards a point with $x/w_c \cong 0, z/w_c \cong 0.6$. Note that, when Wi is increased from

$Wi = 9.4$ to $Wi = 18.8$, the maximum measured local Deborah number decreases from $De_{max} = 1.4$ to $De_{max} = 0.6$. This could be explained by the fact that the flow field of the higher Wi is less symmetric than the one of the lower Wi, hence the flow prefers a configuration with less stretch of fluid elements. At $Wi = 37.6$, within the single corner vortex flow regime, the region where De is more pronounced is still close to the contraction plane. At $Wi = 94.1$, the onset of a time-dependent double corner vortex flow regime is reflected in the region of maximum stretch to shift upstream in the flow, similarly than what observed in case of the $8 : 1$ contraction in the high Wi flow regime.

As shown in Fig. 6.10, at $Wi = 94.1$ the position of the De_{max} is noteworthy changing in time. Note that, for this El and β, De_{max} appeared to be much lower than Wi for all the imposed flow conditions.

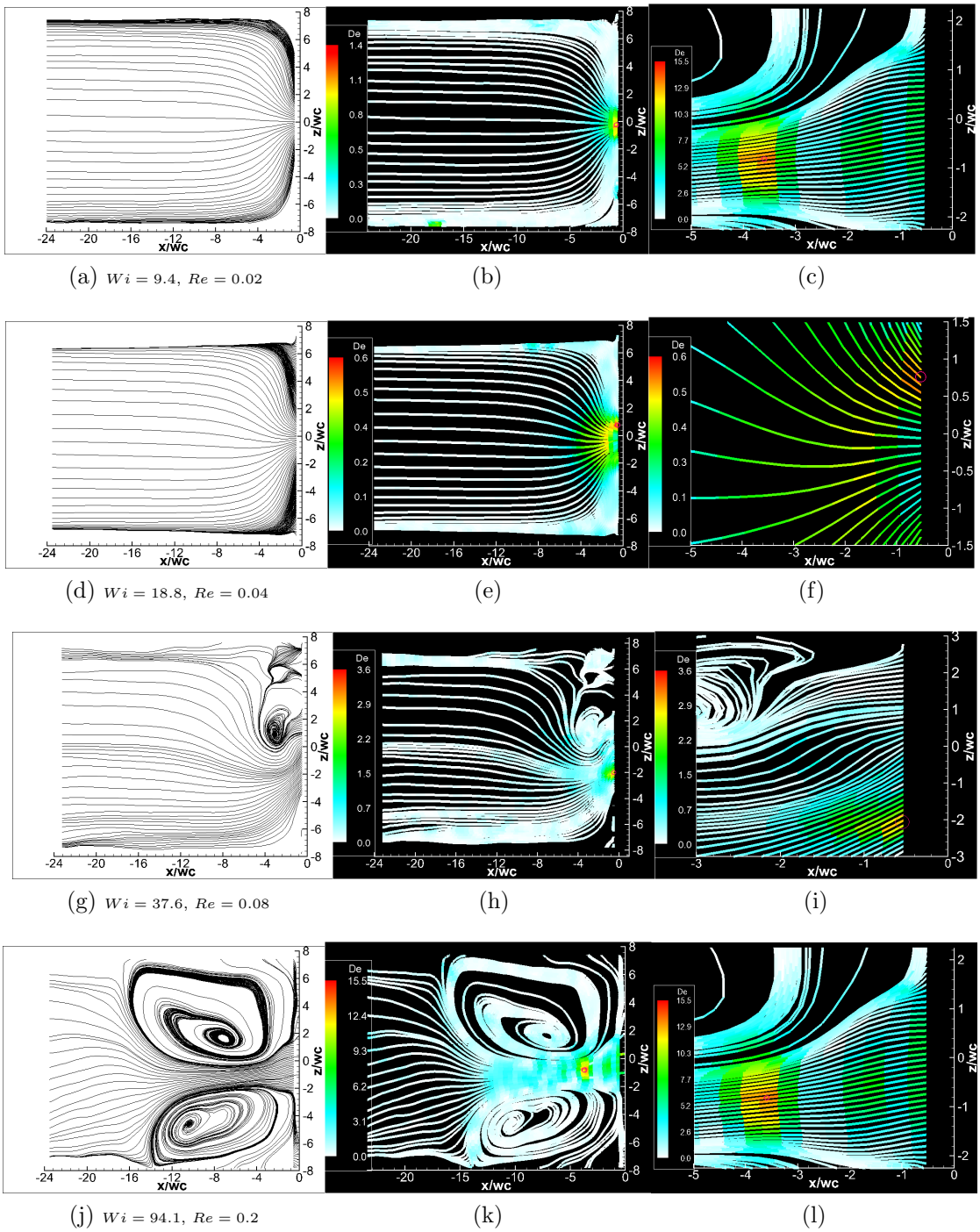

(a) $Wi = 9.4,\ Re = 0.02$ (b) (c)

(d) $Wi = 18.8,\ Re = 0.04$ (e) (f)

(g) $Wi = 37.6,\ Re = 0.08$ (h) (i)

(j) $Wi = 94.1,\ Re = 0.2$ (k) (l)

Figure 6.9: De fields for the El = 476.8 flow of the 16.6c^* PAAm solution through the Flowcell 3 ($\beta = 16$). The left column shows, from top to bottom, the velocity fields at flow rates $Q = 0.05$ ml/hr (ensemble-averaged), $Q = 0.1$ ml/hr (ensemble-averaged), $Q = 0.2$ ml/hr (instantaneous) and $Q = 0.5$ ml/hr (instantaneous). The corresponding intensity patterns of De are shown in the middle column. In the right column, the De fields have been magnified in the vicinity of the maximum measured De.

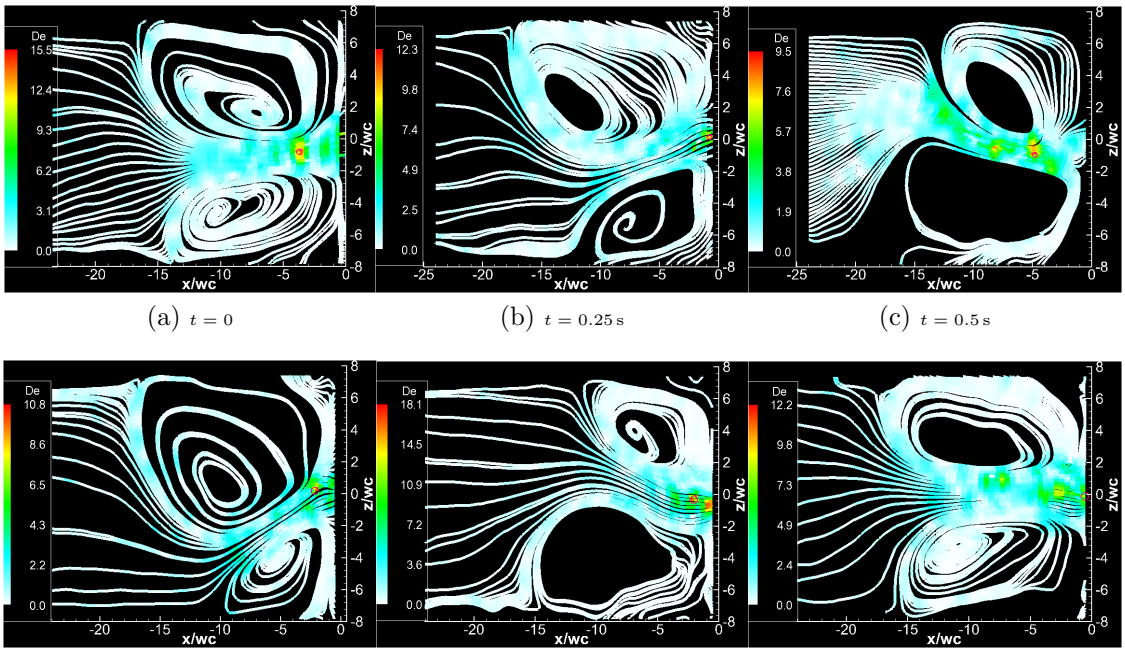

(a) $t = 0$ (b) $t = 0.25\,\mathrm{s}$ (c) $t = 0.5\,\mathrm{s}$

(d) $t = 0.75\,\mathrm{s}$ (e) $t = 1\,\mathrm{s}$ (f) $t = 1.25\,\mathrm{s}$

Figure 6.10: Snapshots of the De field at various instants t for the $El = 476.8$ flow of the $16.6c^*$ PAAm solution through the Flowcell 3 ($\beta = 16$) at $Q = 0.5$ ml/hr ($Wi = 94.1$).

6.6.1 Velocity profiles along the central streamline

As shown in Fig. 6.11, the streamline along the $x = 0$ axis in the fully developed upstream region ($x/w_c << -1$) is defined as the *central streamline* C. It is interesting to evaluate the velocity and extensional profile along the central streamline, especially for highly asymmetric patterns observed in the 16:1 contraction geometry. From its definition, C is positioned along the $x = 0$ axis if the flow is symmetric. If a given velocity vector $\underline{v}_a$ is located at a point $\underline{r}_a \in C$ ($\underline{r}_a$ is measured from the origin of the coordinate frames in Fig. 6.11), the path along C from $\underline{r}_a$ to the contraction plane is indicated as $\xi(\underline{r}_a)$ and is calculated as:

$$\xi(\underline{r}_a) = \sum_{\underline{r}_i = \underline{r}_0}^{\underline{r}_i = \underline{r}_a} \Delta\xi(\underline{r}_i) \tag{6.10}$$

where $\Delta\xi(\underline{r}_i)$ is the distance between two consecutive points along C and is computed as in Section 6.3.1, and $\underline{r}_0$ is the point of C which lies on the $x = 0$ plane.

Fig. 6.12 shows the profile of the dimensionless speed $v_\xi / < v_u >$ along the central streamline in the dimensionless contour distance ξ/w_c from the origin for

the $El = 476.8$ flow of the $16.6c^*$ PAAm solution through the $\beta = 16$ contraction geometry, over a range of nominal Weissenberg numbers $9.6 \leq Wi \leq 116.4$. The profile for the Newtonian fluid is plotted for a comparison. At $Wi = 9.4$, within the Newtonian-like flow regime, C lies on the $x = 0$ axis (see Fig. 6.11a), and the velocity profile of the polymer solution closely follows the profile of DI water all the way to the contraction. At $Wi = 56.4$, the presence of a single corner vortex reduces the fluid passage cross section in the vicinity of the contraction, and curves the central streamline (see Fig. 6.11b). As a consequence, the v_ξ profile starts to increase at $\xi/w_c \cong 15$ (where $x/w_c \cong -12$), and reaches a local maximum at $\xi/w_c = 6$ (or $x/w_c \cong -4$), where the vortex size along the z direction is also maximum. At $Wi = 116.4$, within the double corner vortex flow regime, the central streamline starts to deviate from the x axis at $x/w_c \cong -20$, and assumes an "S" shape on the vicinity of the contraction (see Fig. 6.11c). As a consequence, the velocity profile along C starts to deviate from the profile of DI water further upstream, at $\xi/w_c \cong 20$ (or $x/w_c \cong -19$). For the $Wi = 116.4$ flow, the local maximum in the velocity profile (reached at $\xi/w_c \cong 7.5$ or $x/w_c \cong -6$) is higher than the one observed for the $Wi = 56.4$ flow. This is due to the contemporaneous presence of two vortices, which causes a further reduction of the fluid passage cross section.

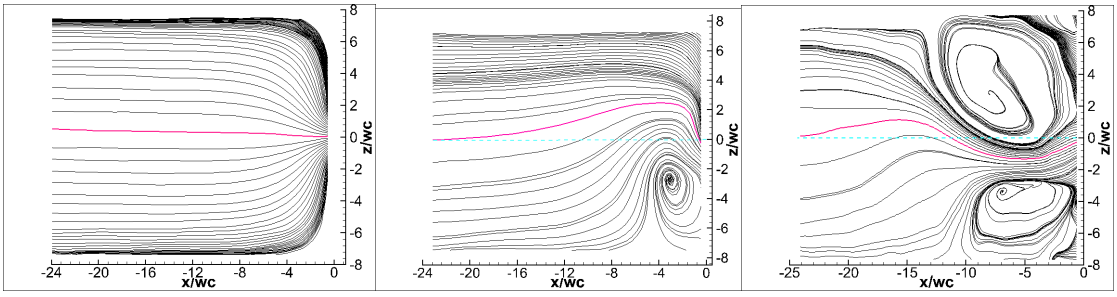

(a) $Wi = 9.4, Re = 0.02$ (b) $Wi = 56, Re = 0.12$ (c) $Wi = 116, Re = 0.24$

Figure 6.11: Central streamlines for the $El = 476.8$ flow of the $16.6c^*$ PAAm through the Flowcell 3 ($\beta = 16$). (a) $Q = 0.05$ ml/hr, ensemble-averaged velocity field; (b) $Q = 0.3$ ml/hr, instantaneous velocity field; (c) $Q = 0.6$ ml/hr, instantaneous velocity field.

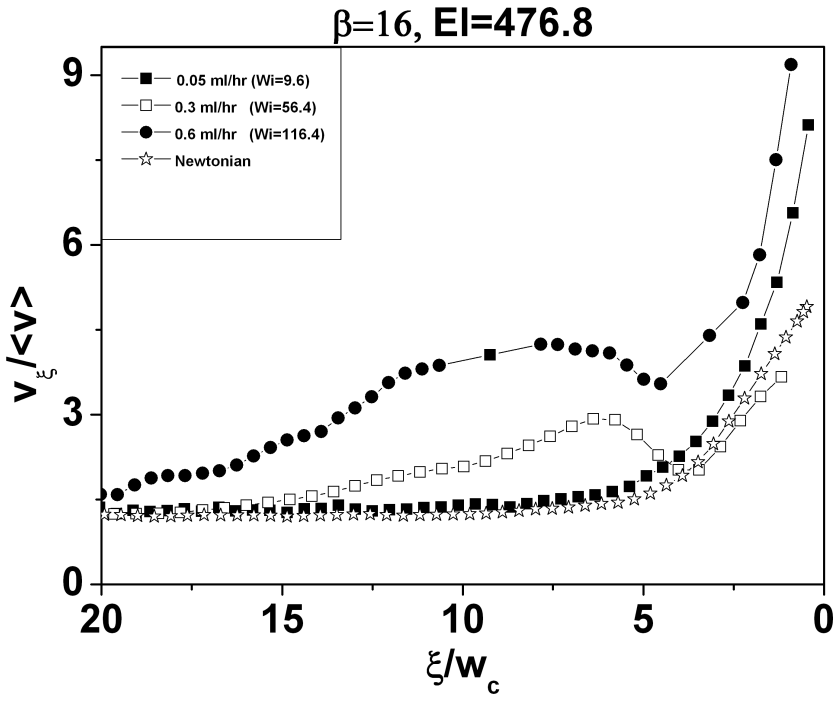

Figure 6.12: Velocity profiles along the central streamline plotted as a function of ξ for different Wi, for the $El = 476.8$ flow of the $16.6c^*$ PAAm solution through the Flowcell 3 ($\beta = 16$).

6.7 The De-Wi diagrams

As discussed in Section 2.4, the characteristic dimensionless numbers in characterisation of nonlinear complex viscoelastic fluid flows are usually defined in a quite arbitrary way. For exemple, in the definition of the nominal Weissenberg number used for studying the flows through a sudden contraction, the characteristic rate of deformation experienced by the fluid is taken as the nominal shear rate in downstream narrow channel $\dot{\gamma}_d$. However neither $\dot{\gamma}_d$ nor the nominal upstream shear rate $\dot{\gamma}_u$ can truly represent the distribution of the deformation rate effectively experienced by the fluid. The local Deborah number can be used to assess the appropriateness of the definition of the nominal Weissenberg number.

In Fig. 6.13 and Fig. 6.14, the maximum local Deborah number De_{max} is plotted as a function of the Weissenberg number defined by either upstream or downstream conditions, $Wi_u = \lambda\frac{2<v_u>}{w_u}$ or $Wi_d = \lambda\frac{2<v_d>}{w_d}$. Every De_{max} point in the diagram was obtained by averaging the De_{max} estimated from instantaneous intensity patterns of De at five consecutive instant. The straight lines $De_{max} = Wi_u$ and $De_{max} = Wi_d$

are also plotted. Fig. 6.13 shows $De_{max} > Wi_u$ for all flow rates. Fig. 6.14 shows that, for the flow of $El = 25.5$ and $\beta = 4$, De_{max} is close to Wi_d in relatively low flow rate ($Wi_d \leq 50$). At higher Wi_d, De_{max} becomes smaller than Wi_d, and has a bigger standard deviation. For the 8:1 contraction flows with $El = 14.8$ and $El = 60.8$, the condition $Wi_d \cong De_{max}$ is attained in low flow rate regime ($Wi_d \leq 25$), which approximately correspond to the Newtonian-like and symmetric lip vortices flow structures. At higher Wi, the flow becomes highly time-dependent and the local Deborah number becomes systematically lower than Wi_d. Finally, for the 16:1 contraction flows, which exhibit noteworthy asymmetric flow structures at almost all flow rates, De_{max} is much lower than Wi_d for all the range of Wi_d.

Thus, the Weissenberg number defined by means of the downstream flow conditions is effectively close to the true deformation rate experienced by the fluid only in such cases where the flow field is symmetric and stable (that is, in the Newtonian-like flow regime for $\beta = 4$ and 8 or where symmetric corner or lip vortices flow structures are observed). For highly asymmetric and/or unstable flows, the effectiveness of stretch is reduced and De_{max} becomes lower than Wi_d. Therefore, the convention commonly used in the literature does not reflect the true deformation rate experienced by the fluid, especially in the high Wi_d region. It greatly over estimates the stretch experienced by polymers. The true degree of the stretch, characterized by De, is comprised between Wi_u and Wi_d for all the flow geometries and the imposed El and flow rates.

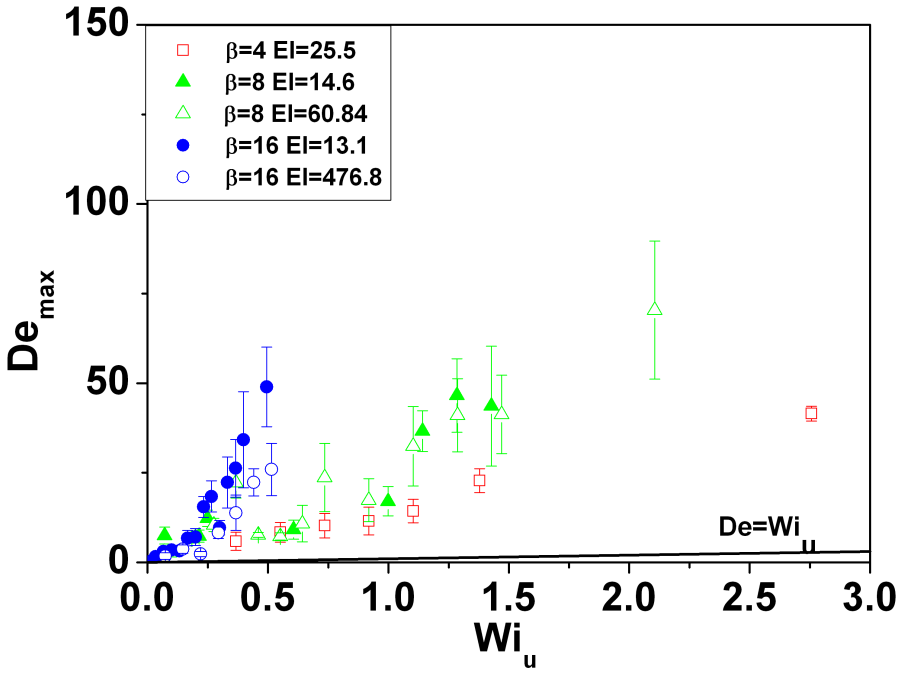

Figure 6.13: De_{max} plotted as a function of the Weissenberg number defined by means of upstream width, $Wi_u = \lambda \frac{2<v_u>}{w_u}$.

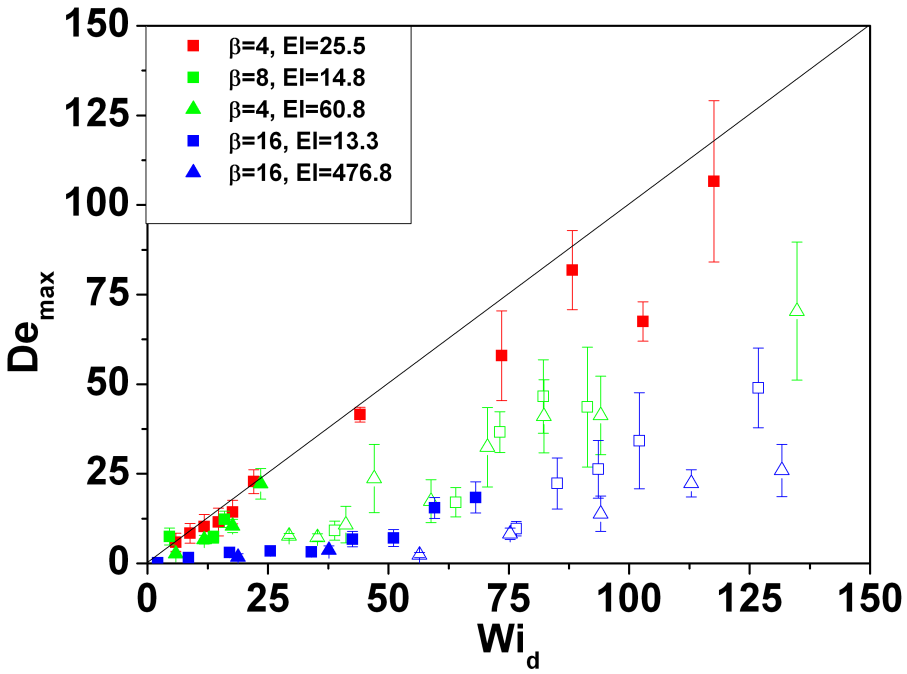

Figure 6.14: De_{max} plotted as a function of the nominal Weissenberg number defined by means of downstream width, $Wi_d = \lambda \frac{2<v_d>}{w_d}$. Filled symbols refer to those flow structures which appear stable. Empty symbols refer to flow structures with a time-dependent behaviour.

Chapter 7

Conclusions and Recommendations

7.1 Conclusions

The aim of this research has been to quantitatively study the high Weissenberg number, moderate Reynolds number flow regime of well-characterized polyacrylamide aqueous solutions through several microfluidic geometries.

A systematic approach was adopted. Molecular analysis was performed by gel permeation chromatography, and a full rheometric characterisation was carried out by various techniques, such as the ARES rotational rheometer equipped with double-wall Couette geometry, the Vilastic-3 analyzer, the piezoelastic axial vibrator (PAV), the capillary-force-driven rheometer (CaBER) and a novel microfluidic device. Quantitative flow measurements in micro-fabricated devices were carried out by a $\mu - PIV$ system and *in situ* pressure measurements.

The GPC analysis revealed the very high polydispersity of the PAAm sample. The semi-dilute PAAm solutions, with the nearly same weight averaged molecular weight as the PEO(I) studied in Li et al. (2011) but much higher polydispersity index, show significantly different nonlinear fluid dynamics in the contraction flow, especially with $\beta = 8$ and 16. The nonlinear steady shear viscosities were measured (with the minimum inertial effects) at a shear rate at least two orders of magnitude higher than those measured by most commercial rheometers. The relaxation

spectrum for the $16.6c^*$ PAAm solution was extracted from G' and G" data over a wide frequency range up to 6650 Hz. A single relaxation time, as measured using a CaBER, is not sufficient to quantify the flow behaviour of polydisperse polymer solutions with a wide span of relaxation times.

Quantitative measurements of velocity fields and pressure drops in microscopic planar contraction geometries were carried out for various Elasticity numbers ($13.3 \leq El \leq 476.8$) and three different contraction ratios ($\beta = 4,\ 8$ and 16), in order to compare the effect of varying fluid properties with that of changing geometry in a range of Weissenberg numbers $1.4 \leq Wi \leq 131.7$.

In case of the $El = 25.5$ flow of the $16.6c^*$ PAAm solution through the $\beta = 4$ contraction geometry, symmetric and stable corner vortices were found over a range of Weissenberg numbers $22.0 \leq Wi \leq 88.2$. This is in agreement with the observations of Evans and Walters (1986), (1989) for aqueous polyacrylamide solutions through macroscopic 4:1 planar contractions, and of Gulati et al. (2008) for an high El flow of a DNA solution through a $\beta = 2$ contraction geometry. The presence of symmetric corner vortices for the $\beta = 4$ contraction flow has also been numerically predicted for either two and three-dimensional viscoelastic flows (Alves et al., 2004; Xue et al., 1998). Note also that the vortex growth phenomena here observed for a $\beta = 4$ contraction flow with a very shallow aspect ratio are different from what reported by Rothstein and McKinley (1999) for the flow of a dilute polystyrene solution through an axisymmetric $\beta = 4$ macro-scale geometry. Rothstein and McKinley observed symmetric and stable corner vortices only at a low Weissenberg number, the recirculation regions then becoming asymmetric and time-dependent at higher Wi. As pointed out by Rodd et al. (2005a), the different vortex growth mechanisms observed in axial and planar contraction flows with a same contaction ratio could depend on the different Hencky strains between the two geometries ($\varepsilon_H = \ln \beta$ and $\varepsilon_H = 2 \ln \beta$ for planar and circular contraction flows respectively).

For both $El = 14.8$ and $El = 60.8$ flows through a $\beta = 8$ contraction, lip vortices were observed over a range of Weissenberg numbers $13.7 \leq Wi \leq 40$. At $Wi = 40$, these structures are transformed into much larger and unsteady corner vortices, and

their size depends much more strongly on Wi. The minimum Weissenberg number for the onset of elastic flow structures is much lower than what reported by Li et al. (2011) for the flow of aqueous solutions of a less polydisperse PEO sample through a nearly identical $8:1$ contraction geometry. The results reported here are much different from the observations of Nigen and Walters (2002), which did not report the formation of elastic vortex structures for 2D flows of PAAm solutions through an $8:1$ macro-fabricated contraction. The vortex formation mechanism reported here is also in contrast with the simulations of Alves et al. (2004) for a PTT fluid through a two-dimensional $\beta = 8$ contraction. The three dimensional simulations of Omowunmi and Yuan (2010) of the PTT fluid in $\beta = 8$ contraction flow of the PTT fluid are the only available computational work to predict some of the flow phenomena observed here, such as the formation of lip vortices at low Wi and their growth into larger corner vortices as Wi is increased . Note also that Afonso et al. (2006) have predicted some of the flow phenomena observed in $\beta = 8$ contraction flow, such as the formation of time-dependent corner vortices and the coexistence of two vortices on a same side of the flow channel. However, because of the very different flow geometries ($\beta = 8$ and $\alpha = 47/800$ here, $\beta = 4$ and 2D flow in the work of Afonso et al.), it is not possible to have any meaningful comparison with the results of present work.

In case of the $El = 13.3$ and 476.8 flows through a $\beta = 16$ contraction, very different flow patterns from those of lower contraction ratio flows were observed. A single lip vortex was found in a window of Wi ($34 \leq Wi \leq 56$). Such flow structure was observed to grow in a much larger, single corner vortex with an increase of Wi. At $Wi = 75$ a secondary corner vortex is formed, and its size eventually reaches the size of the primary vortex with a further increase of Wi. The minimum Weissenberg number at which the vortex structures occurred was found to be much lower than the one reported by Rodd et al. (2005a, 2007) for PEO aqueous solutions through a $16:1$ micro-contraction with a much shorter downstream narrow channel than the one used in the present work. Again, the asymmetric vortex structures reported here are completely different from the simulations for the flow of a PTT fluid through a

2D, $\beta = 16$ contraction of Alves et al. (2004).

The effect of changing the polymer concentration (thus the Elasticity number) on the observed flow patterns was investigated for both the $\beta = 8$ and $\beta = 16$ contraction flows.

In case of the $\beta = 8$ contraction geometry, it was observed that increasing El from 14.8 to 60.8 has the effect of stabilizing the observed flow structures, while their size and location remain essentially unchanged. This agrees with previous observations in both microscale (Li et al., 2011) and macroscale (Haward et al., 2010a) flow geometries. On the other hand, in case of the $\beta = 16$ contraction geometry, the increase of El (from $El = 13.3$ to $El = 476.8$) makes the elastic flow structures more time-dependent in a range of Wi ($35 \leq Wi \leq 75$). It contrasts with previous observations in a similar $16 : 1 : 16$ micro-contraction geometry (Rodd et al., 2005a, 2007). Therefore, it was found that changing the Elasticity number in a fixed flow geometry can either increase or decrease the stability of observed flow patterns, depending on Elasticity number. These results suggest that increasing the Reynolds number at a fixed value of the Weissenberg number can either stabilize or make more unstable the flow, in a contrast with the previous experimental works.

The vortex growth mechanisms presented in this work are comparable with those reported by Chiba et al. (1990) for the flow of aqueous PAAm solutions with a larger zero-shear viscosity through macro-fabricated contraction geometries with $3.4 \leq \beta \leq 10$. This could be due to the similar ranges of Elasticity number explored ($13.3 \leq El \leq 476.8$ here, $3 \leq El \leq 600$ in the work of Chiba et al.). This observation suggests that any comparison between microscopic and macroscopic viscoelastic entry flows should be carried out at a close value of the Elasticity number.

The excess pressure drop across the contraction-expansion geometry is a very sensitive quantity to characterize non-linear flows of PAAm solutions. Several regimes were clearly identified from the excess pressure drop curves for two El number flows through $8 : 1 : 8$ and $16 : 1 : 16$ contraction geometries respectively, and were correlated with the size of upstream vortices visualized by $\mu - PIV$.

The results here presented are complementary to what shown in previous works

of Rodd et al. (2005a, 2007); Gulati et al. (2008); Rodd et al. (2010); Li et al. (2011), and clearly demonstrate that the complexity of nonlinear dynamics in contraction flows cannot be completely described by Weissenberg and Elasticity numbers, as the details of molecular weight and molecular weight distribution of polymer, and the geometric parameters (like the contraction and aspect ratios, or the length of downstream channel) will also greatly affect the nonlinear flow behaviour. Thus, a fully quantitative approach ranging from molecular characterisation to rheometric and velocity measurements has been proved to be necessary for better understanding of nonlinear dynamics of polymers in complex flows.

A numerical method was proposed to evaluate local elongational rates for an arbitral shape of the streamtraces, leading to the definition of a "local Deborah number" (De) field. It allowed for coupling the velocity fields in complex flow with the corresponding intensity patterns of polymer chains being stretched away from equilibrium, thus to extract a notable amount of information from PIV measurements in microfluidics.

The formation of vortex structures was found to be correlatable with a propagation of the stretch experienced by the polymer chains in the vicinity of the contraction throat towards the upstream region. This has been observed, e.g., in the case of both the $\beta = 8$, $El = 60.8$ and $\beta = 16$, $El = 476.8$ flows, just before the transition from Newtonian-like to lip vortex flow regime. The position of the maximum De across the entire flow domain was found to be very sensitive to the vortex flow regimes. The values of De_{max} were used to critically evaluate the validity of the definition of the nominal Weissenberg number largely adopted in the literature in the study of contraction flows. It was found that the nominal Wi, defined by means of the nominal shear rate in the fully developed region of the downstream channel, is effectively a measure of the true stretch experienced by the fluid only for symmetric and stable flow patterns. If the flow is asymmetric and/or time-dependent, De_{max} can be up to one order of magnitude lower than the nominal Weissenberg number, so that the definition of the nominal Wi loses validity.

The analysis method presented here also allowed for correlating the velocity

profiles extracted along the streamlines with the nonlinear flow regimes also in the case of highly asymmetric flow structures, such as those observed in case of the flows through a $16:1$ contraction geometry.

7.2 Recommendations for future work

The work carried out in this thesis opens a wide avenue for future research.

The relaxation spectrum obtained in Section 4.3 for an $8.3c^*$ PAAm solution is a more accurate rheological measure of polymer molecular weight distribution than the single CaBER relaxation time. Thus, it is necessary to establish and evaluate an appropriate average method, which would lead to a more precise definition of the dimensionless parameters characterizing the contraction flow experiments.

The principle of the microfluidic rheometer presented in Section 3.4 and 4.4 could be applied to the study of oscillatory flows. To do this, the syringe pump used in this work could be replaced by a pulsatile device, like a piezo-electric pump. Due to the small cross section area of the microfluidic channels, an oscillatory flow rate of even a few ml/hr could result in a very large imposed strain, making such a device ideal for studying the behaviour of complex fluids under Large Amplitude Oscillatory Shear (LAOS) flows. Although LAOS flows are important for gaining a fundamental understanding of the rheology of complex fluids, and can also be found in several natural or industrial processes, they are still poorly understood (Collyer and Clegg, 1998; Ewoldt et al., 2007).

As it has been shown in Chapter 5, the flows of PAAm solutions through microfluidic planar contraction geometries with $\beta = 8$ and 16 can be time-dependent and three-dimensional in the high Weissenberg flow regime, and two vortices on a same side of the contraction can even coexist for a short time interval. In order to determine whether such flows are chaotic or not, a further analysis of my experimental data is needed.

The analysis method proposed in Chapter 6 allows for obtaining a snapshot of the local stretch field underwent by polymer chains from PIV-generated, two-dimensional velocity vector fields. The quantitative information obtained by means

of such technique should be coupled with the predictions arising from constitutive models, so that the local extensional stress field related to non-linear dynamics in complex flows could be evaluated.

In order to obtain more systematic information, the method should be completed so that the full local rate of deformation tensor could be computed from the experimental data. This would be possible only if three-dimensional velocity measurements, such as those obtained by confocal micro-PIV (see Kinoshita et al. (2006b,a)), were made available.

The characterisation platform developed in this work could be used for a quantitative study of the flow of polymer solutions through other microfluidic flow geometries of fundamental interest. The stagnation point devices, like the "cross-slots", are of great relevance for studying the dynamics of polymer solutions under extensional flow conditions, see Arratia et al. (2006) and Haward et al. (2010b).

Bibliography

A.M. Afonso, P.J. Oliveira, F.T. Pinho, and M.A. Alves. Dynamics of high-deborah-number entry flows: a numerical study. *Journal of Fluid Mechanics*, 1:1, 2006.

M.A. Alves, P.J. Oliveira, and F.T. Pinho. On the effect of contraction ratio in viscoelastic flow through abrupt contractions. *Journal of Non-Newtonian Fluid Mechanics*, 122:117, 2004.

S.L. Anna and G.H. McKinley. Elasto-capillary thinning and breakup of model elastic liquids. *Journal of Rheology*, 45:115, 2001.

S.L. Anna, G.H. McKinley, D.A. Nguyen, T. Sridhar, S.J. Muller, J. Huang, and D.F. James. An interlaboratory comparison of measurements from filament-stretching rheometers using common test fluids. *Journal of Rheology*, 45:83, 2001.

P.E. Arratia, C.C. Thomas, J. Diorio, and J.P. Gollub. Elastic instabilities of polymer solutions in cross-channel flow. *Physical Review Letters*, 96:144502, 2006.

M. Baumgaertel and H.H. Winter. Determination of discrete relaxation and retardation time spectra from dynamic mechanical data. *Rheologica Acta*, 28:511, 1989.

A.V. Bazilevsky, V.M. Entov, and A.N. Rozhkov. Liquid filament rheometer and some of its applications. *Rheological Measurement*, page 41, 1988.

D.M. Binding. An approximate analysis for contraction and converging flows. *Journal of Non-Newtonian Fluid Mechanics*, 27:173, 1988.

R.B. Bird, W.E. Stewart, E.N. Lightfoot, et al. *Transport phenomena*. Wiley New York, 2007.

M. Bohdaneckỳ, V. Petrus, and B. Sedláček. Estimation of the characteristic ratio of polyacrylamide in water and in a mixed theta-solvent. *Die Makromolekulare Chemie*, 184:2061, 1983.

W. Chang, D. Tzebotich, L.P. Lee, and D. Liepmann. Blood flow in simple microchannels. In *Microtechnologies in Medicine and Biology, 1st Annual International, Conference On. 2000*, page 311. IEEE, 2002.

K. Chiba, T. Sakatani, and K. Nakamura. Anomalous flow patterns in viscoelastic entry flow through a planar contraction. *Journal of Non-Newtonian Fluid Mechanics*, 36:193, 1990.

C. Clasen, J.P. Plog, W.M. Kulicke, M. Owens, C. Macosko, L.E. Scriven, M. Verani, and G.H. McKinley. How dilute are dilute solutions in extensional flows? *Journal of Rheology*, 50:849, 2006.

A.A. Collyer and D.W. Clegg. *Rheological measurement*. Springer, 1998.

R.W. Connelly and J. Greener. High-shear viscometry with a rotational parallel-disk device. *Journal of Rheology*, 29:209, 1985.

J.J. Cooper-White, J.E. Fagan, V. Tirtaatmadja, D.R. Lester, and D.V. Boger. Drop formation dynamics of constant low-viscosity, elastic fluids. *Journal of Non-Newtonian Fluid Mechanics*, 106:29, 2002.

J.J. Crassous, R. Regisser, M. Ballauff, and N. Willenbacher. Characterization of the viscoelastic behavior of complex fluids using the piezoelastic axial vibrator. *Journal of Rheology*, 49:851, 2005.

B.J. de Gans, P.C. Duineveld, and U.S. Schubert. Inkjet printing of polymers: state of the art and future developments. *Advanced Materials*, 16:203, 2004.

PG de Gennes. Coil-stretch transition of dilute flexible polymers under ultrahigh velocity gradients. *Journal of Chemical Physics*, pages 5030–5042, 1974.

P.G. de Gennes. *Scaling concepts in polymer physics*. Cornell University Press, 1979.

A.J. Demello. Control and detection of chemical reactions in microfluidic systems. *Nature*, 442:394, 2006.

MM Denn and KC Porteous. Elastic effects in flow of viscoelastic liquids. *The Chemical Engineering Journal*, 2:280, 1971.

M. Doi and S.F. Edwards. *The theory of polymer dynamics*. Oxford University Press, 1988.

V.M. Entov and E.J. Hinch. Effect of a spectrum of relaxation times on the capillary thinning of a filament of elastic liquid. *Journal of Non-Newtonian Fluid Mechanics*, 72:31, 1997.

R.E. Evans and K. Walters. Flow characteristics associated with abrupt changes in geometry in the case of highly elastic liquids. *Journal of Non-Newtonian Fluid Mechanics*, 20:11, 1986.

R.E. Evans and K. Walters. Further remarks on the lip-vortex mechanism of vortex enhancement in planar-contraction flows. *Journal of Non-Newtonian Fluid Mechanics*, 32:95, 1989.

R.H. Ewoldt, C. Clasen, A.E. Hosoi, and G.H. McKinley. Rheological fingerprinting of gastropod pedal mucus and synthetic complex fluids for biomimicking adhesive locomotion. *Soft Matter*, 3:634, 2007.

J.J. Finnigan. A streamline coordinate system for distorted two-dimensional shear flows. *Journal of Fluid Mechanics*, 130:241, 1983.

K. Foster and G.A. Parker. The role of pure fluidic devices in machine tool applications. *Production Engineer*, 48:169, 1969.

J. François, T. Schwartz, and G. Weill. Crossover from the theta to the Excluded Volume Single Chain Statistics: New Experimental Evidences and a Modified Blob Model. *Macromolecules*, 13:564, 1980.

A. Groisman, M. Enzelberger, and S.R. Quake. Microfluidic memory and control devices, 2003.

S. Gulati, S.J. Muller, and D. Liepmann. Direct measurements of viscoelastic flows of DNA in a 2: 1 abrupt planar micro-contraction. *Journal of Non-Newtonian Fluid Mechanics*, 155:51, 2008.

D.C. Harris. *Quantitative chemical analysis*. WH Freeman, 2003.

S.J. Haward, Z. Li, D. Lighter, B. Thomas, J.A. Odell, and X.F. Yuan. Flow of dilute to semi-dilute polystyrene solutions through a benchmark 8: 1 planar abrupt micro-contraction. *Journal of Non-Newtonian Fluid Mechanics (in press)*, 2010a.

S.J. Haward, J.A. Odell, Z. Li, and X.F. Yuan. Extensional rheology of dilute polymer solutions in oscillatory cross-slot flow: the transient behaviour of birefringent strands. *Rheologica Acta*, 49:633, 2010b.

C.-H. Huang. *Rheological Characterisation of Complex Fluids*. MSc Thesis, the University of Manchester, 2010.

D.M. Jones and K. Walters. The behaviour of polymer solutions in extension-dominated flows, with applications to enhanced oil recovery. *Rheologica Acta*, 28: 482, 1989.

K. Kang, L.J. Lee, and K.W. Koelling. High shear microfluidics and its application in rheological measurement. *Experiments in Fluids*, 38:222, 2005.

A. Keller and J.A. Odell. The extensibility of macromolecules in solution; a new focus for macromolecular science. *Colloid & Polymer Science*, 263:181, 1985.

H. Kinoshita, S. Kaneda, T. Fujii, and M. Oshima. Three-dimensional measurement and visualization of internal flow of a moving droplet using confocal micro-PIV. *Lab on a Chip*, 7:338, 2006a.

H. Kinoshita, M. Oshima, S. Kaneda, and T. Fujii. Validation of confocal micro-PIV technique by Poiseuille flow measurement. In *Microtechnologies in Medicine and Biology, 2006 International Conference on*, page 78, 2006b.

L. Kirschenmann and W. Pechhold. Piezoelectric Rotary Vibrator (PRV)-a new oscillating rheometer for linear viscoelasticity. *Rheologica Acta*, 41:362, 2002.

W.M. Kulicke and RS Porter. Relation between steady shear flow and dynamic rheology. *Rheologica Acta*, 19:601, 1980.

R.G. Larson. Instabilities in viscoelastic flows. *Rheologica Acta*, 31:213, 1992.

R.G. Larson. The structure and rheology of complex fluids. *New York: Oxford*, 2001.

R.G. Larson. The rheology of dilute solutions of flexible polymers: Progress and problems. *Journal of Rheology*, 49:1, 2005.

R.G. Larson and J.J. Magda. Coil-stretch transitions in mixed shear and extensional flows of dilute polymer solutions. *Macromolecules*, 22:3004, 1989.

Z. Li, X.-F. Yuan, S. J. Haward, J. A. Odell, and S. Yeates. Non-linear dynamics of semi-dilute polymer solutions in microfluidics: a study of a benchmark flow problem. *Journal of non-Newtonian flow mechanics (accepted for publication)*, 2011.

R.F. Liang and M.R. Mackley. Rheological characterization of the time and strain dependence for polyisobutylene solutions. *Journal of non-newtonian fluid mechanics*, 52:387, 1994.

Y. Liu, Y. Jun, and V. Steinberg. Concentration dependence of the longest relaxation times of dilute and semi-dilute polymer solutions. *Journal of Rheology*, 53:1069, 2009.

X.L. Luo and R.I. Tanner. A streamline element scheme for solving viscoelastic flow problems. Part I. Differential constitutive equations. *Journal of Non-Newtonian Fluid Mechanics*, 21:179, 1986a.

X.L. Luo and R.I. Tanner. A streamline element scheme for solving viscoelastic flowproblems part II: Integral constitutive models. *Journal of Non-Newtonian Fluid Mechanics*, 22:61, 1986b.

J.J. Magda and R.G. Larson. A transition occurring in ideal elastic liquids during shear flow. *Journal of Non-Newtonian Fluid Mechanics*, 30:1, 1988.

C. Masselon, J.B. Salmon, and A. Colin. Nonlocal effects in flows of wormlike micellar solutions. *Physical Review Letters*, 100:38301, 2008.

G.H. McKinley and A. Tripathi. How to extract the Newtonian viscosity from capillary breakup measurements in a filament rheometer. *Journal of Rheology*, 44:653, 2000.

C.D. Meinhart and S.T. Wereley. The theory of diffraction-limited resolution in microparticle image velocimetry. *Measurement Science and Technology*, 14:1047, 2003.

C.D. Meinhart and H. Zhang. The flow structure inside a microfabricated inkjet printhead. *Journal of Microelectromechanical Systems*, 9:67, 2002.

C.D. Meinhart, S.T. Wereley, and J.G. Santiago. PIV measurements of a microchannel flow. *Experiments in Fluids*, 27:414, 1999.

C.D. Meinhart, S.T. Wereley, and M.H.B. Gray. Volume illumination for two-dimensional particle image velocimetry. *Measurement Science and Technology*, 11:809, 2000.

E. Miller and J. Cooper-White. The effects of chain conformation in the microfluidic entry flow of polymer-surfactant systems. *Journal of Non-Newtonian Fluid Mechanics*, 160:22, 2009.

S. Nigen and K. Walters. Viscoelastic contraction flows: comparison of axisymmetric and planar configurations. *Journal of non-newtonian fluid mechanics*, 102:343, 2002.

W. Ohnesorge. Formation of drops by nozzles and the breakup of liquid jets. *Zeitschrift fur Angewandte Mathematik und Mechanik*, 16:355, 1936.

M.S.N. Oliveira, M.A. Alves, F.T. Pinho, and G.H. McKinley. Viscous flow through microfabricated hyperbolic contractions. *Experiments in Fluids*, 43:437, 2007.

M.S.N. Oliveira, L.E. Rodd, G.H. McKinley, and M.A. Alves. Simulations of extensional flow in microrheometric devices. *Microfluidics and Nanofluidics*, 5:809, 2008.

M.G. Olsen and R.J. Adrian. Out-of-focus effects on particle image visibility and correlation in microscopic particle image velocimetry. *Experiments in Fluids*, 29: 166, 2000.

S.C. Omowunmi and X.F. Yuan. Modelling the three-dimensional flow of a semi-dilute polymer solution in microfluidics. On the effect of aspect ratio. *Rheologica acta*, 49:585, 2010.

J. Ouellette. A new wave of microfluidic devices. *Industrial Physicist*, 9:14, 2003.

L. Pellens, R.G. Corrales, and J. Mewis. General nonlinear rheological behavior of associative polymers. *Journal of rheology*, 48:379, 2004.

T.T. Perkins, S.R. Quake, D. E. Smith, and S. Chu. Relaxation of a single DNA molecule observed by optical microscopy. *Science*, 264:822, 1994.

A. Peterlin. Hydrodynamics of linear macromolecules. *Pure Appl. Chem*, 12:563, 1966.

C.J. Pipe and G.H. McKinley. Microfluidic rheometry. *Mechanics Research Communications*, 36:110, 2009.

C.J. Pipe, T.S. Majmudar, and G.H. McKinley. High shear rate viscometry. *Rheologica Acta*, 47:621, 2008.

L. Rayleigh. On the capillary phenomena of jets. *Proceedings of the Royal Society of London*, page 71, 1879.

L.E. Rodd, T.P. Scott, D.V. Boger, J.J. Cooper-White, and G.H. McKinley. The inertio-elastic planar entry flow of low-viscosity elastic fluids in micro-fabricated geometries. *Journal of Non-Newtonian Fluid Mechanics*, 129:1, 2005a.

L.E. Rodd, T.P. Scott, J.J. Cooper-White, and G.H. McKinley. Capillary break-up rheometry of low-viscosity elastic fluids. *Applied Rheology*, 15:12, 2005b.

L.E. Rodd, J.J. Cooper-White, D.V. Boger, and G.H. McKinley. Role of the elasticity number in the entry flow of dilute polymer solutions in micro-fabricated contraction geometries. *Journal of Non-Newtonian Fluid Mechanics*, 143:170, 2007.

L.E. Rodd, D. Lee, K.H. Ahn, and J.J. Cooper-White. The importance of downstream events in microfluidic viscoelastic entry flows: Consequences of increasing the constriction length. *Journal of Non-Newtonian Fluid Mechanics*, 165:1189, 2010.

J.P. Rothstein and G.H. McKinley. Extensional flow of a polystyrene boger fluid through a 4: 1: 4 axisymmetric contraction/expansion. *Journal of non-newtonian fluid mechanics*, 86:61, 1999.

J.G. Santiago, S.T. Wereley, C.D. Meinhart, D.J. Beebe, and R.J. Adrian. A particle image velocimetry system for microfluidics. *Experiments in Fluids*, 25:316, 1998.

L.A. Slobozhanin and J.M. Perales. Stability of liquid bridges between equal disks in an axial gravity field. *Physics of Fluids A: Fluid Dynamics*, 5:1305, 1993.

D.E. Smith, H.P. Babcock, and S. Chu. Single-polymer dynamics in steady shear flow. *Science*, 283:1724, 1999.

P.C. Sousa, P.M. Coelho, M.S.N. Oliveira, and M.A. Alves. Three-dimensional flow of Newtonian and Boger fluids in square–square contractions. *Journal of Non-Newtonian Fluid Mechanics*, 160:122, 2009.

T. Sridhar, V. Tirtaatmadja, D.A. Nguyen, and R.K. Gupta. Measurement of extensional viscosity of polymer solutions. *Journal of Non-Newtonian Fluid Mechanics*, 40:271, 1991.

G.I. Taylor. Stability of a viscous liquid contained between two rotating cylinders. *Philosophical Transactions of the Royal Society of London. Series A, Containing Papers of a Mathematical or Physical Character*, 223:289, 1923.

G.B. Thurston. Elastic effects in pulsatile blood flow. *Microvascular Research*, 9: 145, 1975.

G.B. Thurston and N.M. Henderson. Effects of flow geometry on blood viscoelasticity. *Biorheology*, 43:729, 2006.

V. Tirtaatmadja, GH McKinley, and JJ Cooper-White. Drop formation and breakup of low viscosity elastic fluids: Effects of molecular weight and concentration. *Physics of Fluids*, 18:043101, 2006.

D.C. Vadillo, T.R. Tuladhar, A.C. Mulji, and M.R. Mackley. The rheological characterization of linear viscoelasticity for ink jet fluids using piezo axial vibrator and torsion resonator rheometers. *Journal of Rheology*, 54:781, 2010.

S.T. Wereley and C.D. Meinhart. Micron-resolution particle image velocimetry. *Microscale Diagnostic Techniques*, page 51, 2005.

S.T. Wereley, L. Gui, and C.D. Meinhart. Advanced algorithms for microscale particle image velocimetry. *AIAA Journal*, 40:1047, 2002.

F.M. White. *Viscous fluid flow*. McGraw-Hill New York, 1991.

G.M. Whitesides. The origins and the future of microfluidics. *Nature*, 442:368, 2006.

S.C. Xue, N. Phan-Thien, and R.I. Tanner. Three dimensional numerical simulations of viscoelastic flows through planar contractions. *Journal of Non-Newtonian Fluid Mechanics*, 74:195, 1998.

A. Ziabicki and K. Kedzierska. Studies on the orientation phenomena by fiber formation from polymer melts. part i. preliminary investigations on polycapronamide. *Journal of Applied Polymer Science*, 2:14, 1959.

B.H. Zimm. Dynamics of polymer molecules in dilute solution: viscoelasticity, flow birefringence and dielectric loss. *The Journal of Chemical Physics*, 24:269, 1956.

Appendix

Publications

A. Lanzaro and X.F. Yuan. Effects of contraction ratio on non-linear dynamics of semi-dilute, highly polydisperse PAAm solutions in microfluidics. *Journal of Non-Newtonian Fluid Mechanics*, 2011.

Invited talks

"Quantitative characterization of complex fluids in highly non-linear flow regimes", British Society of Rheology Midwinter Meeting, 2008, Leeds, UK

"Towards a novel design of Microfluidic Rheometer", the 5^{th} Meeting of the European Society of Rheology, Cardiff, UK